

THE EFFECT OF FLUORIDE ON
THE CRYSTALLINITY AND
PHOTOACTIVITY OF TiO₂

by

JONATHAN ISAAC BRAUER

GREGORY J. SZULCZEWSKI, COMMITTEE CHAIR
SHANE C. STREET
DAVID A. DIXON
ARUNAVA GUPTA
TIM MEWES

A DISSERTATION

Submitted in partial fulfillment of the requirements
for the degree of Doctor of Philosophy
in the Department of Chemistry
in the Graduate School of
The University of Alabama

TUSCALOOSA, ALABAMA

2012

Copyright Jonathan Brauer 2012

ALL RIGHTS RESERVED

ABSTRACT

This dissertation describes the synthesis and characterization of fluorinated N-doped TiO₂ nanoparticles under ambient conditions. Samples were synthesized by sol-gel methods that utilized the controlled hydrolysis of titanium(IV) tetra-isopropoxide in acidic solutions. Nitrogen doping was achieved by two different methods. In one scheme triethylamine (TEA) was added post-synthesis to the nanoparticle formation. In the other scheme, ammonium chloride (NH₄Cl) was added during the acid catalyzed hydrolysis reaction. A freeze-drying process of the sol-gel was used to prevent aggregation during dehydration and was found to retain the high surface area of the powder. Post-synthesis the hydroxyl groups on the surface were exchanged with fluoride by stirring the powders in acidic solution of NaF. Using this synthetic approach the amount of nitrogen and fluoride could be independently controlled. The nanoparticles were characterized by numerous spectroscopic techniques including DRS, FTIR, Raman, and XPS. Vibrational spectroscopy shows that the particles contain significant amounts of organic impurities after doping with TEA. In contrast, particles synthesized with NH₄Cl showed much less contamination. XPS analysis revealed that a single nitrogen species with a binding energy of 400.6 eV when using TEA as the N precursor. In contrast, when NH₄Cl was used as the nitrogen precursor two nitrogen species were observed with binding energies at 402.6 and 401.2 eV. These latter peaks are assigned to interstitial nitrogen in the N¹⁺ and N⁰ oxidation states. The as-synthesized nanoparticles also show a significant differences in their optical properties. In general, the particles doped from TEA and NH₄Cl were yellow and white, respectively, despite

containing approximately the same amount of nitrogen (~5% with respect to Ti). The difference is attributed to a high fraction of oxygen-vacancies in the TEA doped nanoparticles.

XRD and Raman measurements determined that the as-synthesized samples were amorphous, but could be converted to the anatase phase by two different methods. Thermal annealing was shown to convert the amorphous particles to the anatase polymorph. The presence of surface fluoride was found to significantly lower the temperature to observe the amorphous to anatase transition. In the second method, stirring the powders in acidic solutions of NaF at room temperature for 12-168 hours produced the anatase phase with an average crystallite size of 4 nm. It was found that the phase transition only occurs when the pH is below the point of zero charge of the particles.

The photoactivity of the nitrogen and nitrogen / fluoride-doped particles was tested for their ability to degrade methylene blue (MB) with visible light (> 400 nm). In general the particles with a surface fluoride were more photoactive than those without. In addition, particles with nitrogen were more photoactive than pure TiO₂. By analyzing the decomposition products with electrospray ionization mass spectrometry and UV-Vis spectroscopy, it was possible to elucidate a different decomposition pathway for the nitrogen-doped samples. When TEA was the dopant precursor, MB primarily decomposed by a ring-cleavage pathway using superoxide. In contrast, when NH₄Cl was the dopant precursor, MB decomposed through demethylation pathway induced by hydroxyl radicals. The as-synthesized particles were found to be more photoactive than those thermally annealed. The loss of photoactivity could be ascribed to two main factors: (1) loss of nitrogen and fluoride and (2) loss of surface area by sintering.

DEDICATION

To Leon

Whose love for life
was envied by all who knew him.

LIST OF ABBREVIATIONS AND SYMBOLS

°C	degrees centigrade
Å	Angstrom (0.1 nm)
A-R	anatase to rutile
a.u.	arbitrary units
AM1.5	Air Mass 1.5 (a solar irradiation standard)
ATR	Attenuated Total Reflectance (an FTIR technique for solids)
AU	Absorbance Units
BET	Brunauer-Emmett-Teller surface area analysis
CB	Conduction band
cip	common intersection point
cm	centimeter
CPS	counts per second
DOS	Density of States
DRIFTS	Diffuse Reflectance Infrared Fourier Transform Spectroscopy

DRS	Diffuse Reflectance Spectroscopy (a UV-Vis technique for solids)
ESI-MS	ElectroSpray Ionization – Mass Spectrometry
eV	electron volt
FTIR	Fourier Transform Infrared Spectroscopy
FWHM	Full Width at Half Maximum
GL(x)	x percent Gaussian, 100-x percent Lorentzian (peak shape)
GPa	GigaPascals
IPA	Isopropyl alcohol, 2-propanol, isopropanol
ISE	Ion Selective Electrode
lN_2	Liquid Nitrogen
LMB	leucomethylene blue
M	Molarity (mol/L)
MB	Methylene Blue
mg	milligram
mL	milliliter
MΩ	megaohm
nm	nanometers

V _o	Oxygen vacancy
P-25	Degussa P-25 Aeroxide, a standard TiO ₂ powder
PID	Proportional Integral Derivative (an algorithm)
PTT	Phase Transition Temperature
PZC	Point of Zero Charge
ROS	Reactive Oxygen Species
RPM	revolutions per minute
sccm	Standard Cubic Centimeters per Minute
SEM	Scanning Electron Microscopy
SF	Sensitivity Factor (for XPS)
STP	standard temperature and pressure (0 °C, 100 kPa)
Ti(OiPr) ₄	Titanium(IV) tetra-isopropoxide
TiO ₂	Titanium Dioxide, Titania
TTIP	Titanium(IV) tetra-isopropoxide
UHV	Ultra High Vacuum
UV-Vis	Ultra Violet – Visible Spectroscopy
VB	Valence Band

W	watt
XPS	X-ray Photoelectron Spectroscopy
XRD	X-ray diffraction
α -A	amorphous to anatase

ACKNOWLEDGMENTS

I would like to take this opportunity to thank my research advisor, Dr. Greg Szulczewski, for providing support and guidance throughout my graduate studies, without which this dissertation would not have been possible. I would also like to thank my committee members, Drs. David Dixon, Arunava Gupta, Tim Mewes, and Shane Street for their valuable advice and suggestions. Thanks also are also due Dr. James Gole from Georgia Tech for providing the initial procedure and taking the time to show me his lab and process.

Many UA faculty lent expertise and instrumentation. Thanks go to Drs. Micheal Bowman (EPR and irradiation instrumentation), Alan Lane (BET advice and instrumentation), Patrick Leclair (providing XAS opportunities), Shanlin Pan (annealing ovens and microscopes), Shane Street (DRIFTS and FTIR), Joe Thrasher (F⁻ ISE), and Tom Vaid (XRD and DRS instrumentation).

I would like to thank the University of Alabama Chemistry Department and NSF NIRT grant #CTS-0608896 (PI: Dr. Dixon) for supporting me financially during for this work.

Lastly, I would like to thank my past and current group members, who have established a great camaraderie among the Szulczewski group: Weihao Xu, Jian Tang, Justin Kreil, Ed Ellingsworth, and Kim Anderson, all of whom have countless contributions to this dissertation.

CONTENTS

ABSTRACT.....	ii
DEDICATION.....	iv
LIST OF ABBREVIATIONS AND SYMBOLS.....	v
ACKNOWLEDGMENTS.....	ix
LIST OF TABLES.....	xiv
LIST OF FIGURES.....	xv
CHAPTER 1 - INTRODUCTION.....	1
1.1 Origin of Photoactivity.....	2
1.1.1 Photon Absorption.....	4
1.1.2 Electron-Hole Pair Migration.....	8
1.1.3 Surface Interaction.....	8
1.2 TiO ₂ Polymorphs.....	9
1.3 Synthesis Methods.....	13
1.3.1 Pure TiO ₂	13
1.3.2 Doping TiO ₂	13
1.3.3 Effect of Fluoride.....	16
1.4 Prior Photoactivity Experiments.....	18

1.4.1 Methylene Blue.....	19
1.5 Outline of this Dissertation.....	22
CHAPTER 2 - EXPERIMENTAL METHODS.....	24
2.1 X-Ray Photoelectron Spectroscopy.....	24
2.2 X-Ray Diffraction.....	25
2.3 UV-Vis Diffuse Reflectance Spectroscopy.....	27
2.4 Raman Spectroscopy.....	27
2.5 Fluoride Ion Selective Electrode.....	27
2.6 Surface Area Measurement.....	27
2.6.1 Single Point BET.....	29
2.6.2 Molecular adsorption.....	31
2.7 Fourier Transform Infrared Spectroscopy (FTIR).....	31
2.8 Photoactivity.....	32
2.9 Point of Zero Charge.....	37
2.10 Auger Electron Spectroscopy.....	41
2.11 Electrospray Ionization Mass Spectrometry.....	41
2.12 Thermogravimetric Analysis.....	42
CHAPTER 3 - TiO ₂ SYNTHESIS.....	43
3.1 Chemicals.....	43
3.2 Organic Precursors (TEA).....	43
3.2.1 Synthesis.....	43
3.2.2 Surface Area.....	46

3.2.3 Purity.....	46
3.2.4 Doping.....	48
3.3 Inorganic Precursors (NH ₄ Cl).....	51
3.3.1 Synthesis.....	51
3.3.2 Doping.....	52
3.4 Hydrophilicity.....	61
3.5 Annealing.....	61
3.6 Standards.....	63
3.7 Conclusions.....	63
CHAPTER 4 - CRYSTALLINITY.....	65
4.1 Annealing.....	65
4.2 Effect of Fluorination.....	65
4.2.1 Proposed Mechanism of Anatase Formation.....	71
4.2.2 Crystallization Kinetics.....	73
4.2.3 pH dependance.....	75
4.3 Phase Transition Temperature.....	80
CHAPTER 5 - PHOTOACTIVITY.....	86
5.1 Increasing the Optical Absorption.....	86
5.1.1 Powders from Organic Synthesis.....	86
5.1.2 Powders from Inorganic Synthesis.....	88
5.1.3 Effect of Doping on O Vacancy Creation.....	88
5.2 Photodegradation of MB.....	93

5.2.1 Effect of N-doping and Surface Fluorination.....	93
5.2.2 Effect of Fluorination.....	98
5.2.3 Effect of Annealing and Surface Area.....	102
5.2.4 Effect of Crystallinity.....	107
5.3 Conclusions.....	107
CHAPTER 6 - CONCLUSIONS.....	110
6.1 This Work.....	110
6.1.1 Synthesis.....	110
6.1.2 Crystallinity	110
6.1.3 Photoactivity.....	111
6.2 Future Work.....	112
6.2.1 F ⁻ adsorption	112
6.2.2 Anatase formation	112
6.2.3 Phase Transition Temperature.....	112
6.2.4 BET Studies.....	113
6.2.5 Other Analyte Molecules.....	113
CHAPTER 7 - ADDITIONAL EXPERIMENTS.....	114
7.1 Effect of N on Surface Group Retention.....	114
7.2 Metal-doped TiO ₂	117
7.3 Effect of pH and Buffers on Photoactivity	117
REFERENCES.....	121

LIST OF TABLES

Table 3.1: Peak positions of the N(1s) signal in Figure 3.6 and relative amounts of N/Ti.....	58
Table 4.1: Surface energies for anatase and rutile from [139].....	72
Table 4.2: Comparison of the available HF and the amount of anatase formed at a given pH.....	81
Table 5.1: Comparison of the relative amounts of demethylation products as a function of amount of absorbed fluoride.....	101
Table 5.2: Summary of surface areas, N and F amounts, and MB decomposition rate constants versus annealing temperature for N-doped TiO ₂ from the NH ₄ Cl synthesis.	104

LIST OF FIGURES

- Figure 1.1: Cartoon of photoactivity mechanism for TiO_2 . (a) an incident photon is absorbed, (b) promoting an electron from the valence band (VB) to the conduction band (CB). (c) The electron (e^-) and hole (h^+) migrate to the surface of the particle, and (d) react with surface adsorbed species.....3
- Figure 1.2: Cartoon illustrating the effect of doping on the bandgap of Cr- and N-doped TiO_2 . (a) undoped TiO_2 requires UV light for exciton creation, while (b) can utilize visible light due to the added states from the dopant atoms.....5
- Figure 1.3: Spectrum of solar radiation at the earth's surface with the sun at 48.2° from zenith, or at AM1.5, adapted from [18].....6
- Figure 1.4: Comparison of the VB and CB positions for various metal oxides, in order of increasing bandgap.....10
- Figure 1.5: Unit cells for the anatase, rutile and brookite polymorphs of TiO_2 [34,35]. The bandgaps and standard enthalpy of formation[36] are shown as well.....11
- Figure 1.6: Photograph of a naturally occurring anatase crystal mined in the Czech Republic.. 17
- Figure 1.7: Scheme showing the decomposition of MB by the demethylation pathway. The names, maximum absorbance, and molecular weight of the intermediates are noted.....20
- Figure 1.8: Scheme showing the decomposition of MB by the ring cleavage pathway.....21
- Figure 2.1: Method to estimate the bandgap from UV-Vis data. This shows the DRS for undoped TiO_2 , and the bandgap is 400 nm, or 3.1 eV.....28
- Figure 2.2: Representative BET data. Peaks due to (a) gas contraction (b) N_2 absorption (c) gas expansion (d) N_2 desorption (e) 0.5 mL reference aliquot (f) 1.0 mL reference aliquot.....30
- Figure 2.3: Diagram of the filter setup. (a) shows the absorption of pure (undoped) TiO_2 , (b) methylene blue and (c) shows the percent transmittance of the filter combination.....34
- Figure 2.4: Calibration curve for MB. The line is an exponential fit to the data, with the equation shown. The inset shows the deviation at low concentrations.....36
- Figure 2.5: Method for extracting rate constants from raw UV-Vis data. (a) shows the raw

UV-Vis data, as the MB is irradiated the concentration falls. (b) shows the conversion to concentration. (c) shows the fit to an exponential decay.....	38
Figure 2.6: Method to find the PZC of a material. The effect of the salt concentration on the pH is measured. The intersection point indicated shows where the salt has no effect on the pH.....	40
Figure 3.1: Setup for TiO ₂ synthesis. See text for details.....	45
Figure 3.2: FTIR spectra of TEA sample. (a) shows the N-doped TiO ₂ before and (b) after annealing to 300 °C for 6 hours. (c) shows N,F-doped TiO ₂ before and (d) after annealing.....	47
Figure 3.3: XPS survey scan of samples made with organic precursors. (a) N-doped, (b) N,F-doped. Peak assignments from [71].....	49
Figure 3.4: High resolution XPS of N(1s) and F(1s) for the TEA sample. (a) shows the N-doped TiO ₂ , (b) N,F-doped TiO ₂ , (c) N-doped TiO ₂ after annealing at 300 °C, (d) F,N-doped TiO ₂ after annealing at 300 °C.....	50
Figure 3.5: TGA analysis of N-doped TiO ₂ from (a) TEA and (b) NH ₄ Cl samples. (c) and (d) show the absolute value of the derivative of (a) and (b), respectively. Note the 30-minute isotherm from time=10 min.....	54
Figure 3.6: High resolution XPS of the N(1s) region of N-doped NH ₄ Cl samples (a) shows the as made samples, (b) annealed to 300 °C, (c) treated with 10 mM NaF, and (d) treated with 100 mM NaF.....	55
Figure 3.7: Comparison of N(1s) binding energies from published literature. Compiled from [25,26,97–124].....	56
Figure 3.8: High resolution XPS of the F(1s) region of N-doped NH ₄ Cl samples. (a) shows the as made samples, (b) treated with 10 mM NaF, and (c) treated with 100 mM NaF.....	59
Figure 3.9: DRIFTS measurements of N-doped NH ₄ Cl sample. (a) shows the as made samples, (b) treated with 100 mM NaF.....	60
Figure 3.10: Effect of annealing on the retention of dopants for NH ₄ Cl samples.....	62
Figure 4.1: XRD spectra show (a) as made TiO ₂ samples and (b) annealed to 300 °C. The standard peak positions and intensities for anatase and rutile are shown.....	66
Figure 4.2: XRD spectra of N-doped TiO ₂ showing the growth of anatase. (a) shows N-doped TiO ₂ as synthesized, (b) after annealing to 300 °C for 6 hours, (c) after fluorinating in 10 mM NaF, (d) after fluorinating in 100 mM NaF. (e) shows the calculated spectra of pure anatase assuming a crystallite size of 4 nm. The standard anatase powder positions and intensities are noted[37].....	67

Figure 4.3: Raman spectra of surface F-doped TiO₂. (a) shows as synthesized TiO₂, (b) fluorinated in 10 mM NaF solution, (c) fluorination in 100 mM NaF solution, (d) standard anatase, and (e) standard rutile. The raman modes for anatase are noted[131].....69

Figure 4.4: DRS of NH₄Cl samples. (a) N-doped TiO₂, (b) fluorinated anatase N-doped TiO₂, (c) fluorinated amorphous N-doped TiO₂. (d) shows the AM1.5 solar spectrum.....70

Figure 4.5: Time dependance of the growth of anatase in a 10 mM NaF at pH=3.4. (a) shows the anatase (101) peak after various reaction times. (b) Peak intensities with respect to time....74

Figure 4.6: XRD spectra to show the influence of N-doping. (a) shows growth over time of anatase (101) peak for undoped TiO₂, (b) shows N-doped TiO₂.....76

Figure 4.7: XRD spectra of the anatase (101) peak to show the anatase transformation at various pH values for pure TiO₂. The dark line is the fit, with the data shown in gray.....77

Figure 4.8: Theoretical concentration of HF vs pH based on a pK_a for HF of 3.167 is shown with ●. On the right axis, the anatase (101) peak intensity from Figure 4.7 is shown with ■.....78

Figure 4.9: Measurement to find the PZC of N-doped NH₄Cl sample.....79

Figure 4.10: The data points are linked to the left axis and show the amount of F⁻ remaining in solution after fluorination vs pH of the fluorination solution. The solid line on the right axis shows the amount of F⁻ vs HF.....82

Figure 4.11: AES after treating NH₄Cl samples at various pH values.....83

Figure 4.12: XRD spectra to show the effect of F on the PTT. (a) shows as synthesized N-doped TiO₂, (b) after annealing (a) to 300 °C for 6 hours, (c) after fluorinating (a) in 10 mM NaF, (d) after annealing (c) to 300 °C for 6 hours, (e) after fluorinating (b) in 100 mM NaF...85

Figure 5.1: DRS of TEA samples. (a) P-25, (b) pure TiO₂, (c) N-doped TiO₂, and (d) F,N-doped TiO₂. (e) shows the AM1.5 solar spectrum. The inset shows a photograph of the samples.....87

Figure 5.2: DRS of NH₄Cl samples. (a) pure TiO₂, (b) N-doped TiO₂, (c) F,N-doped TiO₂. (d) shows the AM1.5 solar spectrum. The inset shows a photograph of the samples.....89

Figure 5.3: DRS of (a) N-doped and (b) pure (undoped) NH₄Cl samples. The bandgap shift is shown by arrow 1, and the creation of O vacancies is shown by arrow 2.....91

Figure 5.4: DRS at various annealing temperatures for (a) N-doped TiO₂, (b) N-doped TiO₂ with a small amount of surface F, and (c) N-doped TiO₂ with the surface saturated in F for NH₄Cl samples.....92

Figure 5.5: Normalized UV-Vis spectra for MB photodecomposition. (a) shows pure, (b) N-doped, and (c) F,N-doped TEA samples.....	94
Figure 5.6: Rates for photodecomposition of MB for (a) pure MB, no TiO ₂ (b) pure (undoped), (c) N-doped, and (d) N,F-doped TEA samples. The table shows the extracted pseudo first order rate constants.....	95
Figure 5.7: ESI-MS of the decomposition products for N-doped TEA samples. (a) shows the sample before irradiation, (b) after 210 minutes of irradiation time, and (c) after 390 minutes.	97
Figure 5.8: UV-Vis spectra for MB degradation. (a) shows Degussa P-25, (b) shows as synthesized N-doped, and (c) shows fluorinated N-doped NH ₄ Cl samples.....	99
Figure 5.9: ESI-MS showing the effect of fluorination on the degradation path for NH ₄ Cl samples. (a) shows the as-synthesized N-doped, (b) was fluorinated at pH=7, and (c) was fluorinated at pH=3.....	100
Figure 5.10: Effect of annealing on the photodegradation rate of MB. (a) shows N-doped, (b) anatase N,F-doped, and (c) amorphous N,F-doped NH ₄ Cl samples.....	103
Figure 5.11: Effect of surface area on the rate constant. ● shows N-doped, ■ shows anatase F,N-doped, and ♦ shows amorphous F,N-doped NH ₄ Cl samples.....	105
Figure 5.12: Comparison of the rate as a function of the surface area. (a) shows N-doped, (b) anatase N,F-doped, and (c) amorphous N,F-doped NH ₄ Cl samples.....	106
Figure 5.13: Photodecomposition rates of MB for N-doped NH ₄ Cl samples annealed at 300 °C for 6 hours. (a) annealed, (b) annealed then fluorinated with a 10 mM NaF solution, (c) fluorinated then annealed.....	108
Figure 7.1: FTIR of N-doped NH ₄ Cl samples shown as a solid line, and undoped NH ₄ Cl samples shown as a dashed line. Lines (a) and (b) are untreated, (c) and (d) are treated with 10 mM NaF, and (e) and (f) are treated with 100 mM NaF.....	115
Figure 7.2: XRD of undoped (a, c, and d), and N-doped (b, d, and f) NH ₄ Cl samples, as made (a,b), after treatment with 10 mM NaF (c,d), and 100 mM NaF (e,f).....	116
Figure 7.3: pH dependance for MB degradation. (a) at pH = 4, (b) pH = 7, and (c) pH = 10..	118
Figure 7.4: The effect of buffer solutions on the autodegradation of MB.....	120

CHAPTER 1 - INTRODUCTION

Titanium Dioxide (TiO_2), also commonly called titania, is a common mineral with a very wide range of applications. Currently, it is chiefly used as a pigment and a pigment base, due to its high refractive index ($n=2.7^1$) and bright white color. Combined with the fact that TiO_2 is abundant, inexpensive (0.7% of the earth's crust²) and chemically inert (safe for handling and consumption) leads to over 70% of all pigments in paints, foodstuffs, inks, cosmetics, sunscreens and others containing TiO_2^3 .

TiO_2 owes its bright white color to its bandgap (the energy difference between the valence and conduction bands) being greater than visible light, causing all wavelengths of visible light to be reflected. While the bandgap for TiO_2 is too large to absorb visible light, it is small enough to absorb ultraviolet (UV) light. In 1972, Fujishima and Honda⁴ showed that the energy from the absorbed UV photon can then be harnessed to drive chemical reactions, a process globally known as photoactivity⁵. This has found commercial applications in recent years. Hydrophillic (anti-fog) coatings for glass⁶ cause water to form in sheets rather than droplets on glass, allowing it to remain transparent. Hospitals and water treatment plants use TiO_2 based systems for the elimination of air- and waterborne pathogens^{7,8}, where a small reaction with a cell wall is enough to kill a cell. A feature article in *Chemical & Engineering News* showcased self-cleaning glass and concrete^{9,10}, which uses TiO_2 and sunlight to mineralize any pollutants that come in contact with it. Additionally, hundreds of applications have emerged in research labs, including water splitting for the green production of H_2 as an energy source¹¹, CO_2 reduction to

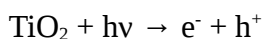
methane, methanol and other useful compounds¹², and hydroxylation, coupling, cycloaddition and other steps of organic synthesis routes^{13,14}. Often the photon source for these reactions is sunlight. Consequently, research on improving the photoactivity of TiO₂ has been growing exponentially¹⁵.

This dissertation focuses on ongoing improvements to the visible light photoactivity of TiO₂. This introductory chapter will summarize the properties of TiO₂ and mechanisms by which the chemistry takes place.

1.1 Origin of Photoactivity

Currently, all the commercial uses of photoactive TiO₂ involve the degradation of pollutants. The photoactivity is most often measured and used for the mineralization (decomposition to lowest-energy species, i.e. H₂O, CO₂, etc) of pollutant molecules. Analogous is the use of TiO₂ as a bactericidal agent, where complete mineralization is not necessary, only small disruptions to the cell walls of water- or air-borne pathogens are enough. However, TiO₂ can also be used to drive synthesis reactions. Reactions that require the addition of an O as an alcohol or carbonyl are especially well suited. The mechanism that drives the photoactivity is the same regardless of the end result.

There are four basic steps to photoactivity, shown in the cartoon in Figure 1.1: a photon is absorbed (shown in Figure 1.1.a), promoting an electron from the valence band (labeled VB) to the conduction band (CB) and creating an electron/hole pair (e⁻/h⁺ pair) (Figure 1.1.b). This is often written as a chemical reaction



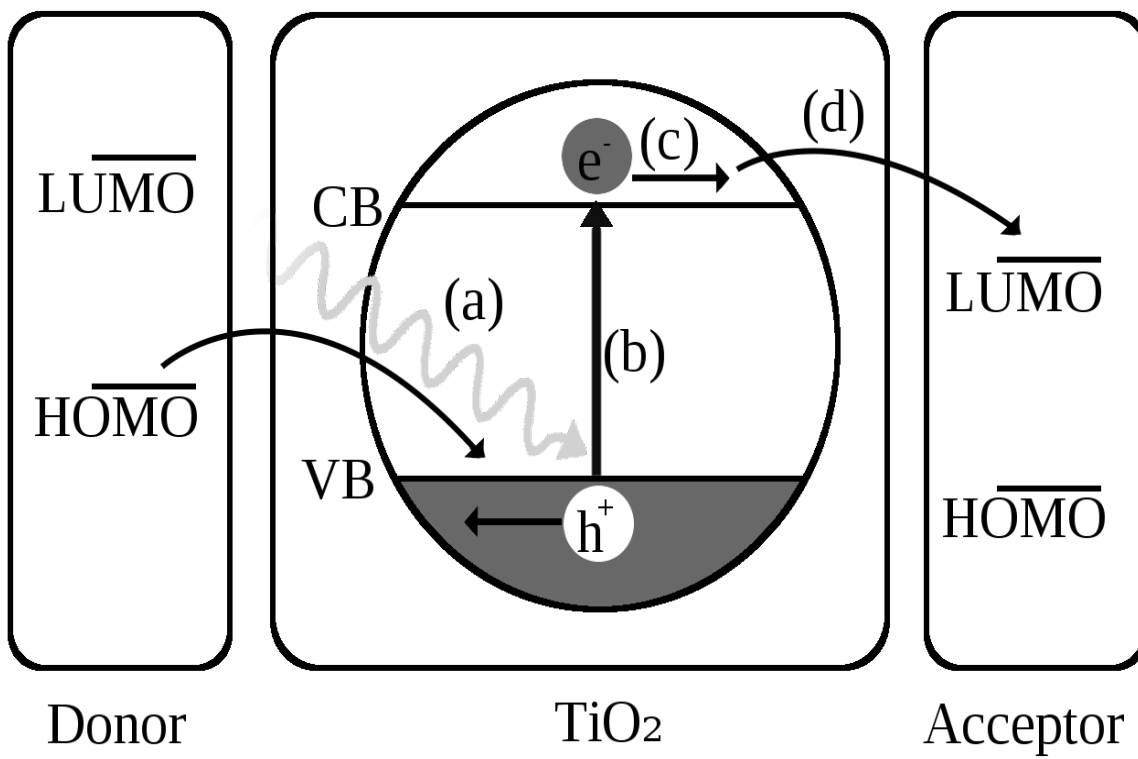
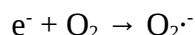
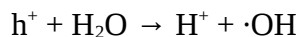


Figure 1.1: Cartoon of photoactivity mechanism for TiO₂. (a) an incident photon is absorbed, (b) promoting an electron from the valence band (VB) to the conduction band (CB). (c) The electron (e^-) and hole (h^+) migrate to the surface of the particle, and (d) react with surface adsorbed species.

The e^- and h^+ are mobile in physical space, and can migrate to the surface of the particle (Figure 1.1.c). There, they react with molecules absorbed to the surface of the particle (Figure 1.1.d).

The e^- and h^+ can directly react with a target molecule as shown in Figure 1.1, or, in a process known as remote photoactivity¹⁶, the e^- and h^+ react with water and O_2 on the surface which forms reactive species



superoxide, and hydroxyl radicals, which can go on to form other species such as hydrogen peroxide¹⁷, which migrate away from the TiO_2 particle to react with the target molecule. These species are termed reactive oxygen species (ROS).

To optimize photoactivity, several aspects of this mechanism must be optimized:

1.1.1 Photon Absorption

First, the photon absorbed in Figure 1.1.a must be of an energy greater than the bandgap (E_{gap}), or the energy difference between the valence and conduction bands, in order to promote an electron. For pristine TiO_2 , the VB maximum and CB minimum correspond to the O 2p and Ti 3d states, respectively, as shown in Figure 1.2. For TiO_2 , this means an energy greater than 3.0-3.2 eV, or a wavelength less than 413-387 nm, depending on the polymorph. This equates to about 2.2% of sunlight that reaches the earth's surface¹⁸ as shown in Figure 1.3. In 2001, Asahi et al.¹⁹ showed that doping the TiO_2 with other elements could reduce the bandgap, allowing less energetic photons, i.e. visible light, to be absorbed and utilized. Cationic dopants are usually metal ions that replace the Ti in the TiO_2 lattice and decrease the bandgap by lowering the CB, as shown in Figure 1.2 with Cr. However, this lowers the CB below the reduction potential for H_2O ,

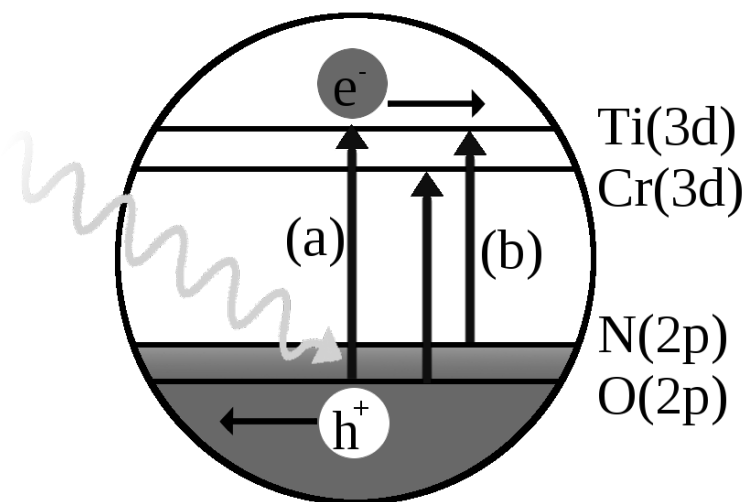


Figure 1.2: Cartoon illustrating the effect of doping on the bandgap of Cr- and N-doped TiO₂. (a) undoped TiO₂ requires UV light for exciton creation, while (b) can utilize visible light due to the added states from the dopant atoms.

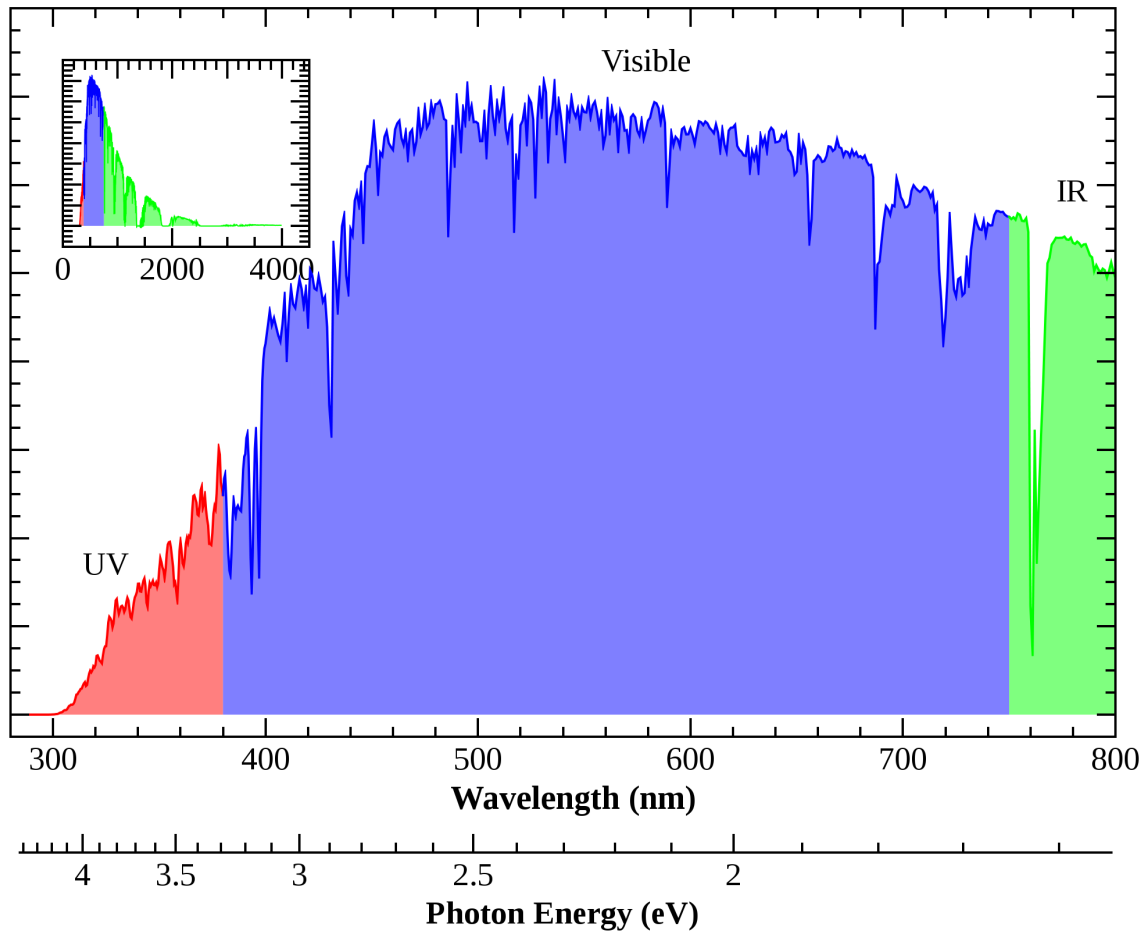


Figure 1.3: Spectrum of solar radiation at the earth's surface with the sun at 48.2° from zenith, or at AM1.5, adapted from [18].

hindering the creation of ROS. Additionally metal ions often act as recombination centers for the e^- / h^+ pair. Anionic dopants can lower the bandgap by adding density of states (DOS) near the VB, as shown in Figure 1.2 with N. For these reasons, Asahi et al. did not consider cationic dopants, and came to the conclusion that N doping would be the most effective. It was originally proposed that doping TiO_2 narrows the bandgap by mixing the N 2p states with the O 2p states to create a hybrid state. However, more recent studies have shown that the N introduces a localized N 2p state, and the visible light irradiation causes a transition from this localized state to the Ti 3d state²⁰.

Since then, it has been well established that doping TiO_2 with various elements can lower the bandgap and promote visible light photoactivity. Nitrogen has become the most commonly studied dopant. However, Cu, Co, Ni, Cr, Mn, Mo, Nb, V, Fe, Ru, Au, Ag, Pt, S, C, B, P, I, and F have all been studied²¹. It is worthwhile to note that while most dopants are studied for their ability to modify the bandgap, many dopants influence the chemistry in other ways, often detrimentally.

Equally important as the element used in the doping is how the dopant is incorporated into the host matrix. Asahi et al. proposed the direct replacement of an O atom with a N atom (known as substitutional N, or β -N) was responsible for the bandgap lowering¹⁹, and that the titanium nitride XPS peak at about 397 eV was indicative of the photoactivity. Newer papers show the exact opposite, with peaks attributed to interstitial NO correlating with photoactivity²². Indeed, Yates et al. have shown that the substitutional N does not lower the bandgap at all^{23,24}. Other papers have shown enhanced photoactivity without a Ti-N peak present at all^{25,26}.

1.1.2 Electron-Hole Pair Migration

Secondly, the e^- and h^+ need to migrate separately and reach the surface of the particle. If the e^- / h^+ pair find one another instead of the surface, they will recombine, releasing heat and wasting the energy. This migration is facilitated by a defect-free crystal structure, since defects and grain boundaries act as recombination sites. Small particle size also facilitates this process by reducing the physical distance the e^- and h^+ need to migrate. A well-defined crystal structure is achieved through high temperature annealing, with temperatures between 500 – 1,000 °C. However, this causes the particles to sinter and grow by Ostwald ripening, forfeiting the advantages of small particle size. Additionally, annealing in air drives out anionic dopants, which often have more stable states as oxides or diatomics. For N, many groups report the loss of N around 350 °C (confirmed by work reported in this dissertation), a temperature below the temperature for crystal formation from an amorphous TiO_2 powder of 400 °C²⁷. To get around this, many groups turn to hydrothermal synthesis methods, which involves a sealed reaction container heated in an autoclave for an extended time. This can produce particles that are very crystalline, but usually have a relatively low surface area.

1.1.3 Surface Interaction

Thirdly, for maximum efficiency, the TiO_2 particles need to be in a medium that allows the target molecules to interact with the surface freely. In aqueous solutions, the intrinsic surface charge of TiO_2 (ζ potential) must be considered. The TiO_2 surface is O-terminated, and the O atoms can be freely protonated and deprotonated depending on the pH of the solution. This means that depending on the surface charge and the pH of the solution, charged molecules are electrostatically repelled or attracted. To passivate the surface, groups have treated the surface

with F, which replaces the surface exposed -OH group. F also has the effect of selectively bonding to high-energy facets of TiO₂, so incorporating HF into the hydrothermal synthesis allows the growth of particles with specific facets unnaturally abundant²⁸.

Other metal oxides are also known to be photoactive, but due to the position of the valence and conduction bands are not generally used, as is shown in Figure 1.4. In order to generate reactive intermediates for an aqueous solution, the CB minimum needs to be above the reduction potential for water (-4.4 eV vs. Vacuum Level). Additionally, the metal oxide needs to be stable, non-toxic, and inexpensive. FeO, for example, cannot be used because it would decompose to Fe₂O₃ in an aqueous solution. TiO₂ has the best combination of characteristics and is known to be the most photoactive, and as such has been the focus of an exponentially growing amount of research. A number of review papers are available on the subject^{15,29-33}.

This same mechanism is widely referred to as photocatalysis. The term “photocatalysis” has been disputed, since the photon absorbed is consumed and should be considered a reactant. A true catalyst would not require the additional energy input from the photon. Even though the misnomer is widely used, the term “photoactivity” will be used instead in this dissertation.

1.2 TiO₂ Polymorphs

TiO₂ is found in nature as 5 polymorphs, and 6 more have been created in the lab. The three most common are anatase, rutile and brookite, whose crystal structures are shown in Figure 1.5 (adapted from [34,35]). Rutile is the most stable, with the vast majority of the TiO₂ on earth found in this form. Anatase and brookite are referred to as metastable at room temperature.

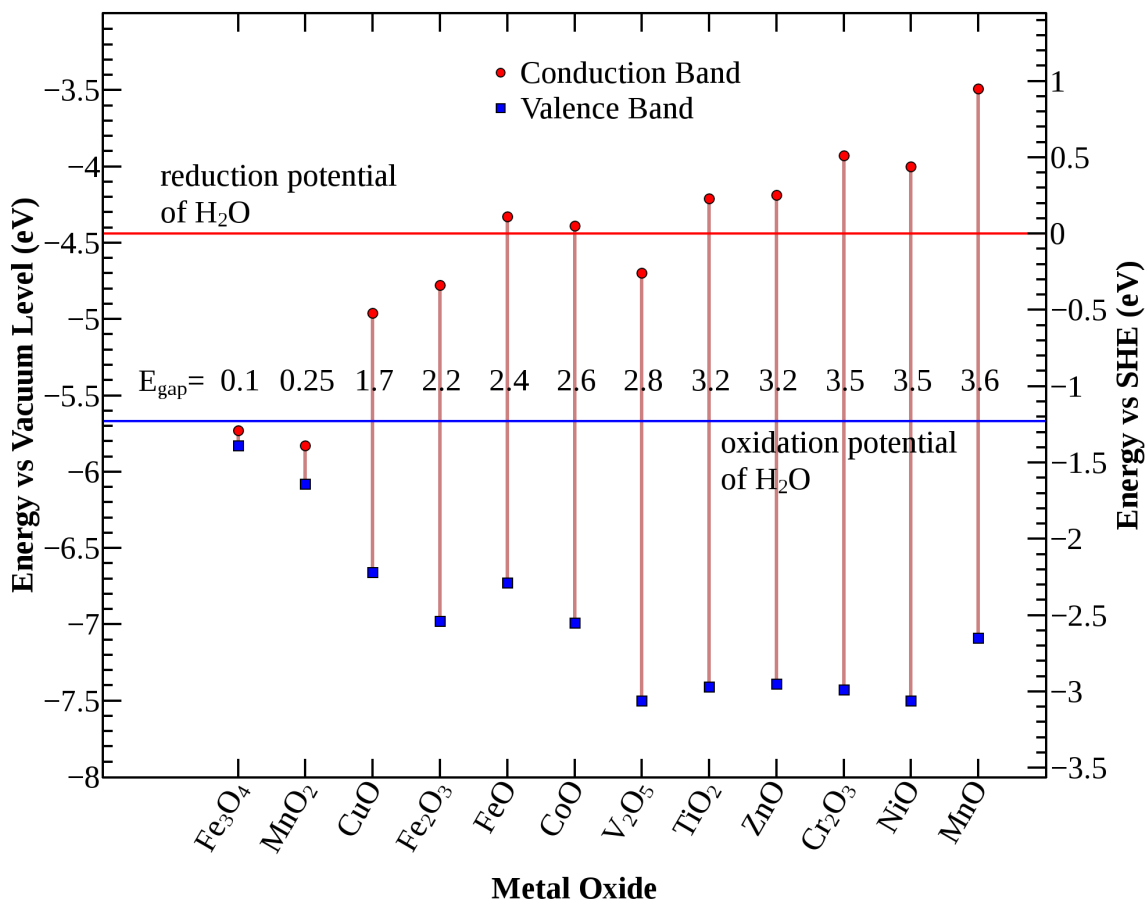


Figure 1.4: Comparison of the VB and CB positions for various metal oxides, in order of increasing bandgap.

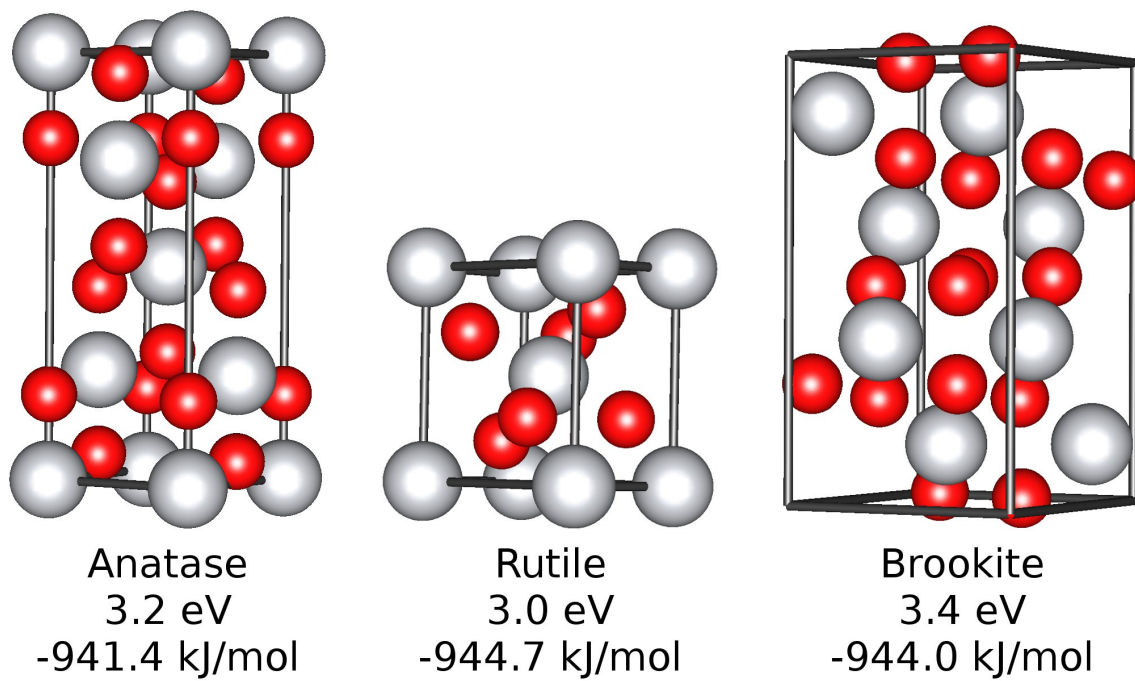


Figure 1.5: Unit cells for the anatase, rutile and brookite polymorphs of TiO_2 ^{34,35}. The bandgaps and standard enthalpy of formation³⁶ are shown as well.

The TiO₂ polymorph formed is important to the photoactivity. Pure (undoped), amorphous TiO₂ needs to be annealed to 400 °C to convert to anatase (known as the amorphous to anatase phase transition temperature, or α -A PTT), and then to 650-900 °C for conversion to rutile (A-R PTT)^{27,36,37}. The annealing process also sinters the particles, creating a larger mean particle size and reducing the surface area per mass. Rutile has a lower bandgap (3.0 eV vs 3.2 eV), but due to the high temperatures required, is difficult to produce with comparably small particle sizes to anatase. The result is that most groups report anatase to be more photoactive³⁸. However, most theoretical and fundamental studies are done on rutile single crystals, which are easy to work with and clean in UHV. Anatase continues to be reported to be the most photoactive, but more recent research shows that when particle size and surface area are normalized, anatase and rutile have very similar photoactivity³⁹. This may have biased literature that reports anatase is more photoactive than rutile, and it highlights the need for small, high surface area particles.

Research groups that study the properties of TiO₂ usually anneal samples to convert as synthesized amorphous TiO₂ to anatase, and then anneal them to a higher temperature if rutile is desired. The phase transition temperature for 100% conversion from amorphous TiO₂ (from sol-gel) to anatase is about 400°C, and from anatase to rutile (A-R PTT) is 650-750°C²⁷. However, annealing causes the particles to sinter and lose surface area.

Additionally, with increasing temperature and annealing time dopants added during the TiO₂ synthesis are driven out. This is especially true for cationic dopants. Other research has shown that dopants can have an increasing or decreasing effect on the α -A or A-R PTT⁴⁰.

1.3 Synthesis Methods

1.3.1 Pure TiO₂

TiO₂ is an extremely common mineral, making 0.7% of the earth's crust in the form of rutile sand². TiO₂ is chiefly mined from mineral sands in western Australia, west Africa, south Africa, and the Czech Republic. For many applications that do not require pure or doped TiO₂, the mineral is mined, cleaned, powdered and separated by electrostatic and density sorting to produce 95% pure TiO₂⁴¹, which can be used for applications such as abrasives and welding flux. For pure TiO₂, the Ti⁴⁺ ion is chemically extracted as TiCl₄ by carbothermal chlorination from mined TiO₂ and is reoxidized in a simple synthesis method, such as oxidizing the TiCl₄ in an oxygen flame^{42,43}. Due to the high heat in the oxygen flame, this method produces a mixture of very pure, white, and crystalline anatase and rutile (about 80:20). This can be purchased commercially and is referred to as Degussa P-25 or P-25 equivalent.

Another common method involves the hydrolysis of a Ti(IV) alkoxide, such as titanium isopropoxide (TTIP), to form amorphous TiO₂. This is referred to as a sol-gel method. The simplest method slowly adds TTIP to water, with the acidity of the water controlling the final particle size. At room temperature and pressure, this produces amorphous particles which are then often annealed in order to induce the crystallinity. In the hydrothermal method, this is done in an autoclave at temperatures up to 220°C for as long as 10 hours⁴⁴. This produces crystalline particles, although larger and with less surface area than the room-temperature method.

1.3.2 Doping TiO₂

To incorporate cations (usually transition metal ions) into the TiO₂ lattice, the cations are added to the sol-gel precursors. This can produce material that is truly doped, with the cations

replacing Ti atoms in the lattice, or a material that is co-crystallized, with the metal (often as a salt) forming in electronically isolated pockets within the TiO₂ structure⁴⁵. The latter case has chiefly been studied to improve the photoactivity under UV irradiation, and is often referred to as “surface doped”, since the surface cations can promote the photoactivity by offering reaction sites⁴⁶, promoting charge carrier separation⁴⁷, and preventing particle aggregation to name a few. In short, the chemistry can drastically change depending on the cation, target molecule, and environment. However, metal centers often act as traps and recombination centers for e⁻ / h⁺ pairs, proving detrimental to the overall photoactivity. In general, cationic dopants are stable to the high heat and pressure often used to achieve the crystallinity.

Anionic dopants that have been studied include N, S, C, B, P, I, and F³¹. Anionic dopants tend to dissipate in high temperatures, as most have a stable gaseous form. Since most materials are doped and then annealed to burn out organic precursors and cause the anatase transformation, most of the anionic dopants are driven out as well. Since the focus of the work in this dissertation is on N-doped TiO₂, an overview of N-doping is presented below.

Since 2001, when Asahi et al. first reported photocatalytic activity of N-doped TiO₂¹⁹, there has been a vast number of papers describing N-doping. Several methods have been described to synthesize N-doped TiO₂:

Implantation: This method is used chiefly for single crystals. A crystalline sample of TiO₂ is placed in an ultra high vacuum (UHV) chamber and bombarded with an energetic beam of N ions, at energies up to 30 keV. The final product is then annealed to heal defects created by the bombardment, which often results in the loss of most of the N.

Annealing: A sample of undoped TiO₂ is placed in an oven and heated to 450 – 600 °C under an atmosphere of N₂, ammonia, urea or other N-containing gas⁴⁸.

Hydrothermal Method: This is a method which can create doped, crystalline TiO₂ by autoclaving⁴⁴. The dopant precursors are mixed in a (usually) aqueous solution with TiO₂ particles and heated under high pressure for extended periods of time to incorporate the dopant.

Sol-Gel: N-containing components such as triethylamine (TEA), NH₄Cl, N₂H₄, NH₄NO₃, or HNO₃ are added to the precursors of a sol-gel synthesis^{49,50}.

Methods which use organic precursors will have organic impurities in the final material, which clearly show up in the FTIR . Most groups will anneal the product in air or oxygen to “burn” out organic impurities by converting the impurity to NO_x, SO_x, and CO_x, but this also removes the dopant. Even with annealing, many groups may unintentionally create C-doped TiO₂.

The absorption edge shift in the UV-Vis is often used qualitatively as proof of doping. However, many parameters can cause coloration and therefore a shift in the absorption edge. Oxygen vacancies in the TiO₂ lattice will cause a yellow color to form. TiO₂ is also known to self-dope, where the Ti⁴⁺ is reduced to Ti³⁺ due to some reaction condition, such as heating in a vacuum⁵¹. The Ti³⁺ has a strong blue color. In fact, while pure TiO₂ is colorless and transparent, most naturally occurring TiO₂ single crystals are a deep blue (although they can also be found as yellow, green or red, due to impurities⁵²), as shown in Figure 1.6. An atomic analysis method such as XPS is the the best way to confirm the presence of the dopant. Dopants are referred to as being interstitial or substitutional. Substitutional dopants take the place of an O atom in the TiO₂ lattice. For N, the N 2p state ends up slightly above the VB of TiO₂, and gives us the lowered

bandgap⁵³. Interstitial dopants force their way into the lattice, often creating grain boundaries. Bandgap lowering is still observed, but due to the N-O π^* orbital⁵⁴, which is injected as a midgap state in slightly above the conduction band. In XPS, a N(1s) peak position can be used to distinguish between substitutional and interstitial N. This is discussed further in Chapter 3.

1.3.3 Effect of Fluoride

Shape Control: In 2008, it was reported that Ti foil etched with hydrofluoric acid (HF) produces nanorods of TiO₂⁵⁵. It has since been widely reported that including HF in the synthesis (especially hydrothermal synthesis methods) can affect the shape of the resulting nanoparticles, and is used to create particles with high-index facets exposed²⁸.

Bulk Fluorination: Bulk fluorination can be achieved through sol-gel methods or implantation. The result is a mix of TiO₂ and TiOF₂. The multicoordinate F results in a distinct XPS peak, and TiOF₂ is readily identified in an XRD or raman spectra. It has been shown theoretically and experimentally that the bandgap does not change, as the extra levels are inserted below the VB of TiO₂⁵⁶. However, many groups still report an increase in the visible light photoactivity.

Surface Fluorination: In an aqueous solution, the surface of TiO₂ is hydroxyl terminated, which can be protonated (>Ti-OH₂⁺) or deprotonated (>Ti-O⁻) depending on the pH of the solution. Fluorinating is not difficult, simply suspending the particles in an acidic solution of HF⁵⁷ is sufficient, and the hydroxyl groups are exchanged for Ti-F groups. Although F is more electronegative than O (3.98 and 3.44, respectively, on the Pauling scale), the Ti-F and the Ti-OH bond have similar bond dissociation energies (109±5 and 105±2 kcal mol⁻¹, respectively^{58,59}). It has been shown that surface fluorination does not affect the bulk structure or optical properties,

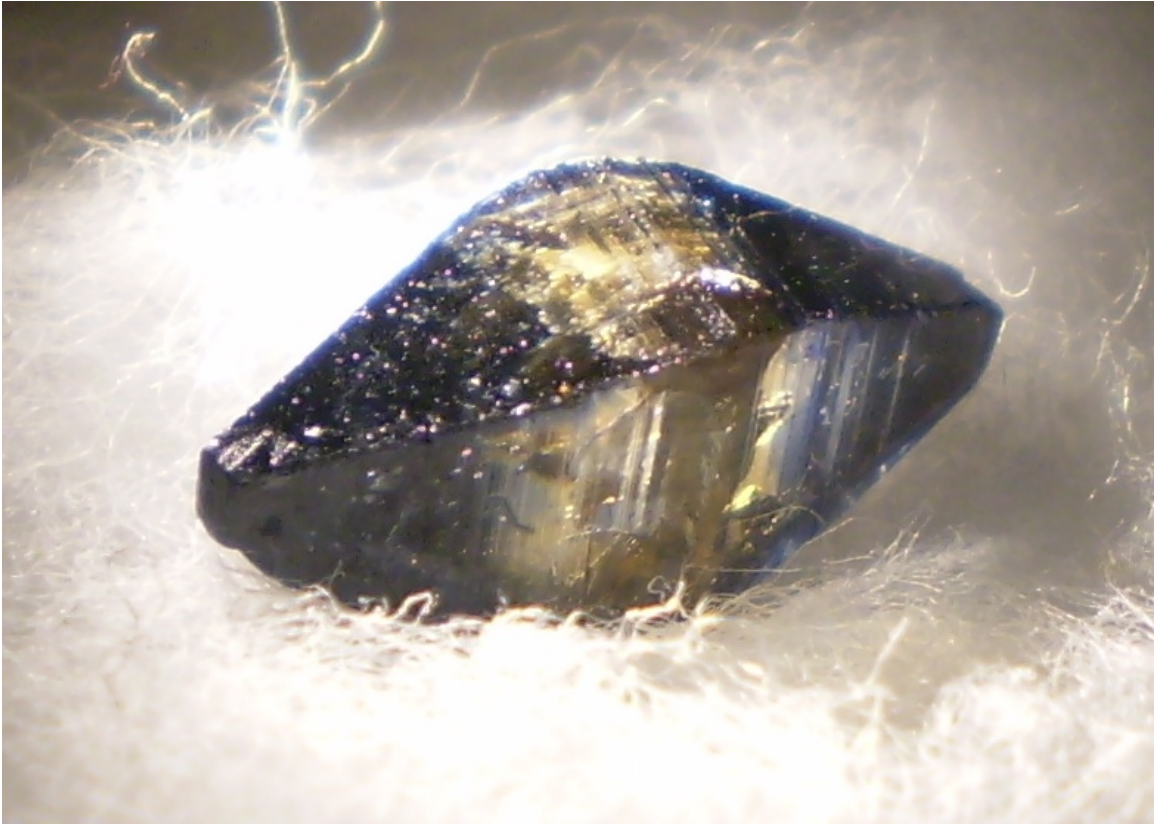
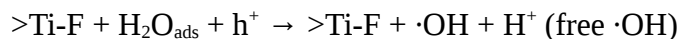
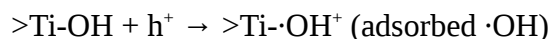


Figure 1.6: Photograph of a naturally occurring anatase crystal mined in the Czech Republic.

but since the charged surface OH groups are removed and replaced with neutral F, the interaction with polar molecules is enhanced⁶⁰. Additionally the production of ROS, especially ·OH, is increased⁶¹, promoting systems that depend on remote photoactivity. This is partially due to the enhanced mobility of the ·OH from fluorinated TiO₂⁶²⁻⁶⁴:



Additionally, the absorbed F shifts the flat-band potential by up to 2 V⁶⁵ to facilitate transfer of a CB e⁻s to H₂O or OH⁻, creating more radicals.

1.4 Prior Photoactivity Experiments

The potential applications for TiO₂ photoactivity seem limitless, and the methods employed to quantify that photoactivity are equally broad. It has become clear from this broad base of work that modifications such as N-doping or surface fluorination may improve the photoactivity for some systems and affect others detrimentally.

One of the most active research areas involves use of the TiO₂ to decompose pollutants. To probe this, researchers use a model compound and either measure the increase in decomposition products (CO₂) or the decrease in reactants as the sample is illuminated with light. Methylene blue (MB), 4-chlorophenol, trichloroethylene, and many others are used as model compounds. The rate of photodegradation is reported under various conditions, but since the light flux, pH, temperature, concentrations, and other conditions vary greatly from one lab to another, results are not easily comparable.

1.4.1 Methylene Blue

3,7-bis(Dimethylamino)-phenothiazin-5-ium chloride, (shown in the first pane of Figure 1.7) commonly known as Methylene Blue (MB) is a cationic dye that's been well studied for over 100 years, chiefly due to its antiseptic use in medicine. Although not widely used in medicine anymore, MB is still widely used as a cellular dye in biology. MB is also widely used as a probe molecule to measure TiO_2 photoactivity due to its good solubility, ionic nature, and strong color, which makes for easy monitoring of the concentration.

There are two general decomposition routes reported in the literature, loosely called demethylation and ring cleavage. The experimental conditions, especially the pH, prescribes which mechanism dominates.

The first step in the demethylation mechanism is the reaction of the CB e^- s or ROS with the N- CH_3 bond, which is the lowest-energy bond in the MB molecule⁶⁶. This is characterized by a blueshift in the MB peak in the UV-Vis as the electronic environment of the conjugated π system of the MB molecule changes. This reaction path is shown in Figure 1.7, with the maximum absorbance for each species noted. Since the UV-Vis spectrum is the sum of the absorbing species, the peak shape can be used to derive the percent concentration of each species present⁶⁷.

The ring cleavage pathway, shown in Figure 1.8, involves the reaction of VB h^+ s or ROS directly breaking the π system⁶⁸, causing the coloration to disappear. Since the color-giving π system is broken in the first step, this pathway shows a much greater rate of color disappearance. This pathway is characterized in the UV-Vis by a decrease in the signal without a shift in the peak maximum.

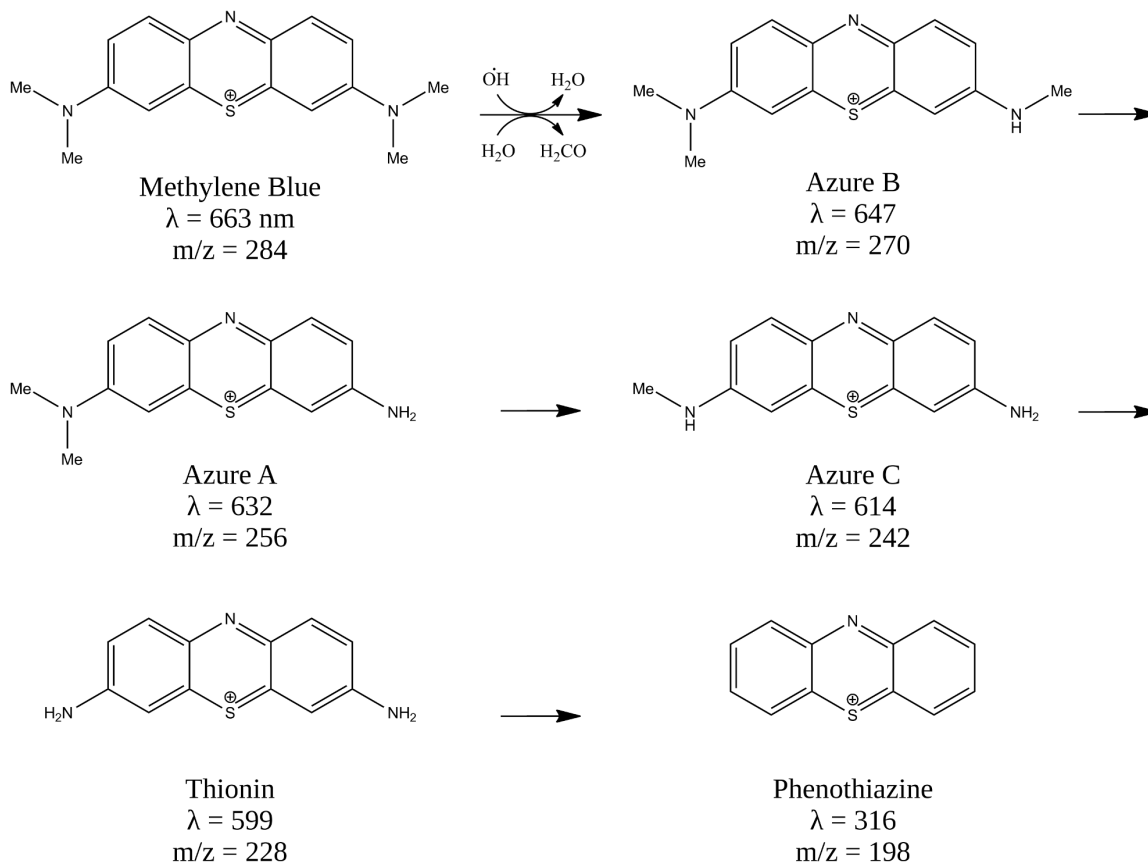


Figure 1.7: Scheme showing the decomposition of MB by the demethylation pathway. The names, maximum absorbance, and molecular weight of the intermediates are noted.

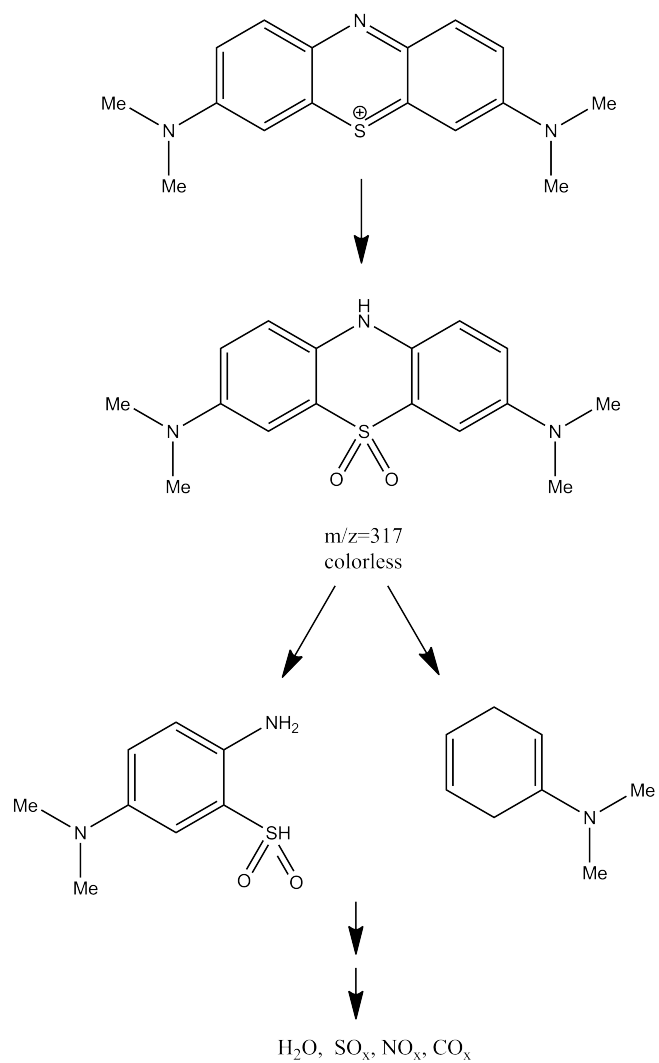


Figure 1.8: Scheme showing the decomposition of MB by the ring cleavage pathway.

The demethylation pathway is generally accepted as the most predominant under most conditions, however this is a dynamic system and it has been shown that both mechanisms can work concurrently⁶⁹.

MB is used due to its strong color, which disappears quickly during a reaction. One should keep in mind that the disappearance of the color is only the first step in the complete mineralization of MB to H₂O, CO₂, SO_x and NO_x. To measure the rates involved with complete mineralization, the formation of CO₂ needs to be monitored. However, the disappearance of the blue color is widely used as an indicator of the photoactivity.

1.5 Outline of this Dissertation

Although there is a vast body of work on this system, it is clear from the amount of conflicting information in the literature that the photoactivity of TiO₂ holds a hidden complexity. With the large amount of work that has been done also emerges a large number of realized and potential applications, which merits continued study in this area. Therefore, the motivation was to synthesize and characterize a N-doped TiO₂ powder with a narrowed bandgap that shows increased photoactivity over standard, undoped TiO₂. Based on research that shows the effect of surface doped F, the effect of surface F was investigated as well. Published reports often show a “sweet spot” for the concentration of incorporated dopant, where the activity is greatest. This lead to the development of a method that allows independent control over the N and F concentrations. This research stayed focused on room-temperature methods that do not require dangerous reagents such as HF as a reagent or high temperature, high pressure reaction vessels.

To this end, many sample sets were prepared by sol-gel methods and tested for photoactivity. Chapter 2 will provide an outline of the the characterization methods used.

Chapter 3 will review the synthesis methods and characterization of the TiO₂ product. Chapter 4 will present the effect of F on the crystallinity of TiO₂. Chapter 5 will present the results of photoactivity experiments and will show the effect of N-doping, N,F-doping, and F surface doping on the photoactivity of TiO₂. Chapter 6 will summarize the conclusions drawn from this body of work. Additional experimental results are provided in Chapter 7.

CHAPTER 2 - EXPERIMENTAL METHODS

2.1 X-Ray Photoelectron Spectroscopy

X-Ray Photoelectron Spectroscopy (XPS) spectra were measured using a Kratos Axis 165 X-ray photoelectron spectrometer. The X-ray source was a Al $\kappa\alpha$ monochromatic x-ray (1486.7 eV) operated at 150 W (15 kV at 10 mA) and the spectra were collected with a pass energy of 80 eV in hybrid mode. The base pressure of the system was 2×10^{-9} Torr. Samples were mounted one of two ways:

For all samples that have atomic percentages reported, the samples were mounted on a 15×15 mm Au coated Si chip. The chip is cut from an 4 inch Si wafer coated with about 100 nm of Au, sufficiently thick so only Au peaks are visible in the XPS spectra of a clean chip. A slurry of the titania to be measured is made by crushing 50 mg of the titania in 3 mL of purified water with an agate mortar and pestle. The Au coated chip is heated to 60 °C on a hot plate, and 0.5 mL (~10 drops) of the TiO₂ slurry is dropped on along with 2 drops of concentrated HCl. The strong acid protonates the surface of the TiO₂, preventing the particle-particle interactions that cause flaking, and providing better adhesion to the Au. The liquid is then allowed to evaporate to dryness, leaving behind a thin, uniform film of TiO₂. The film is thick enough to allow for high quality spectra, and thin enough to dissipate the surface charge inherently created with XPS, thus eliminating the need for charge canceling or charge corrections. The peak areas were calculated using the Kratos software, the Shirley background subtraction method⁷⁰, and a GL(30) peak

shape (30% Gaussian + 70% Lorentzian). Atomic percentages were calculated using the integrated area of the peaks and the sensitivity factors (SF) for the x-ray source positioned at 54.7° to the analyzer, published in the PHI Handbook of XPS⁷¹. Since the signal intensity varies from one sample to the next, intensities could not be directly compared. Therefore, atomic percentages were calculated for N and F relative to the Ti signal, normalizing the data and allowing for comparison between samples.

A faster method for mounting samples that also allows more samples to be run at the same time is the carbon tape mounting system. Powdered samples are pressed into a double-sided piece of conductive carbon tape with a metal spatula. This allows for quick measurements, but charging cannot be controlled. The XPS instrument includes a charge neutralizer, which is a filament from which electrons are extracted and funneled to the sample with a magnetic well to compensate for the photoelectrons lost. This can never be perfectly adjusted, so spectra must be corrected for local charging based on the adventitious C(1s) peak. Also, the amount of sample in the measurements is not easily controlled, resulting in spectra that are hard to compare. The variations also introduce a large amount of error into atomic percentage calculations. Lastly, the C tape introduces extra C and O peaks that add to the TiO₂ signal. However, qualitative information can be obtained fairly quickly and easily by this method.

2.2 X-Ray Diffraction

XRD measurements were done on a Bruker D2 Phaser desktop diffractometer with a Cu $\kappa\alpha$ X-ray and a LynxEye Si strip detector. About 80 mg of the powdered sample was used, with a cup rotation of 5 revolutions per second, X-ray power of 300 W (30 kV at 10 mA), and a primary slit size of 0.6 mm. An air-scatter screen was used.

The intensity of the peak is directly proportional to the amount of crystalline material in the sample well⁷². In other words, if we notice a 2× increase in the signal intensity, we can assume a 2× increase in the amount of crystalline material. If the same amount of sample with the same density is used every time, and instrumental parameters are kept constant, approximations can be made about the relative amounts of crystallinity between samples. To this end, the mass and packing of all samples was carefully controlled. All spectra were collected with ~80 mg of powder pressed into a 10 mm disk on the sample cup.

Crystallite sizes were estimated using the Debye-Scherrer Equation⁷³:

$$\phi = \frac{K \lambda}{\beta \cos(\theta)} \quad (1)$$

Where ϕ is the size of the crystallite in nanometers, K is the shape factor and was set to 0.93 (assuming spherical crystallites), λ is the wavelength of the x-ray in nanometers (0.154079 nm for Cu $\kappa\alpha$), β is the full width at half maximum (FWHM) of the peak in radians 2θ , and θ is the peak position. The crystallites were assumed to be spherical, although some evidence exists that anatase maintains its tetragonal bipyramidal shape (see in Figure 1.6) to extremely small dimensions (3-5 nm)⁷⁴. This estimation will find the lower bound for crystallite size, since instrumental broadening is unaccounted for.

Other factors affect the peak broadening as well, such as surface distortions, grain boundaries and lattice strain⁷⁵. With nanoparticles and nanocrystals it is not unreasonable to expect such line broadening. However since this quantification was not available, it is assumed that the broadening of the peaks is directly correlated to the size.

2.3 UV-Vis Diffuse Reflectance Spectroscopy

UV-Vis Diffuse Reflectance Spectroscopy (DRS) was done with a Shimadzu UV-3600 UV-Vis equipped with a Harrick Scientific Praying Mantis Diffuse Reflection Accessory. The bandgap was estimated as the point of the onset of absorption. To find the bandgap, straight lines were extrapolated from the baseline and slope, as shown in Figure 2.1. The bandgap is the intersection of the extrapolated lines.

2.4 Raman Spectroscopy

Raman measurements were made with a Jobin Yvon LabRAM HR800 UV, with a HeNe laser, 100 μm hole, and a 50 \times objective. Experiments were performed in air.

2.5 Fluoride Ion Selective Electrode

A F⁻ Ion Selective Electrode (ISE) attached to a Orion Research Expandable Ion Analyzer EA940 was used to measure free F⁻ in solution. Since the amount of F⁻ free in solution is affected by the ionic strength and pH of the solution, a total ionic strength adjustment buffer (TISAB II) was used in a 50:50 ratio with the solution to be analyzed to normalize the pH and ionic strength.

2.6 Surface Area Measurement

The surface area was measured by a single point Brunauer-Emmett-Teller (BET) isotherm measurement and estimated using two molecular adsorption methods.

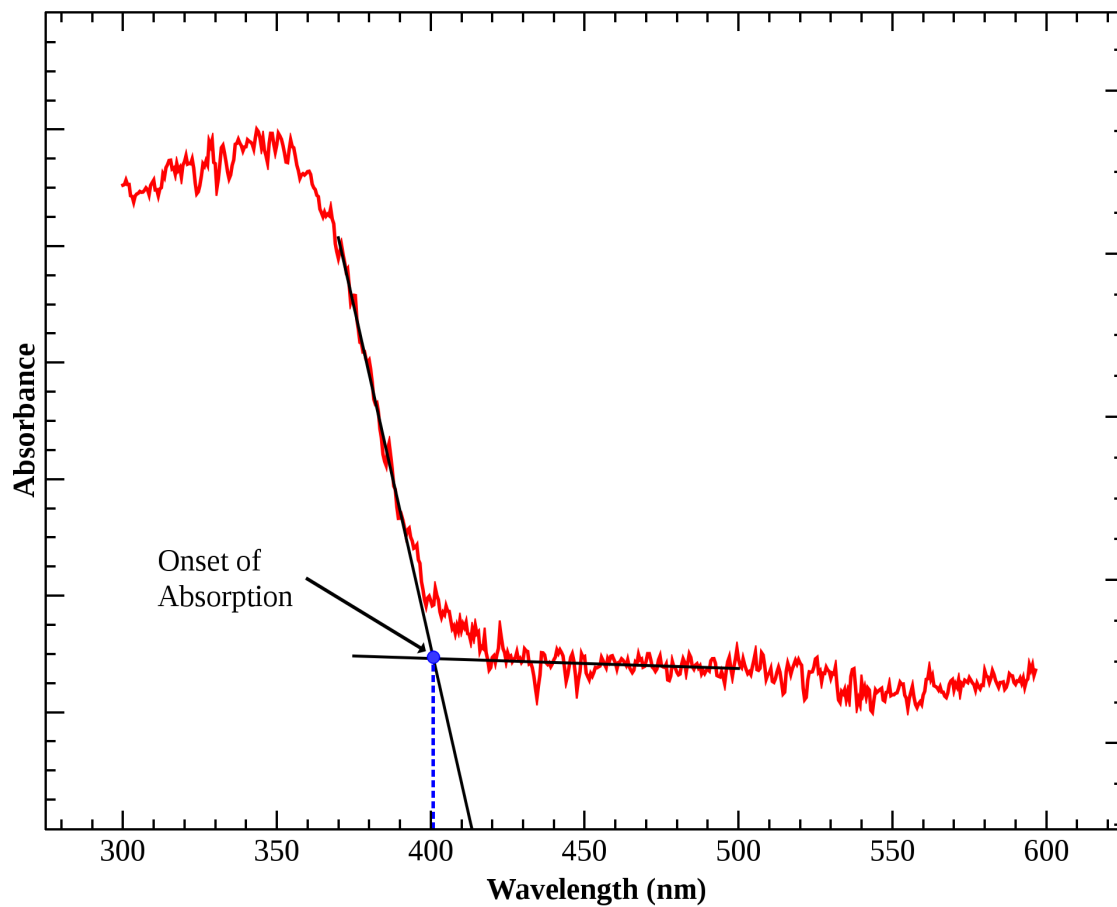


Figure 2.1: Method to estimate the bandgap from UV-Vis data. This shows the DRS for undoped TiO₂, and the bandgap is 400 nm, or 3.1 eV.

2.6.1 Single Point BET

The BET measurements were made with a homemade instrument^{76,77}. About 0.5 g of the sample was placed in a U-shaped glass tube known as the reactor. The amount of sample used was calculated to have an surface area corresponding to about 0.75 mL of N₂ adsorption.

The reactor is pumped out to a pressure of 1×10^{-4} Torr for at least 30 minutes to degas the sample. A precise 30% N₂ / He mix is then flown through the reactor. The partial pressures of N₂ (P_{N_2}) and He (P_{He}) coming out of the reactor are monitored by a quadrupole mass spectrometer (MS) residual gas analyzer (RGA) (Stanford Research Systems RGA 300), shown in Figure 2.2. The sample is then cooled to 77 K with liquid N₂ (lN_2). The P_{N_2} decreases due to the gas contraction due to the temperature change (Figure 2.2.a) (as predicted by the ideal gas law, $PV=nRT$), and then another decrease is seen corresponding to the N₂ adsorption to the powdered sample (Figure 2.2.b). The lN_2 is then removed and replaced with a room temperature water bath. The P_{N_2} then shows a peak corresponding to the gas expansion due to the temperature change (Figure 2.2.c), and then another peak corresponding to the N₂ desorption (Figure 2.2.d). Lastly, 2 precisely calibrated aliquots of pure N₂ are injected, with a volume of 0.5 mL and 1.0 mL, respectively (Figure 2.2.e, f).

By comparing the peak intensity of the N₂ desorption (Figure 2.2.d) to the reference aliquots, the volume of N₂ desorbed (V) can be calculated by assuming a linear relationship between volume and peak intensity. The volume of the N₂ monolayer (V_m) can then be calculated by the equation

$$V_m = V \cdot \left(1 - \frac{P}{P_0}\right) \cdot \left(\frac{T}{273.15}\right) \quad (2)$$

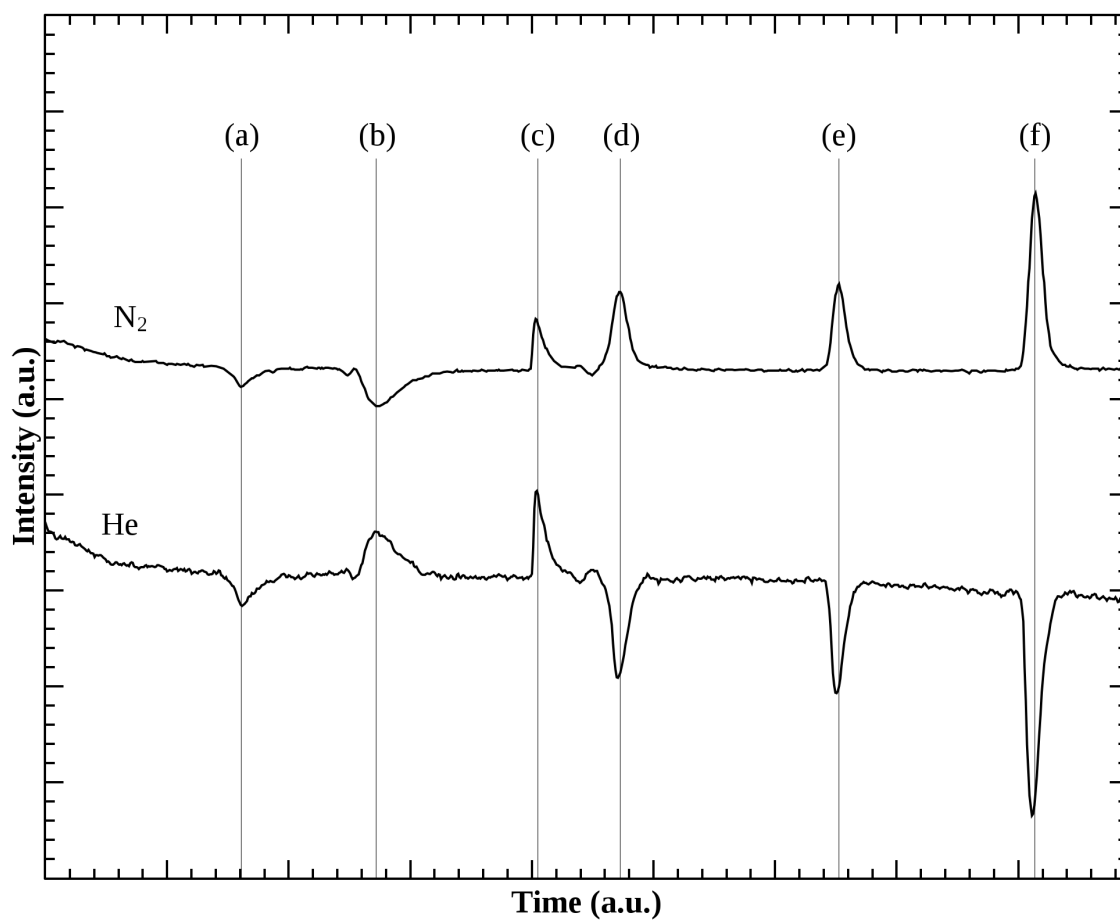


Figure 2.2: Representative BET data. Peaks due to (a) gas contraction (b) N₂ absorption (c) gas expansion (d) N₂ desorption (e) 0.5 mL reference aliquot (f) 1.0 mL reference aliquot.

Where P is the partial pressure of the N_2 , P_0 is the total pressure, and T is the ambient temperature. The total surface area (S_t) can be calculated using the equation

$$S_t = \frac{V_m \cdot N \cdot \delta}{V_s} \quad (3)$$

where N is the Avogadro constant, δ is the cross section of an adsorbed N_2 molecule (16.2 \AA^2), and V_s is the volume of N_2 at STP (22.4 L)⁷⁷.

2.6.2 Molecular adsorption

An estimate of the surface area was obtained by measuring the amount of F^- adsorbed to the particles. Using a F^- ion sensitive electrode (F^- ISE), we were able to measure the F^- ion concentration in the NaF solution before and after fluorination of the particles, the difference being attributed to the amount adsorbed on the particles. It has been reported that F has a surface coverage on TiO_2 of 3-4 F atoms / nm^2 . Assuming complete coverage at an acidic pH, the surface area can be calculated⁷⁸.

A similar method can be applied to MB adsorption. After adding MB to an aqueous solution of TiO_2 and allowing 2-24 hours for the MB to adsorb, UV-Vis can be used to quantify the remaining MB in solution. It can be assumed that at constant temperature and pH, the amount of MB / nm^2 is constant. This change can be used to estimate the relative surface of the TiO_2 samples.

2.7 Fourier Transform Infrared Spectroscopy (FTIR)

Fourier Transform Infrared Spectroscopy (FTIR) was measured with three complementary techniques with three instruments.

Transmission FTIR measurements were made with Nicolet 560 Magna IR spectrometer with a mercury cadmium telluride (MCT) detector. Approximately 5 mg of powdered samples were scattered on a KBr single crystal and placed in the spectrometer which was purged with N₂ for 20 minutes, or until the CO₂ signal was steady. Two hundred scans were averaged and had a background scan (just the KBr crystal) subtracted from them.

Attenuated Total Reflectance (ATR) FTIR measurements were made with a Jasco FT/IR 4100 spectrometer equipped with a PIKE MIRacle™ single reflection ATR with a ZnSe crystal. Collected data is the average of 64 scans at 1 cm⁻¹ resolution. Experiments were done in air, with the background subtracted out to remove the signals from CO₂ and H₂O.

Diffuse Reflectance Infrared Fourier Transform Spectroscopy (DRIFTS) measurements were done with a Bruker Vertex 70 FT-IR with a Harrick Scientific Praying Mantis Diffuse Reflection Accessory. About 1 mg of powdered sample was mixed with about 100 mg of powdered KBr. Since the KBr is transparent to IR, more surface area of the sample is exposed, thus increasing the signal and decreasing the amount of sample needed. The apparatus was purged with N₂.

2.8 Photoactivity

TiO₂ samples were also tested for photoactivity by monitoring the photodegradation of methylene blue (MB). These samples were prepared by grinding 6 mg of TiO₂ powder with an agate mortar and pestle with 1 mL of purified water. Control experiments revealed by XPS that grinding with a standard mortar and pestle added a significant amount of silica to the sample. An additional 4 mL of water was added to create a slurry. NaOH was added to adjust the pH to 8. 1.00 mL of this slurry was then mixed in a quartz cuvette with 2.00 mL of purified water and 100

μL of MB solution (1.6×10^{-3} M MB in water, Aldrich). This brought the total concentration of MB to 5.2×10^{-5} M.

When MB and TiO_2 are introduced, some amount of MB will adsorb to the surface of the particles and the walls of the cuvette until an adsorption equilibrium is reached. This can take 1-4 hours. Since the UV-Vis is only sensitive to molecules free in solution, molecules adsorbing to the TiO_2 will decrease the UV-Vis signal. To ensure a stable baseline, solutions were allowed to equilibrate in the dark for 2 – 24 hours before irradiating. The adsorption was monitored by UV-Vis and considered complete when the percent change was less than 2%/hr.

The samples were then placed in the beam of a 300 W Xe arc lamp (R 300-3, ILC Technologies). The lamp was equipped with a water filter in a glass brick to filter out most of the infrared radiation (heat). Since it is well known that TiO_2 is photoactive in the UV range, a UV longpass filter (400 nm, Edmund Optics) was added, allowing only visible light to pass, and therefore measuring only the contribution from visible light absorption of the TiO_2 . It is also known⁷⁹, but not widely reported, that MB will autodecompose when exposed to high flux radiation in its absorption ranges ($180 < \lambda < 340$ nm and $550 < \lambda < 700$ nm). To counter this, a visible shortpass filter (560 nm, Omega Optical) was added.

The final arrangement of filters only allows light between the wavelengths of 400 and 560 nm to pass, which avoids the normal adsorption ranges of TiO_2 and MB. Figure 2.3 overlays the absorption spectra for undoped TiO_2 and MB with the filter setup transmittance to show the small overlap of the TiO_2 and MB with the transmitted light. This means that the only degradation detected will be due to the increased absorption of the TiO_2 . During irradiation the samples were stirred with a magnetic stir bar to prevent the TiO_2 from settling out, which would

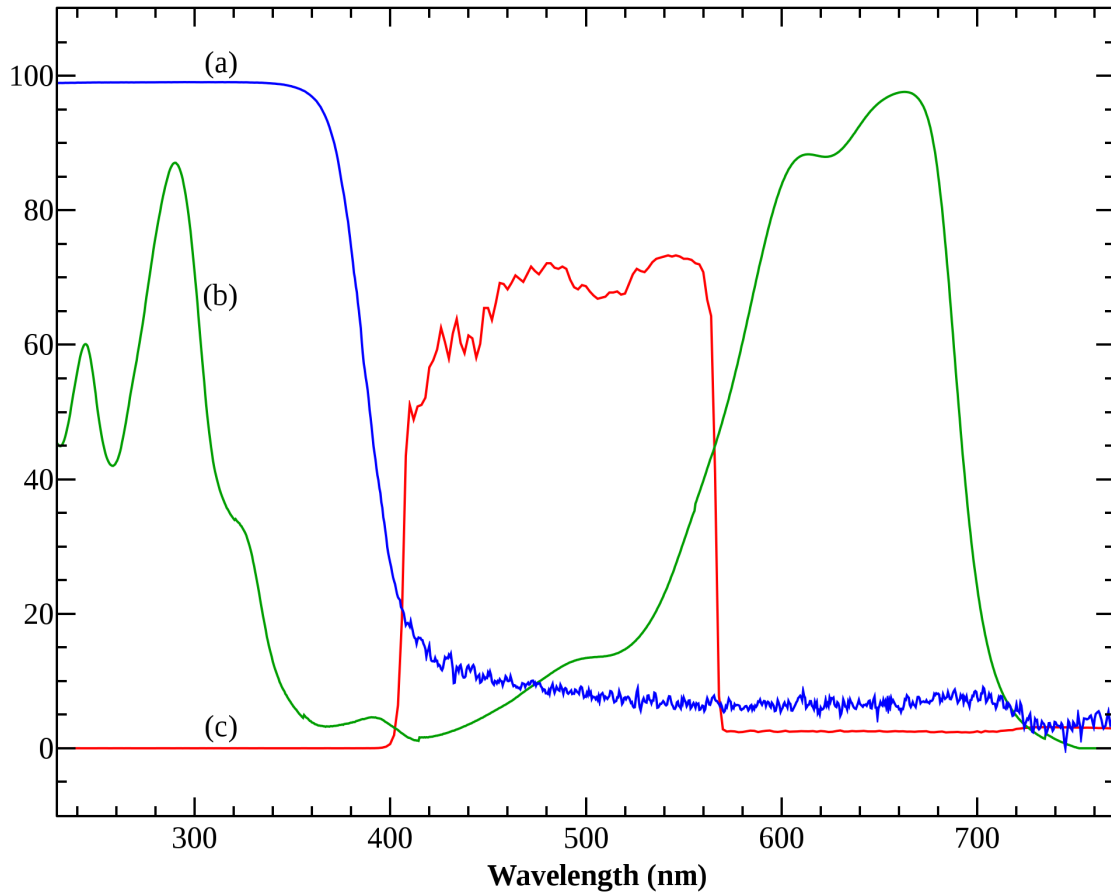


Figure 2.3: Diagram of the filter setup. (a) shows the absorption of pure (undoped) TiO_2 , (b) methylene blue and (c) shows the percent transmittance of the filter combination.

remove them from the beam path of the lamp. The cuvettes were open to air during irradiation.

The extent of MB degradation was monitored with a Beckman Coulter DU800 UV-Vis spectrophotometer. The maximum peak for MB is at $\lambda=664$. A normal process of degradation involves the demethylation of MB (see §1.4.1 , page 19) which blue shifts the absorption peak. To quantify the amount of methylene blue in solution, the maximum value from the range 660-670 nm was used. Since the baseline changes while the reaction is progressing (due to degradation intermediates causing clouding and the particle sizes changing due to constant stirring, which changes the scattering), $\lambda=750$ was used as a point where MB has no absorption, and the amount of MB remaining was quantified as the absorption at $\lambda=664$ minus the absorption at $\lambda=750$. This was then compared to a calibration curve, shown in Figure 2.4, to extract a value for the remaining concentration of MB. Due to the high concentration variance involved (more than an order of magnitude) and the tendency of MB to dimerize at high concentrations, the calibration curve is non-linear. The concentration of MB in solution can be calculated fairly accurately by the exponential fit to the calibration curve:

$$[\text{MB}] = -\ln\left(1 - \frac{A_{\lambda=664} - A_{\lambda=750}}{4.71}\right) \cdot 5.50 \times 10^{-5} \quad (4)$$

Since the initial amount of absorbed MB varied depending on pH, particle size, particle PZC, and particle surface area, the amount of MB was normalized to 1 (or 100%) at time=0 (after equilibrium period, but before any irradiation) for comparison purposes. This was then fit to an exponential decay function:

$$\frac{[\text{MB}]_t}{[\text{MB}]_{t=0}} = e^{-k \cdot t} \quad (5)$$

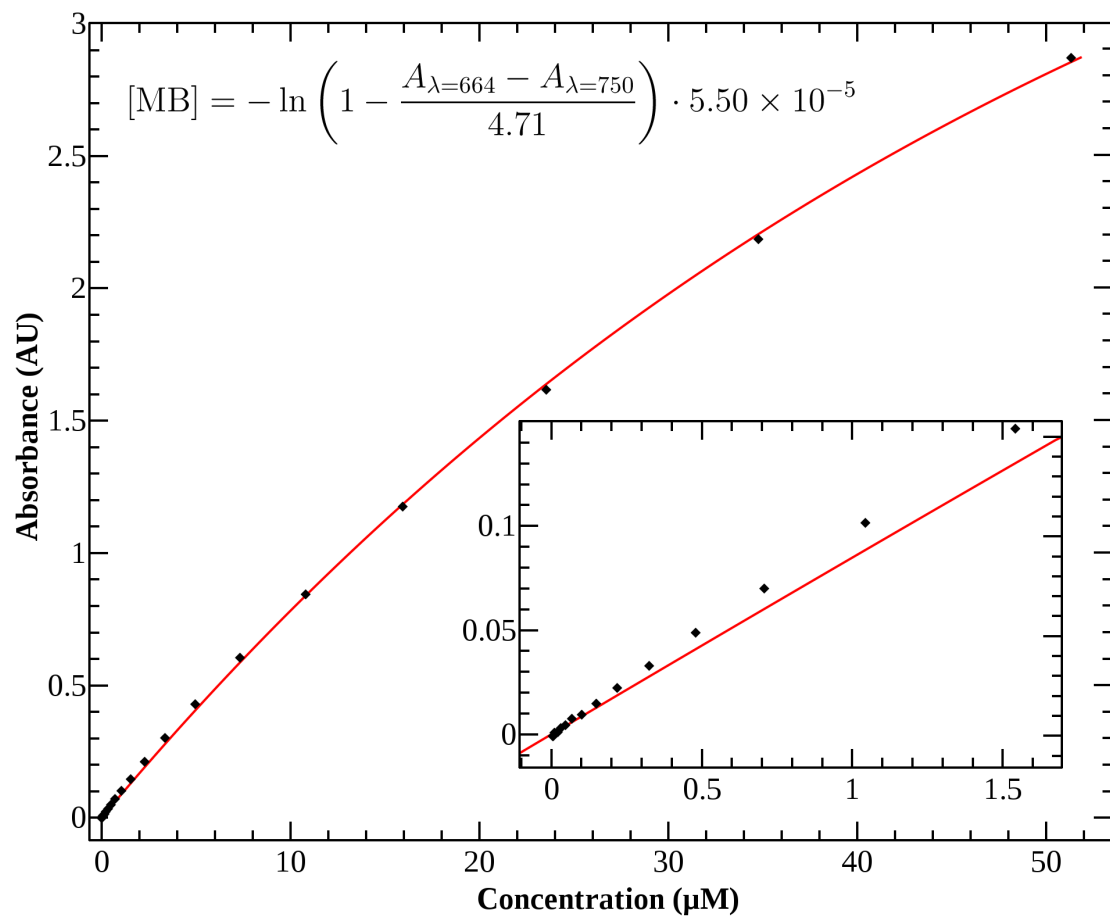


Figure 2.4: Calibration curve for MB. The line is an exponential fit to the data, with the equation shown. The inset shows the deviation at low concentrations.

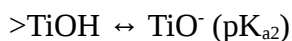
using a scaled Levenburg-Marquardt algorithm^{80,81} with a tolerance of 0.0001. This allows the pseudo first-order rate constant (k) to be extracted, which can be used to compare the activity of various samples.

A representative raw data spectra is shown in Figure 2.5.a. The extracted values for the concentration of the remaining MB is shown in Figure 2.5.b, and the normalization, fit and extraction of the pseudo first-order rate constant is shown in Figure 2.5.c.

It is known that in low oxygen environments, MB is often photobleached to form leucomethylene blue (LMB)⁸² which is the reduced form of MB, and colorless. LMB is oxidized back to MB in the presence of dissolved O₂. This is especially prevalent with a reducing agent in the solution, such as triethylamine⁸³. To check if this phenomenon is present, the UV-Vis spectrum is measured before and after a 2-hour wait while open to air. During that time, atmospheric O₂ would dissolve into the solution and cause the color to regenerate. The photobleaching effect was not observed during this work, indicating that the rate-limiting step was not related to the availability of dissolved O₂.

2.9 Point of Zero Charge

The point of zero charge (PZC) is the pH at which the surface charge of the particles is zero. The surface of TiO₂ particles has exposed O atoms which can be protonated. This causes TiO₂ to act like a diprotic acid in aqueous solutions, as depicted below:



Thus, the pH of the solution determines the surface charge on the particle. A charged particle will form a double layer and will exhibit coulombic interactions with other charged particles,

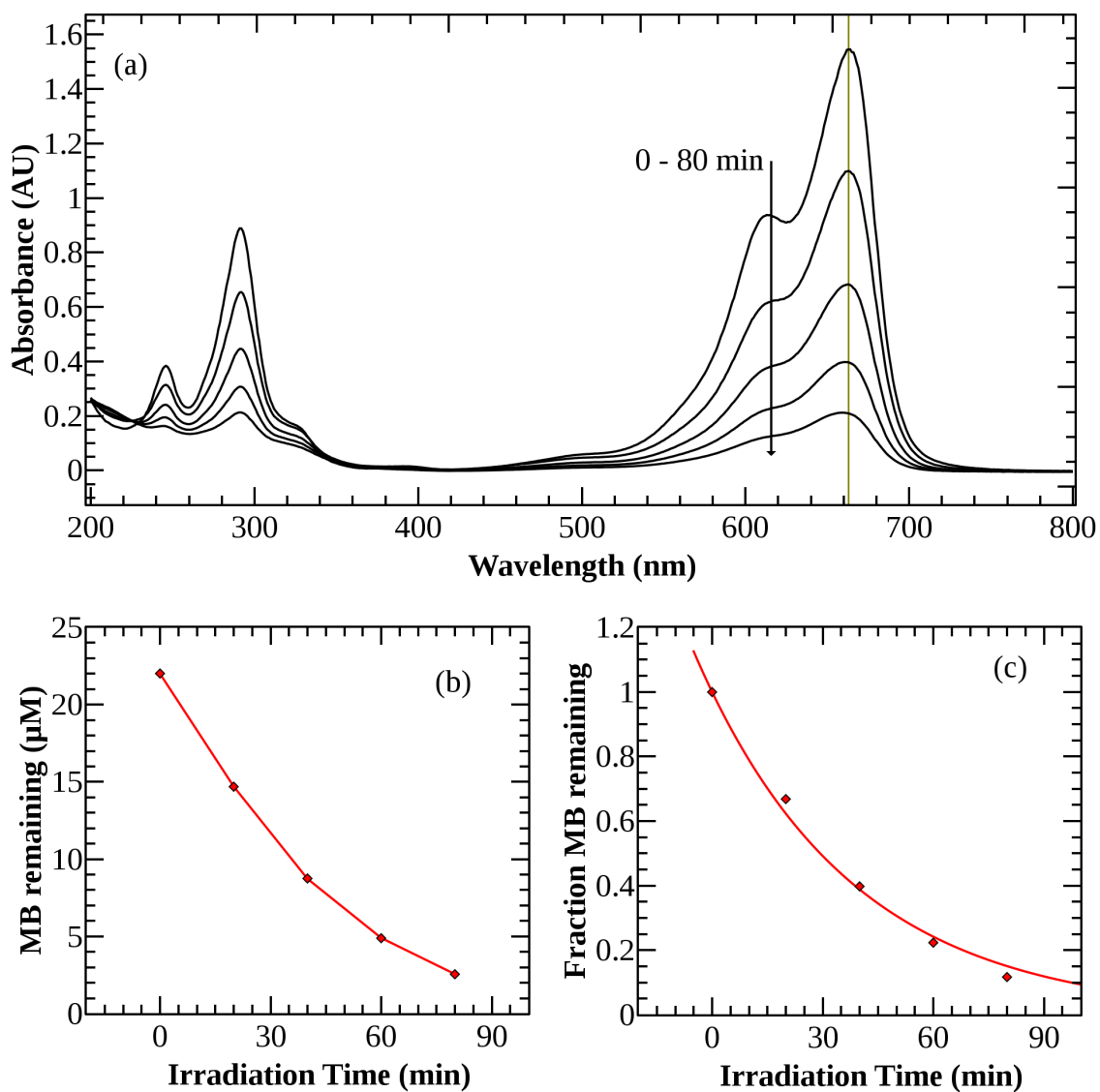


Figure 2.5: Method for extracting rate constants from raw UV-Vis data. (a) shows the raw UV-Vis data, as the MB is irradiated the concentration falls. (b) shows the conversion to concentration. (c) shows the fit to an exponential decay.

including the analyte molecules. This translates into a shift in the measured pH value.

The PZC was measured by the common intersection point (cip) method^{84,85}. A suspension of 180 mg of TiO₂ powder in 9 mL of purified water (2% w/w) was prepared and split into 3 aliquots. Each aliquot had NaCl added to bring the concentration to 0.1, 0.01, and 0.001 M, respectively. Aliquots were then titrated with 0.01 M HCl, also made with the NaCl solutions, recording the pH after each addition. This was repeated with 0.01 M NaOH and plotted. Since the measured pH will not be affected at pH_{PZC}, the pH where the three NaCl concentrations intersect is reported as the PZC.

This effect can be quantified by the Esin-Markov coefficient

$$\beta = \left(\frac{\partial \text{pH}}{\partial \log a_{\text{salt}}} \right)_{\sigma_0} \quad (6)$$

where β is the additional contribution to the pH measurement, a_{salt} is the salt concentration, and σ_0 is the surface charge of the material. At the PZC of a material, β is equal to 0, so the contribution from the salt goes to 0, meaning the same pH value is measured independent of the salt concentration. A representative graph is shown in Figure 2.6.

An error of ± 0.5 pH unit can usually be assumed with this measurement⁸⁵. This is due to the intrinsic error in pH meters with low ionic strength solutions, the changing concentrations of TiO₂, changing ionic strength due to the acid salt addition, the effect of impurities, and the vast number of circumstances that can affect a materials' PZC. The error can be reduced with added titrations at more salt concentrations. More precise measurements are available, but the cip method provides an estimation method that can be easily preformed in the lab with existing equipment.

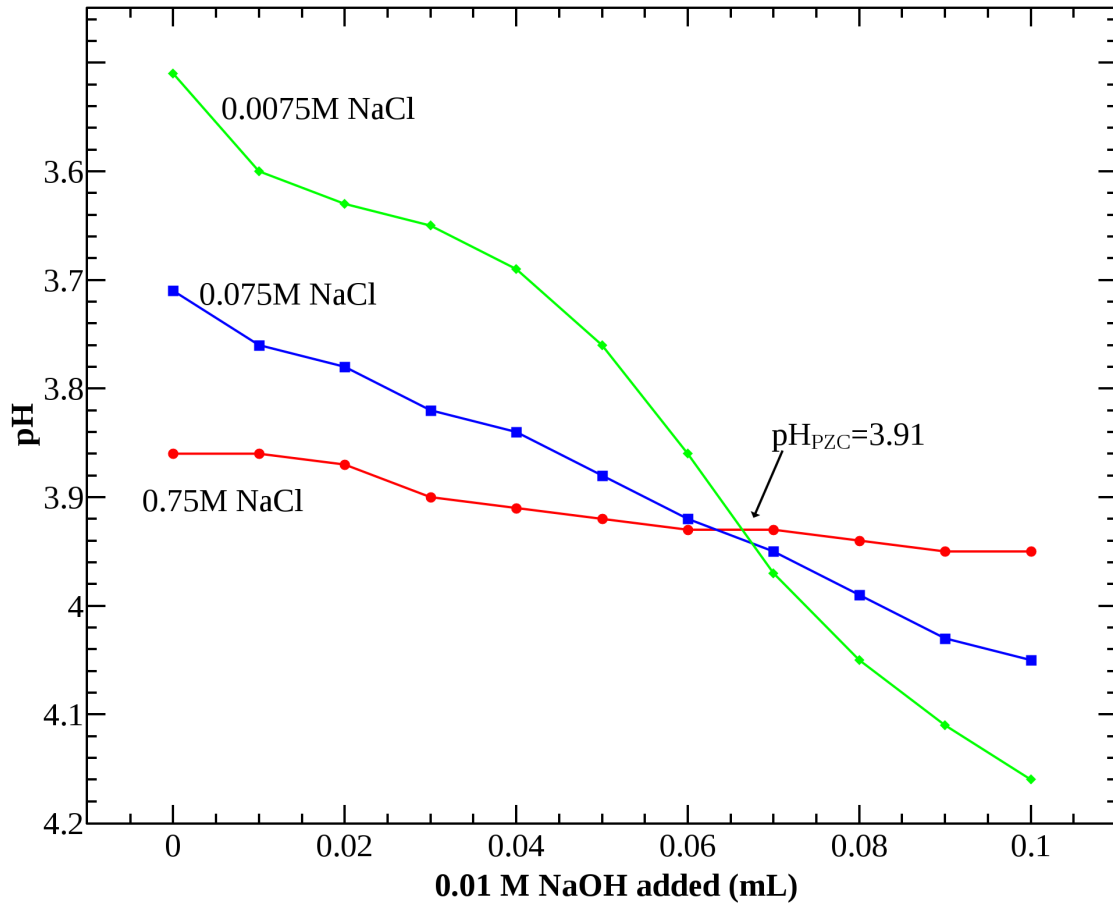


Figure 2.6: Method to find the PZC of a material. The effect of the salt concentration on the pH is measured. The intersection point indicated shows where the salt has no effect on the pH.

2.10 Auger Electron Spectroscopy

Auger Electron Spectroscopy (AES) was done with a PHI Auger system updated with a RBD Instruments package. The base pressure of the system was 2×10^{-9} Torr. The sample was mounted on a Au-coated Si chip by the same method described for XPS (§2.1). The electron gun was set to 3 kV and 0.1 mA emission current.

2.11 Electrospray Ionization Mass Spectrometry

Electrospray Ionization Mass Spectrometry (ESI-MS) was done with a Bruker HCTUltra PTM discovery system.

The ESI technique is known as a “soft” ionization technique. Compared to “hard” ionization techniques, which breaks the parent molecule into secondary ions during the ionization process, soft techniques allow the parent ions to be analyzed. However, this means that species that are not already charged (i.e. salts) generally are not ionized and therefore are not detected. For this reason, MB shows up but many of the degradation products do not.

The ESI-MS uses a spherical ion trap. This provides high sensitivity, but also discards intensity information, meaning the peak intensities are accurate relative to one another, but without an internal standard accurate information about the concentration of an analyte cannot be gleaned. Data is presented as counts per second (CPS) which gives a good approximation of the relative concentrations.

For the experiments described in this dissertation, 100 μL of solution used in the photoactivity experiments was removed from reaction cuvette, added to 400 μL of purified water

in a 1.5 mL micro-centrifuge tube, bringing the total concentration of MB no more than 1×10^{-5} M. These were centrifuged at 7,000 RPM for 20 minutes to separate the TiO₂ particles, and a 250 μ L aliquot was drawn for sampling. The sample line and electrospray needle was flushed with 100 μ L of the sample before data was collected. The injection speed was 150 – 400 μ L/hour, and the final result was a 60 second average. The source was set to 5 nA, and the nebulizer gas was N₂, set to 10 psi, 5 L/min, and 250 °C. MB is known to demethylate easily in the ionization process, and even in these relatively mild ionization conditions the spectra of pure MB shows signals for Azure B and Azure A, at about 16.7% and 7.6% of the MB parent peak, respectively.

2.12 Thermogravimetric Analysis

Thermogravimetric Analysis (TGA) was done with a TA Instruments TGA 2950 thermogravimetric analyzer. About 10 mg of sample was used. The balance pans were cleaned with a propane torch prior to the measurement. The heat rate was set to 10 °C/min, with a 30 minute isotherm at 75 °C to remove residual water. Experiments were run under flowing air to facilitate the mineralization (“burning”) of organic residues to CO₂.

CHAPTER 3 - TiO₂ SYNTHESIS

Although a vast number of synthesis methods have been described, for this work the goal was to use a method that produced N-doped TiO₂ powder with a high surface area at room temperature and without dangerous reagents.

To compare the effect of the N source, N-doped TiO₂ powder was synthesized by two similar methods, using organic and inorganic precursors. The synthesis procedures and characterization of the product is outlined below.

3.1 Chemicals

All chemicals were used without further purification. All water used in the synthesis, washing, characterization, or anywhere else was doubly deionized water from a Barnstead EASYpure LF water purification system. This produced water with a resistivity of 18.3 MΩ·cm, and is hereafter referred to simply as purified water.

3.2 Organic Precursors (TEA)

This synthesis was done with an organic N source and an organic acid. Samples from this synthesis are hereafter referred as TEA, in reference to the N source.

3.2.1 Synthesis

The synthesis method is loosely based on a method published by Gole et al⁵⁰. All reactions were done at 0 °C. A titanium solution was made by mixing 47 mL of titanium

isopropoxide (TTIP) (97%, Aldrich) with 10 mL 2-propanol (IPA) (HPLC grade, Aldrich), and placed in an addition funnel. In a 500 mL three neck flask below it 250 mL of purified water (18.3 M Ω ·cm, Barnstead EASYpure LF) was mixed with 80 mL glacial acetic acid (Aldrich) to bring the pH to 2.0. The 3-neck flask was then placed in an ice bath, allowed to cool to 2°C. The entire setup is shown below in Figure 3.1. Note that the 3-neck is placed at an angle, so the drop from the addition funnel does not fall into the center of the vortex (F) created by the magnetic stir bar. The far right port (C) is connected to a low-pressure, low-flow N₂ feed. Since the TTIP reacts immediately with water, running this reaction in air would cause the petcock on the addition funnel to quickly clog with TiO₂, as the TTIP reacts with atmospheric water. The middle port (D) on the 3-neck is a vent to allow N₂ to escape, and also serves as port for the thermocouple wire (E), whose end is submerged in the liquid. A small amount of desiccant (A) is placed above the addition funnel to prevent atmospheric water from reacting with the TTIP.

Samples were made by the dropwise addition of the TTIP solution under vigorous stirring. This produced a transparent nanocolloid solution, which is stable for years at 0° C. Stirring the nanocolloid solution for 6 hours at 45 °C allows most of the water and IPA to evaporate, leaving a opaque gel. This was then placed in an oven set at 80 °C overnight to dry. The powder had the appearance of large white crystals (no crystallinity is seen in an XRD spectra) and was then crushed with a mortar and pestle, mixed with purified water, agitated, and centrifuged at 3,000 RPM for 10 min. The supernatant was discarded, purified water added again, the powder re-suspended, and centrifuged again. This was then dried in a vacuum chamber (base pressure of 10⁻² Torr) overnight. This sample was labeled “pure TiO₂”.

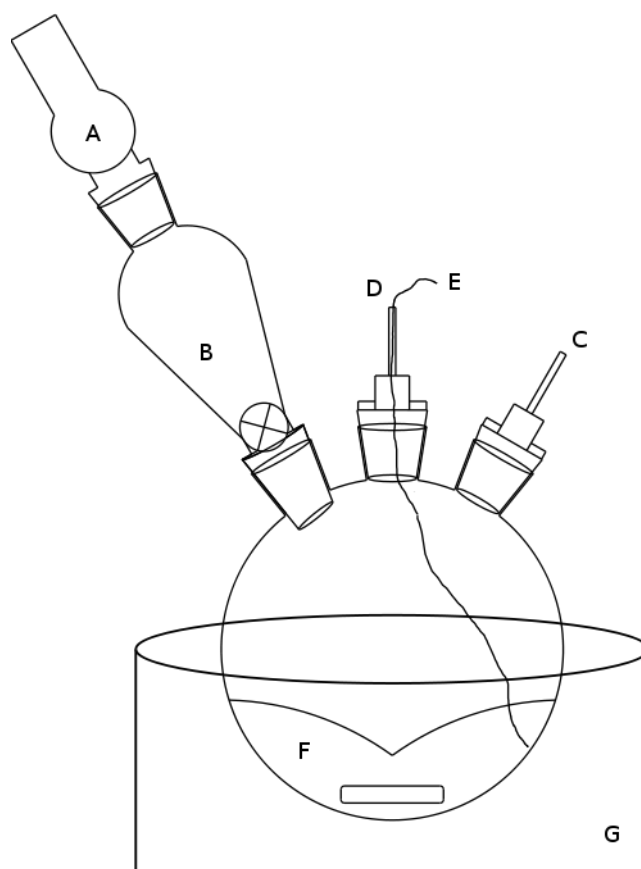


Figure 3.1: Setup for TiO_2 synthesis. See text for details.

3.2.2 Surface Area

Samples were measured by using the BET method (§2.6), and were centered around 80 m²/g. This is consistent with published results for sol-gel synthesis methods and better than P-25 TiO₂ at 48 m²/g⁸⁶.

3.2.3 Purity

The purity of the synthesized samples was measured by XPS, EPR and FTIR. EPR measurements (not shown) reveal only trace amounts of Cu and V impurities were present. Since the water used in these experiments was purified tap water, which is piped through stainless steel pipes, this is the most likely source of the impurities. In any case, the impurities are extremely minimal at an estimated molar percentage of 0.001% (from EPR, since this is well below the detection limit for XPS).

Organic impurities are not seen with XPS or EPR, since the C and O signals are omnipresent from atmospheric CO, CO₂ and H₂O. However, organic moieties can be seen in FTIR, shown in Figure 3.2. Residual hydrocarbons are seen between 1200 and 1800 cm⁻¹, with the major peaks identified as residual acetic acid and triethylamine from the synthesis⁸⁷. The peaks around 2300 cm⁻¹ are due to atmospheric CO₂, and the broad peak between 3000 – 3500 cm⁻¹ is due to the stretching mode of absorbed water. The sharp peak at 1470 cm⁻¹ is due to the asymmetric bending of C-H bonds⁸⁸. The porous nature of the particles makes it impossible to rinse the acetic acid out. In fact, even after a week in the vacuum drying chamber, the smell of acetic acid was obvious in the samples. This was also evident in the mass spectra, where a peak for isopropyl acetate (m/z = 102), the reaction product of acetic acid and IPA, was seen (Figure 5.7). Additionally, a 45% mass loss was seen in the TGA, shown in Figure 3.5. In short, the

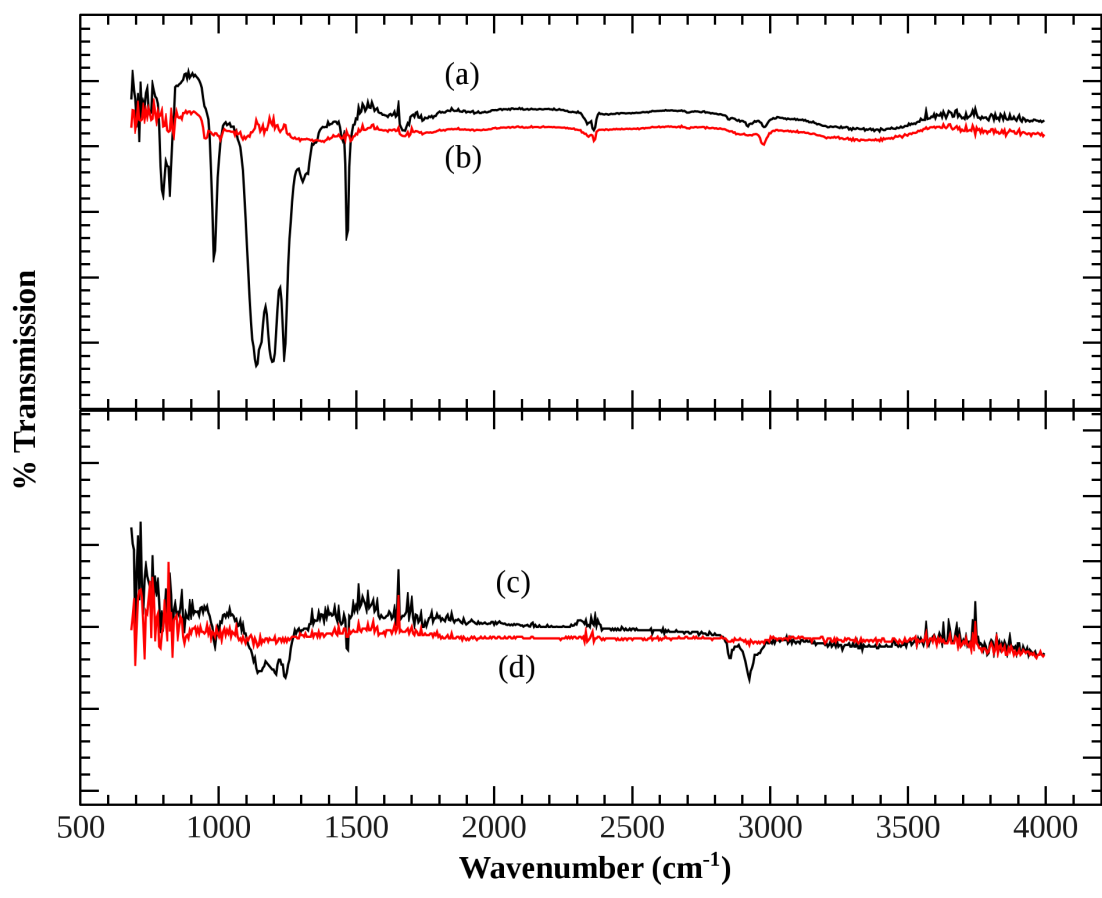


Figure 3.2: FTIR spectra of TEA sample. (a) shows the N-doped TiO₂ before and (b) after annealing to 300°C for 6 hours. (c) shows N,F-doped TiO₂ before and (d) after annealing.

samples were contaminated with a large amount of organic impurities.

Also shown in Figure 3.2 are the spectra for the annealed versions. As expected, annealing significantly reduced the organic impurities.

3.2.4 Doping

To produce N-doped samples, 30 mL of triethylamine (TEA) (Aldrich) was added to 62 mL of nanocolloid solution under vigorous stirring. This exothermic reaction caused the temperature of the solution to jump by 40° C and immediately turn into a dull yellow gel. This was dried as above to produce large, bright yellow crystals. This sample was labeled “N-doped TiO₂”.

To produce N and F-doped samples, 46 mg of NaF was added at 0 °C to the nanocolloid solution and stirred for 5 minutes to dissolve. TEA was then added as before. This sample was labeled “N,F-doped TiO₂”.

The presence of the dopants was verified with XPS, shown in Figures 3.3 and 3.4. The survey scan (Figure 3.3) shows no unexpected peaks. Standard values are included in Figure 3.3⁷¹. The peaks from Au and Cl are due to the sample preparation for XPS (§2.1). The intensity of the Au peaks is a function of the thickness of the sample, and inconsequential. The C(1s) peak is found at 286.3 eV, the expected value for adventitious C, and does not shift over time, confirming that the sample is not charging.

The high resolution scan for N(1s) (Figure 3.4.a) confirms that the sample is N-doped. The addition of F causes a reduction in the amount of N retained, since the F bonds to the surface of the TiO₂ particles, preventing the bonding of the amines to the particle surface, and thus more were lost in the wash stage. This mirrors the observation in the FTIR (Figure 3.2) , which also

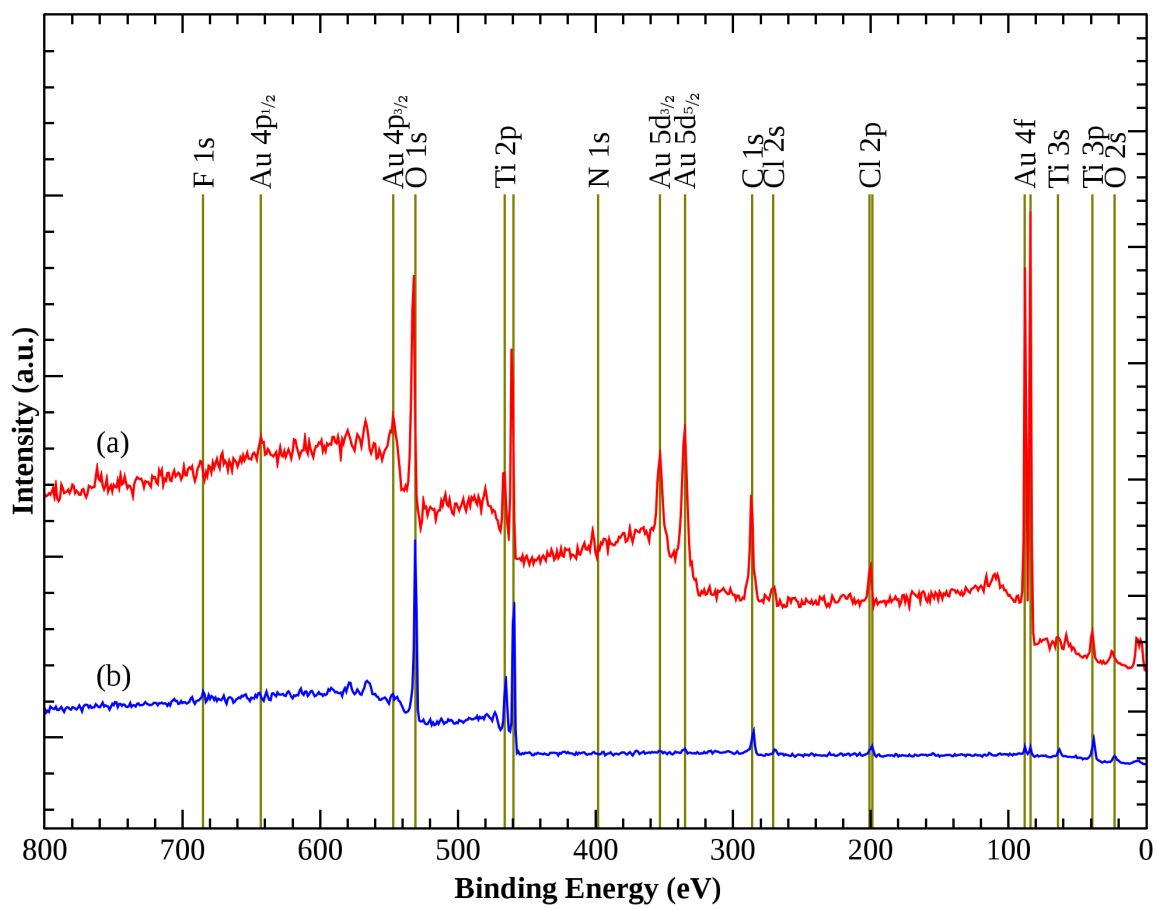


Figure 3.3: XPS survey scan of samples made with organic precursors. (a) N-doped, (b) N,F-doped. Peak assignments from [71].

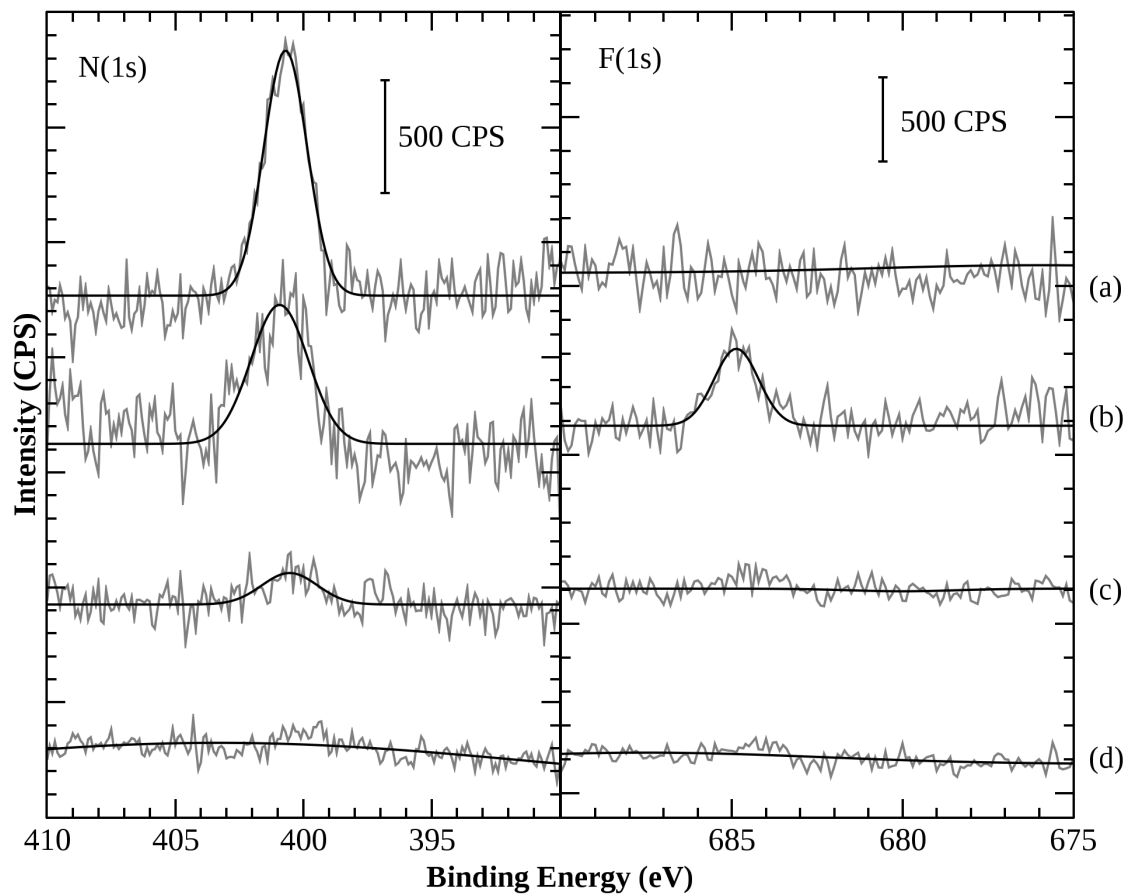


Figure 3.4: High resolution XPS of N(1s) and F(1s) for the TEA sample. (a) shows the N-doped TiO₂, (b) N,F-doped TiO₂, (c) N-doped TiO₂ after annealing at 300 °C, (d) F,N-doped TiO₂ after annealing at 300 °C

shows a reduction in the amount of organic moieties with fluorination.

Annealing the samples to 300 °C causes the N to disappear. This and the fact that fluorination reduces the N amount implies that most of the N seen in both the N- and N,F-doped samples is due to incorporated TEA, not true N-doping. The binding energy of the N(1s) peak at 400.6 eV is consistent with organic amines⁷¹.

The F(1s) high resolution scan is shown in Figure 3.4 confirms the presence of F in the N,F-doped sample. However, upon annealing the F signal disappears.

3.3 Inorganic Precursors (NH₄Cl)

This synthesis was done with an inorganic N source and an inorganic acid. Samples from this synthesis are hereafter referred as NH₄Cl, in reference to the N source.

3.3.1 Synthesis

The same reaction setup was used as described before. A titanium precursor solution was made by mixing 15 mL of TTIP with 10 mL of IPA and placed in the addition funnel. In the three neck flask 100 mL of purified water was mixed with 0.2 mL of 1.0 M hydrochloric acid (HCl) (Aldrich) to bring the pH to 2.0. The titanium precursor solution was added dropwise (~1 drop / 2 sec) under vigorous stirring. During the addition, the exothermic reaction caused a temperature increase of about 6 °C. This produced a milky solution, which was then centrifuged at 3,000 RPM (1,500 G) for 10 minutes, the supernatant discarded, and the centrifuge tubes refilled with purified water and the solid product resuspended. This was repeated 5 times to remove the IPA (added and the reaction product of the hydrolysis of the TTIP) and the HCl. A freeze drying method was employed to remove the water. The wet powder was frozen with liquid nitrogen and placed in a vacuum chamber (base pressure of 10⁻² Torr) at room temperature until the system

recovered its base pressure, indicating all the water was sublimed. It is worthwhile to note that the freeze drying process produces powder with 11 times the volume than any other drying methods we tried (for the same reason freeze dried ice cream looks a lot different than ice cream left to dry on a counter top). No examples of this method were found in the literature. The resulting powder is white in color and is referred to as “pure TiO₂” below. XPS (not shown) shows no unexpected peaks.

TGA measurements, shown in Figure 3.5, only show a peak for free and chemisorbed water at ~60 and 120 °C. In contrast, the organic synthesis shows an additional peak at ~330 °C as the organic impurities mineralize. The sharp drop at approximately 6 minutes for Figure 3.5.b is due to an instrumental failure and can be ignored. This measurement indicates that, compared to the previous sample preparation method, using inorganic precursors provides a much purer final product without the annealing step that is often reported.

3.3.2 Doping

N-doped samples were also prepared by the same method, but with the inclusion of 8 g of NH₄Cl in the water of the titania precursor synthesis (300 mol % N/Ti as per Ref. [89]). The resulting powder is slightly off-white and is referred to as “N-doped”.

The fluorination procedure was adapted from the procedure described by Choi et al⁹⁰. About 300 mg of of as-synthesized powder was suspended in 100 mL of 10 mM NaF and the pH was adjusted with 0.1 M NaOH or HCl. The suspension was vigorously stirred for 24 hours, then washed and dried by the same procedure mentioned above. The amount of free F⁻ ion was monitored with a F⁻ ion selective electrode (ISE). The wash was continued until the wash water reached the detection limit of the F⁻ ISE, about 5 cycles. To further investigate the effect of the

NaF concentration, samples were prepared in a 100 mM NaF solution as well. These samples are termed “surface F-doped TiO₂”.

XPS, shown in Figure 3.6, confirms the presence of N at 5.8 mol percent N/Ti in the N-doped sample. After annealing to 300 °C, the N content drops to 2.9%. The samples treated with NaF also contain 2.5% N. The peak can be deconvoluted to reveal 2 species of N. In contrast to many papers including Asahi et al.¹⁹, no peak near 397 eV is seen. As noted in §1.1.1, this peak is not correlated with the photoactivity of the sample.

The position of the N(1s) peaks in N-doped TiO₂ varies greatly between literature reports, as seen in Figure 3.7, with the majority of reports at about 399 and 402 eV. The peak at 397 eV is universally attributed to a substitutional N because this is the binding energy observed in TiN films. Very few papers that use sol-gel synthesis report a peak near 397 without intensive annealing.

The wide range of reported values is due in part to the wide variety of synthesis methods used and because the majority of published articles do not report how the spectra are normalized, a process which can vary by several eV between groups. Several groups have shown that the adventitious C peak, which is usually used to normalize spectra, can vary between 284.4 and 287 eV depending on the substrate⁹¹⁻⁹³. In fact, the NIST XPS database lists four references for pure NH₄Cl that span 1.2 eV⁹⁴.

However, the correlation between oxidation states of N and the XPS peak position can be determined, and a correlation of about 1.3 eV between oxidation states is measured⁹⁵. This is shown on the top axis of Figure 3.7. This leads to the conclusion that the 402.6 and 401.2 eV peaks seen in this work correspond with N¹⁺ and N⁰, respectively. Both peaks are interstitial N in

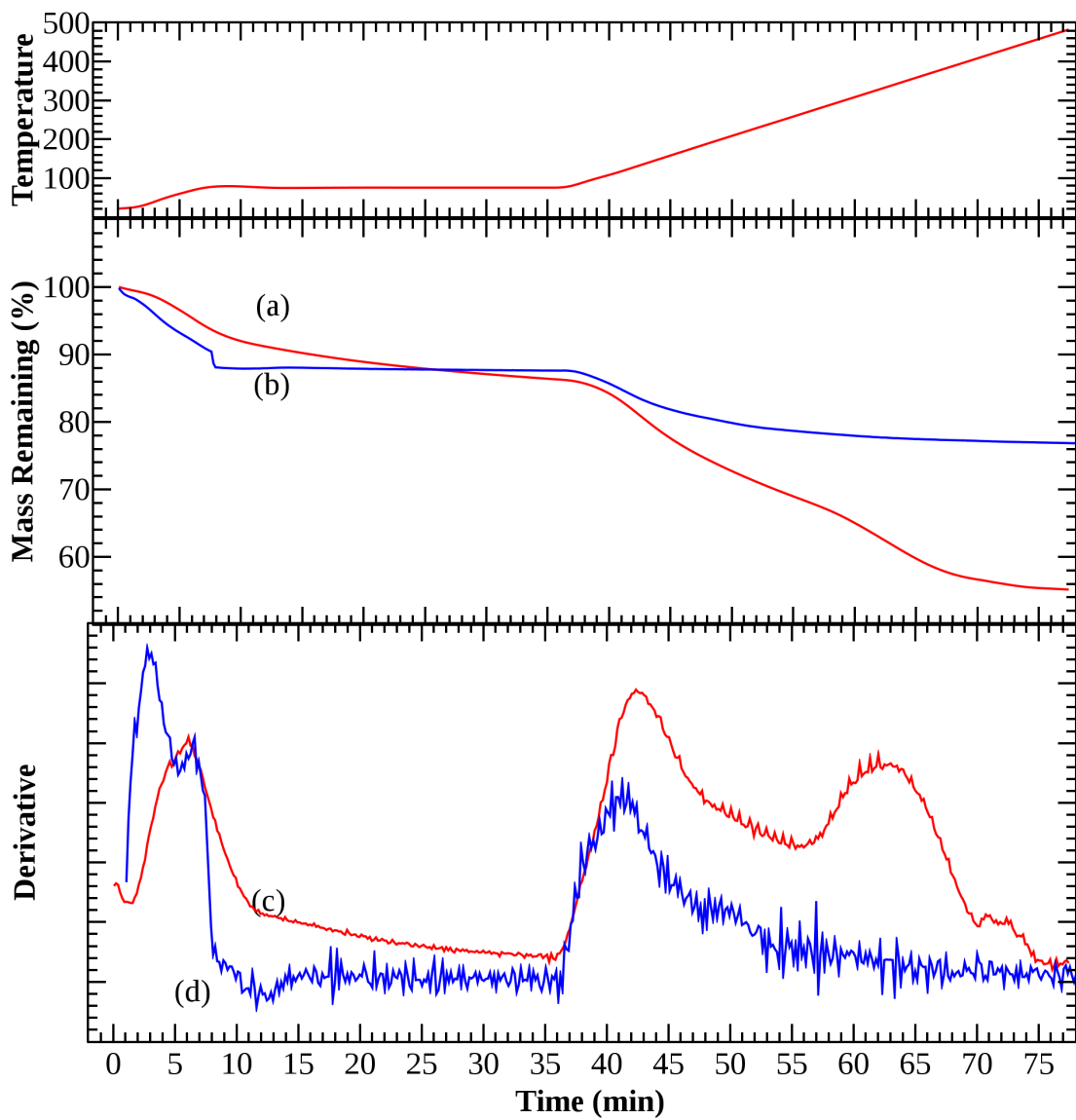


Figure 3.5: TGA analysis of N-doped TiO_2 from (a) TEA and (b) NH_4Cl samples. (c) and (d) show the absolute value of the derivative of (a) and (b), respectively. Note the 30-minute isotherm from time=10 min.

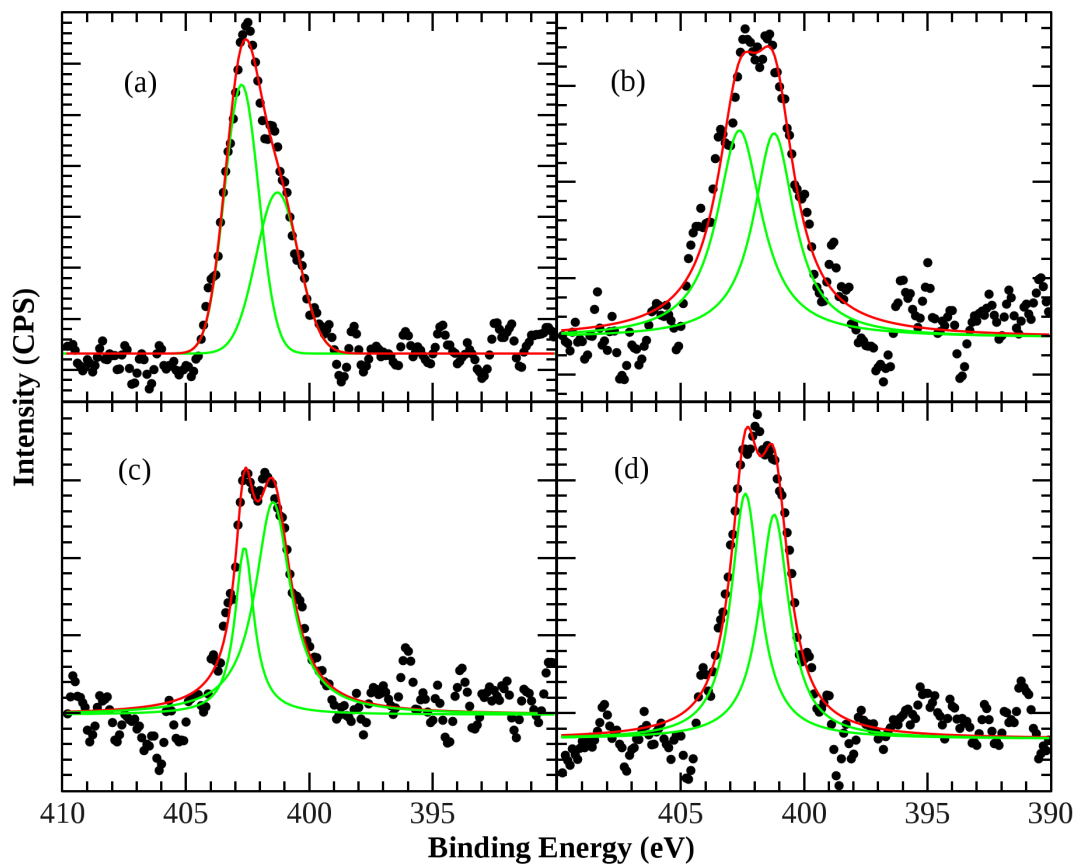


Figure 3.6: High resolution XPS of the N(1s) region of N-doped NH_4Cl samples (a) shows the as made samples, (b) annealed to 300 °C, (c) treated with 10 mM NaF, and (d) treated with 100 mM NaF.

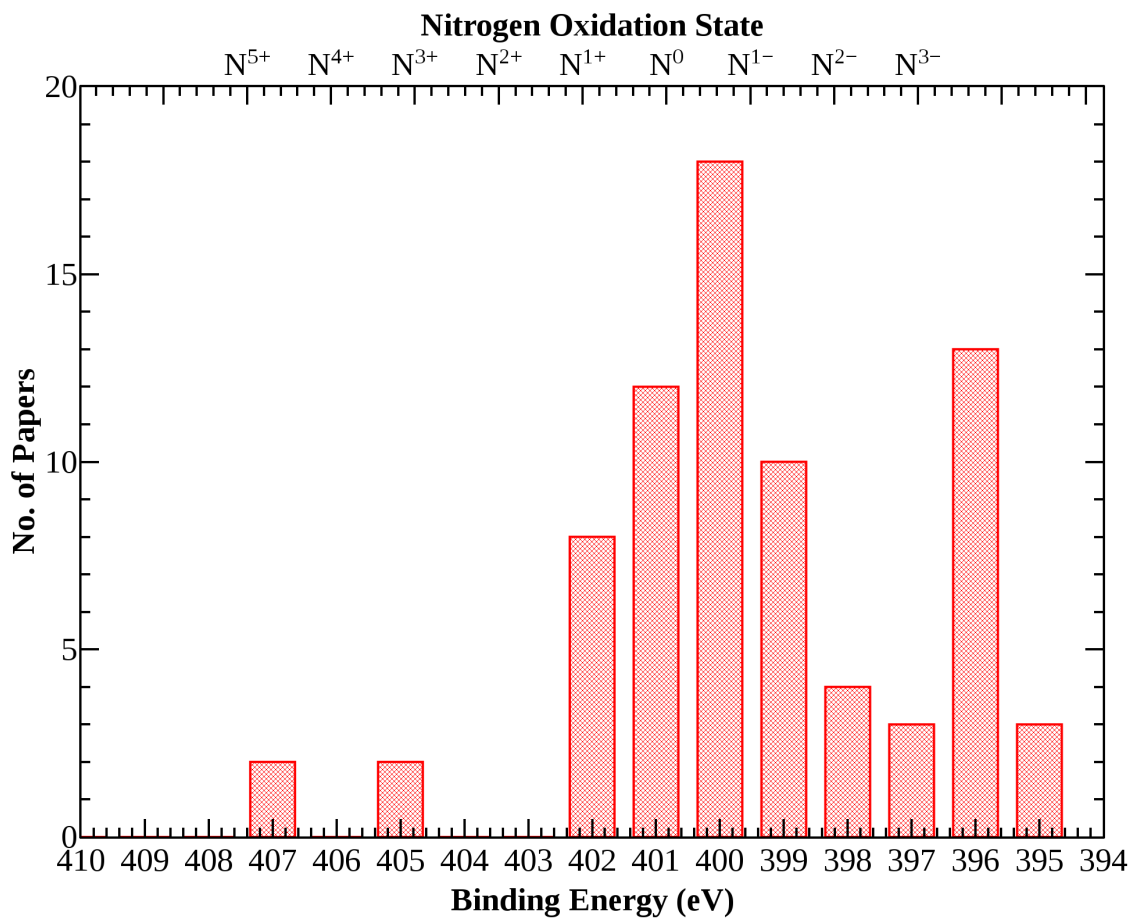


Figure 3.7: Comparison of N(1s) binding energies from published literature. Compiled from [25,26,97–124].

the TiO₂ lattice. Similar peaks have been noted as photoactive in other publications that utilize a sol-gel process and an ammonium salt^{54,96}.

The N(1s) peak in NH₄Cl is known at 400.3 eV¹²⁵, and is not seen in the XPS. Additionally, the Cl peak is absent when the sample is mounted using C tape. This shows that any excess precursors were washed out.

XPS also reveals that samples also retain a large amount of F. As shown in Figure 3.8, neither the concentration of the fluorination treatment or the reaction time affects the amount of F retained, indicating that the F remains on the surface and is not integrating into the particles. Additionally, a binding energy of 685.3 eV is indicative of a surface Ti-F¹²⁶, while a binding energy of 688.6 eV would indicate F-doped TiO₂¹²⁷. The average binding energy is 685.2±0.2, indicating surface F, and a symmetrical peak shape indicates only one species is present. The amount of N retained is also unaffected by the concentration of the fluorination solution.

Since these samples were made without organic precursors, the FTIR spectrum shown in Figure 3.9 shows no organic impurities, with the exception of bicarbonate groups that are absorbed from atmospheric CO₂ and H₂O¹²⁸. The carboxyl (1,300 – 1,700 cm⁻¹) and H₂O signals (2,500 – 3,500 cm⁻¹) are greatly reduced with the fluorinated sample since the Ti-OH groups on the surface have been replaced with Ti-F. The low energy peaks are due to the Ti-O stretches in the bulk material. The signature peaks for NH_x which would indicate residual NH₄Cl precursor in material would be expected at 3200, 3350, and 3450 cm⁻¹ are not seen¹⁰³.

Sample	N ¹⁺	N ⁰	N/Ti (%)
As Synthesized	402.74 eV	401.29 eV	5.82
Annealed	402.62 eV	401.22 eV	2.92
10 mM NaF	402.62 eV	401.47 eV	2.43
100 mM NaF	402.38 eV	401.21 eV	2.46

Table 3.1: Peak positions of the N(1s) signal in Figure 3.6 and relative amounts of N/Ti.

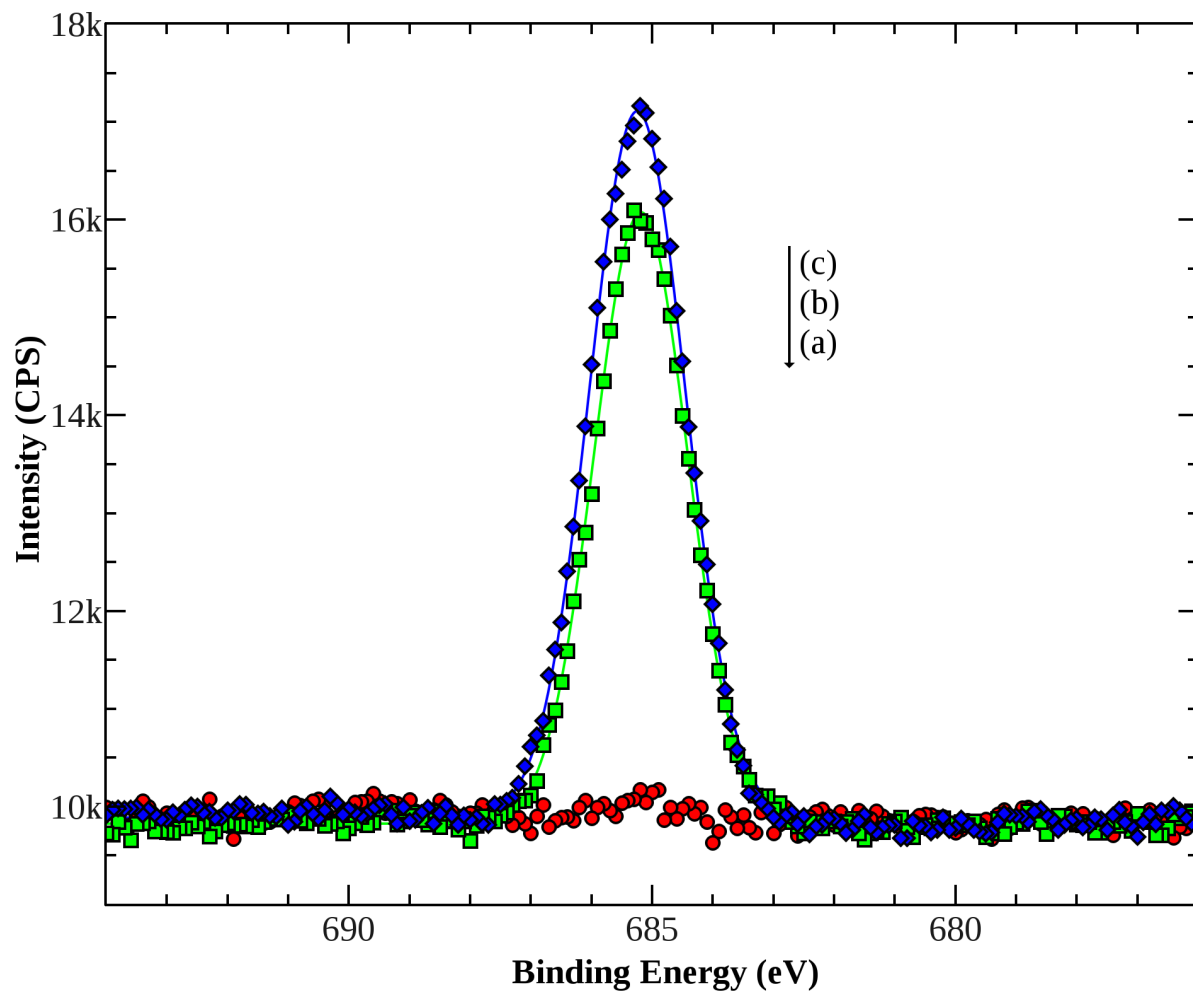


Figure 3.8: High resolution XPS of the F(1s) region of N-doped NH_4Cl samples. (a) shows the as made samples, (b) treated with 10 mM NaF, and (c) treated with 100 mM NaF.

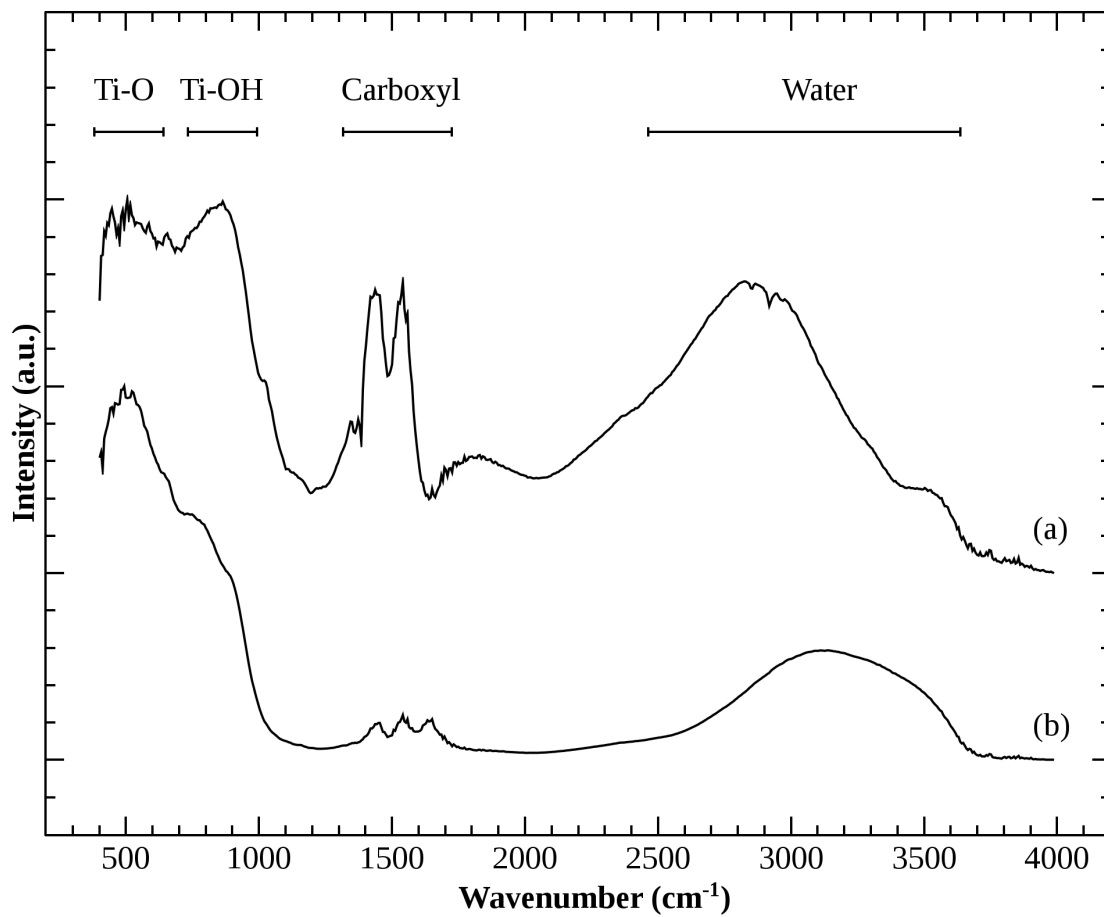


Figure 3.9: DRIFTS measurements of N-doped NH₄Cl sample. (a) shows the as made samples, (b) treated with 100 mM NaF.

3.4 Hydrophilicity

All the samples that were dried in the vacuum chamber gained mass when they were removed. This is due to the vacuum causing the surface chemisorbed water to be pumped off. When the powder is removed from the vacuum and placed on the balance, we can see the mass steadily increase for several hours as atmospheric water is adsorbed. The opposite effect can be seen in the TGA in Figure 3.5.

The hydrophilicity of TiO_2 is well known and is exploited in commercial anti-fog coatings for glass, since fogging is induced on normal glass by the formation of tiny droplets due to the hydrophobicity of SiO_2 . A thin coat of TiO_2 causes the water droplets to spread thinly in a transparent film.

3.5 Annealing

Literature reports for sol-gel syntheses almost always include an annealing in air or O_2 in order to “burn off” the organic residues from the synthesis. The retention of the dopants was investigated by XPS. As expected, annealing caused the loss of N dopant at temperatures greater than 300 °C (shown in Figure 3.10). Surprisingly, the F begins to leave the surface at the relatively low temperature of 200 °C. After annealing to 400 °C, only 15% of the initial F remains.

Annealed samples for photodegradation experiments were prepared by annealing in a tube furnace for 6 hours at 300 °C. The annealing temperature was chosen due to literature reports and our own work that shows N leaving the lattice at temperatures greater than 300 °C.

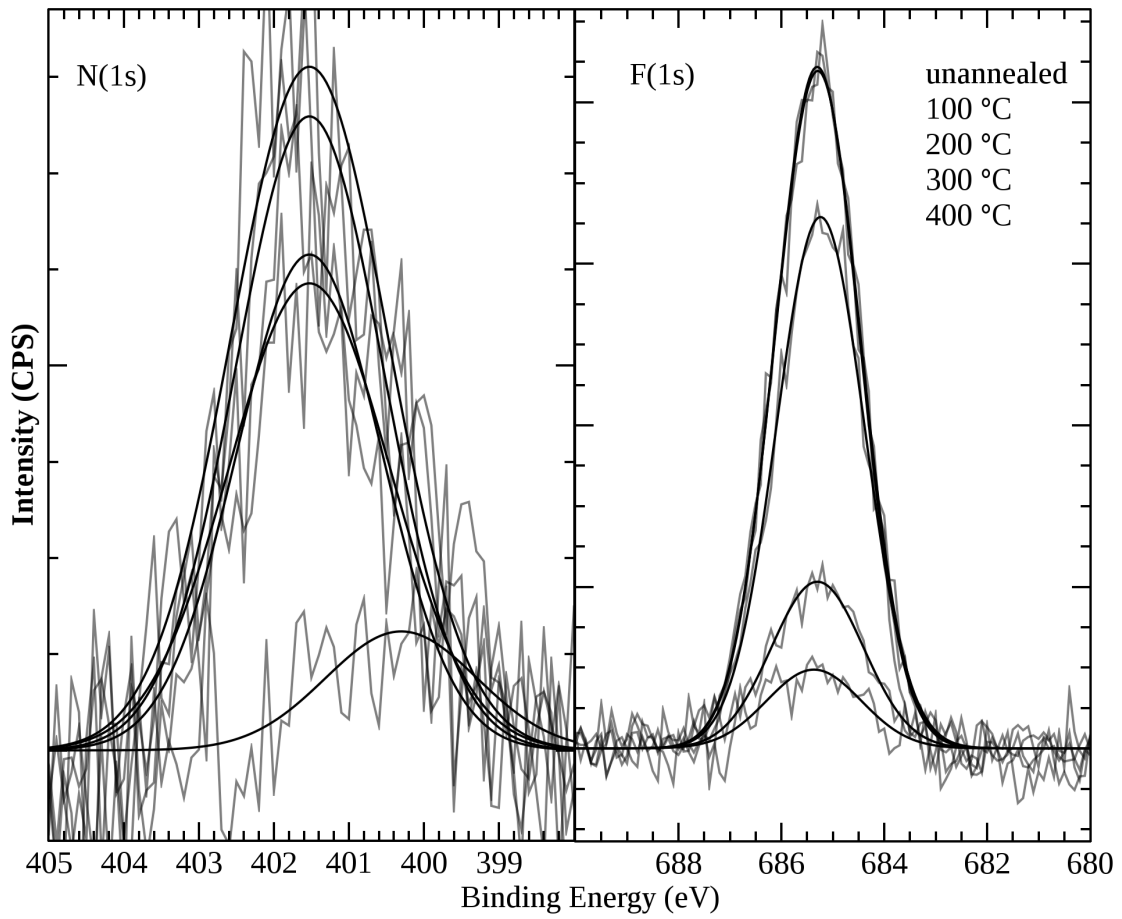


Figure 3.10: Effect of annealing on the retention of dopants for NH_4Cl samples.

3.6 Standards

As with much of the published literature, we used Degussa P-25 Aeroxide (referred to simply as P-25) as a comparison standard. P-25 is made by the flame pyrolysis of TiCl_4 , and is 26% rutile, 74% anatase, has a surface area of $48 \text{ m}^2/\text{g}$ ⁸⁶, and a PZC value of 4.8-6.0⁸⁵.

3.7 Conclusions

N-doped, surface fluorinated, high surface area TiO_2 was successfully synthesized.

Two room-temperature sol-gel processes were developed to create N-doped TiO_2 with high surface area, using organic and inorganic precursors, respectively. The samples made with organic precursors are shown to have a large amount of organic impurities remaining. These can be partially “burned out” by annealing, which also drives out dopants. Additionally, this can cause C-doping, which has been reported beneficial to the photoactivity¹²⁹ but is not the focus of this work. The N-doped samples made with the inorganic precursors were found to be free of the organic impurities and were able to better retain the N dopant when annealed.

Freeze-drying the samples was found preserve the high surface area of the gel, as opposed to traditional drying methods that collapsed the gel as the liquid is extracted.

The surface of the particles was fluorinated after post-synthesis. The TEA had NaF added before the addition of TEA, and the NH_4Cl sample was dried before being re-suspended in a NaF solution. The F is shown to be covalently attached to the surface and displace the -OH groups on pristine TiO_2 . No evidence of bulk-like F incorporation (multicoordinate F, or F-doping) is seen in either method, as this would be evidenced by an extra XPS peak⁹⁶.

The procedures described here are the result of dozens of trials over several years. It is worthwhile to note that many samples were made with a NH_4Cl precursor and showed a bandgap shift, but XPS showed no N present. Deconvolution of the DRS spectra revealed a peak at 440 nm, which is consistent with the formation of O vacancies (V_O) created in the drying process¹³⁰. It was found that stirring the gel in the reaction vessel for more than 12 hours is critical to N incorporation.

CHAPTER 4 - CRYSTALLINITY

4.1 Annealing

A sol-gel synthesis method will produce an amorphous product as shown in Figure 4.1.a. In order to induce crystallinity, the TiO_2 is annealed. Upon annealing to 300 °C, the TiO_2 showed partial conversion to anatase, as shown in Figure 4.1.b. The peaks were compared to standard values³⁷ to confirm that no traces of other TiO_2 polymorphs were present. The broad reflections in the unannealed data are due to the sample holder. Annealing at higher temperatures will cause the anatase to convert to rutile.

4.2 Effect of Fluorination

When the as-synthesized samples are subjected to the surface fluorination procedure at an acidic pH, a clear change is seen in the XRD (as shown in Figure 4.2) showing the formation of the anatase polymorph. It has been shown previously that metal ions affect the crystallization temperatures of TiO_2 ⁵⁰.

As shown in Figure 4.2.a, the as-synthesized sample shows no crystallinity. Annealing the samples induces anatase character (Figure 4.2.b), as expected. After treating the as-synthesized material in a solution of NaF at a pH below the PZC of the material, peaks corresponding to anatase TiO_2 are observed (Figure 4.2.c). With increasing NaF concentration the intensity of the anatase peaks increases (Figure 4.2.d). The full width at half max (FWHM) for Figure 4.2.c&d

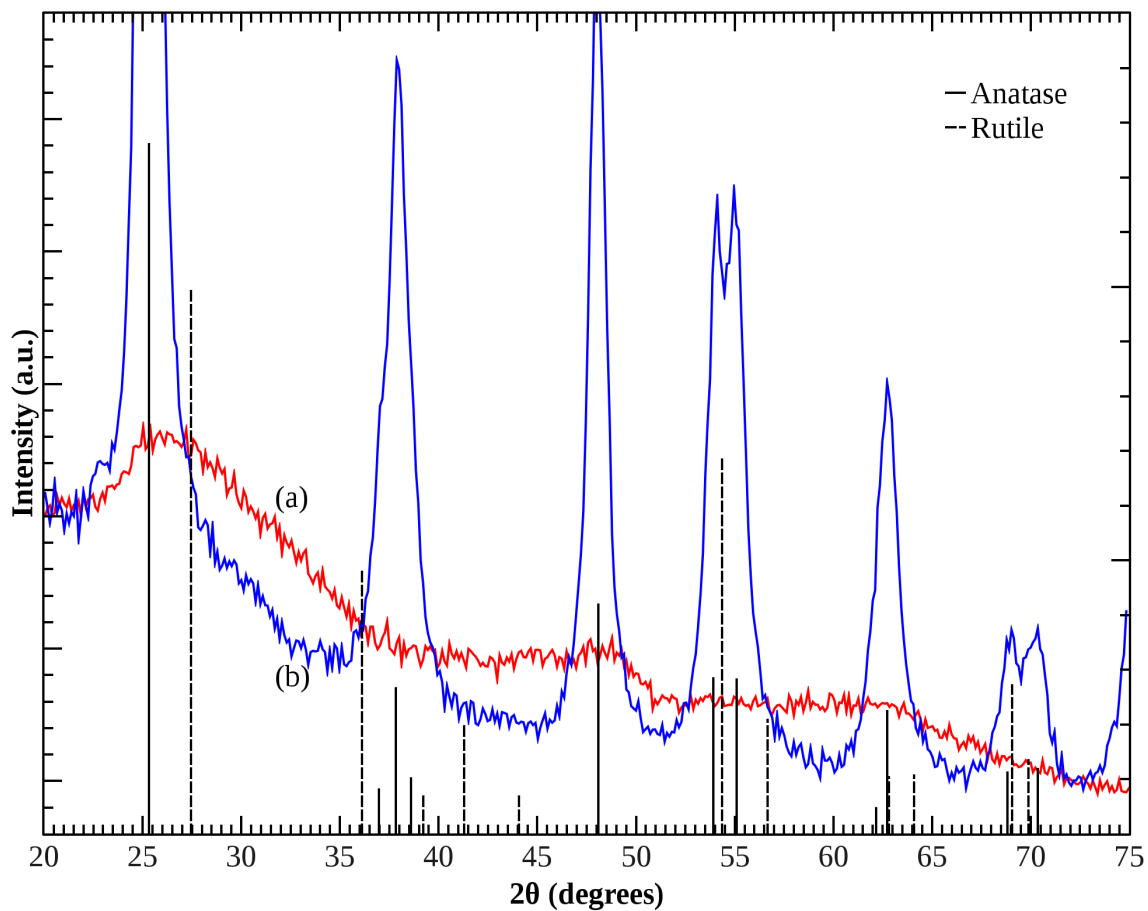


Figure 4.1: XRD spectra show (a) as made TiO_2 samples and (b) annealed to 300 °C. The standard peak positions and intensities for anatase and rutile are shown.

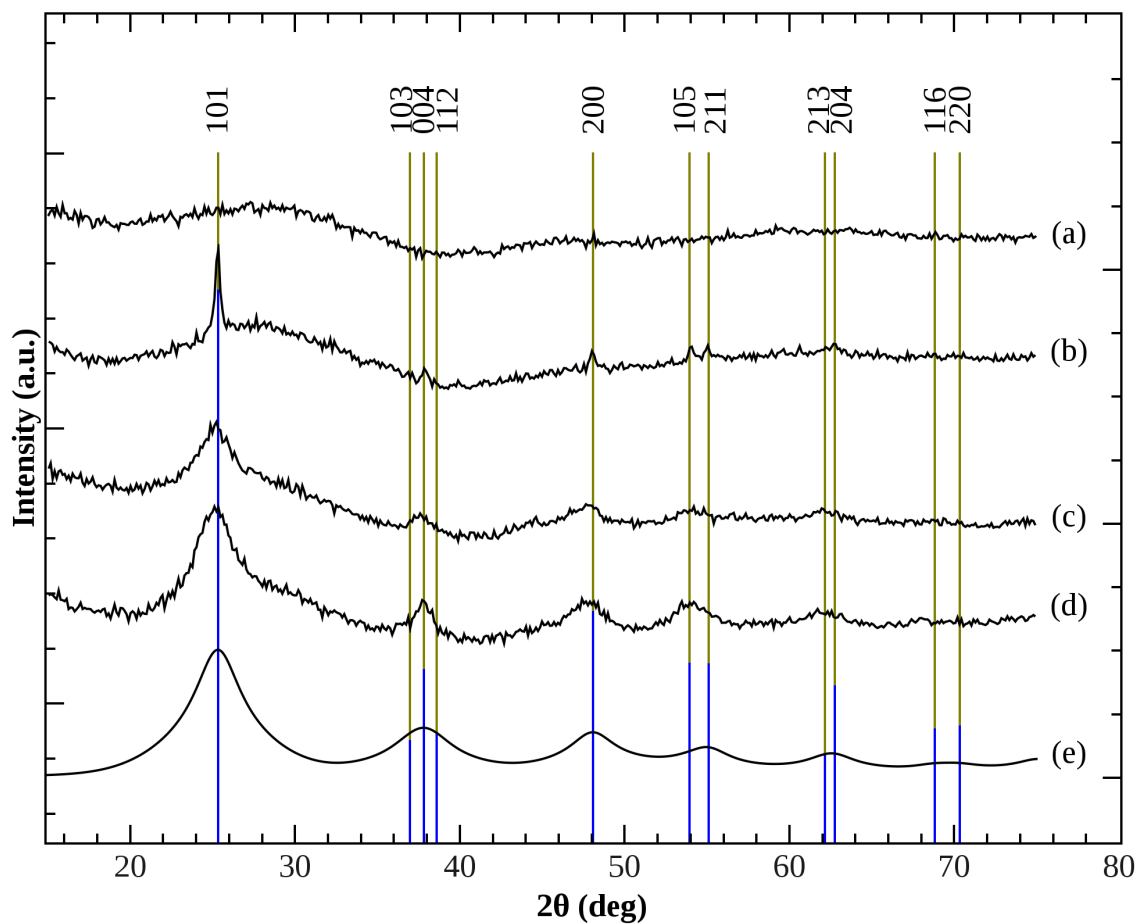


Figure 4.2: XRD spectra of N-doped TiO_2 showing the growth of anatase. (a) shows N-doped TiO_2 as synthesized, (b) after annealing to $300\text{ }^\circ\text{C}$ for 6 hours, (c) after fluorinating in 10 mM NaF, (d) after fluorinating in 100 mM NaF. (e) shows the calculated spectra of pure anatase assuming a crystallite size of 4 nm. The standard anatase powder positions and intensities are noted³⁷.

reveal a crystallite size of 4 nm, and are the same, indicating that the crystallite size is the same, but the increased intensity indicates that the absolute amount has increased. All of these XRD observations are confirmed by Raman measurements, shown in Figure 4.3. Raman is more sensitive to smaller crystallites, and Figure 4.3.a confirms that there is no crystallites in the as-synthesized samples. The Raman modes for anatase are indicated in the figure¹³¹. For Raman, the peak position is dependent on crystallite size¹³². Since the most intense E_g peak for both concentrations of NaF (Figure 4.3.b & c) are at 158 cm^{-1} , it is confirmed that the crystallites are not growing, but the peak intensity increase indicates that the absolute amount of crystallites is increasing. All of the peaks observed in XRD and Raman can be matched to anatase phase in position and relative intensity, with no trace of signals from any other polymorph of TiO_2 or any signal from TiN, TiOF_2 , or other possible crystal forms. Figure 4.2.e shows the simulated structure of anatase based on standard positions and peak intensities³⁷ and the observed FWHM.

This change also causes a change in the optical properties of the sample, as anatase has a lower bandgap than amorphous TiO_2 . The N-doped sample shown in Figure 4.4.a has a bandgap of 386 nm (3.21 eV). When treated with an acidic NaF solution, the bandgap decreases to 395 nm (3.14 eV), shown in Figure 4.4.b, due to the anatase formed. A sample treated with surface F but without allowing the anatase formation (shown in Figure 4.4.c) does not show this decrease, indicating that that anatase formation is responsible for the bandgap decrease. The slight increase in the bandgap is due to the reduction of N-doping as a result of the fluorination process, as shown with XPS (Table 3.1).

Room-temperature anatase formation has very recently been reported with a synthesis technique using formamide ($\text{H}_2\text{N-CHO}$) instead of NaF ¹³³ during the synthesis. The results are

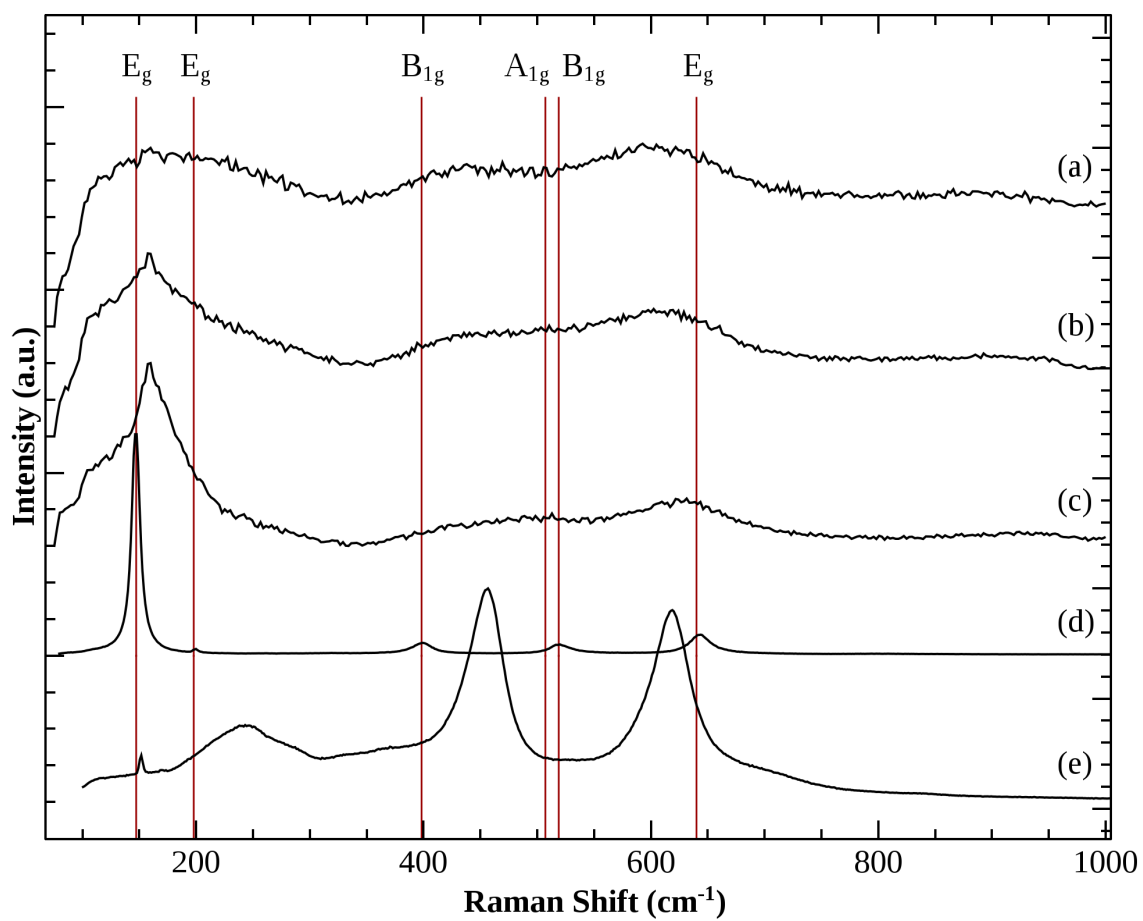


Figure 4.3: Raman spectra of surface F-doped TiO₂. (a) shows as synthesized TiO₂, (b) fluorinated in 10 mM NaF solution, (c) fluorination in 100 mM NaF solution, (d) standard anatase, and (e) standard rutile. The raman modes for anatase are noted¹³¹.

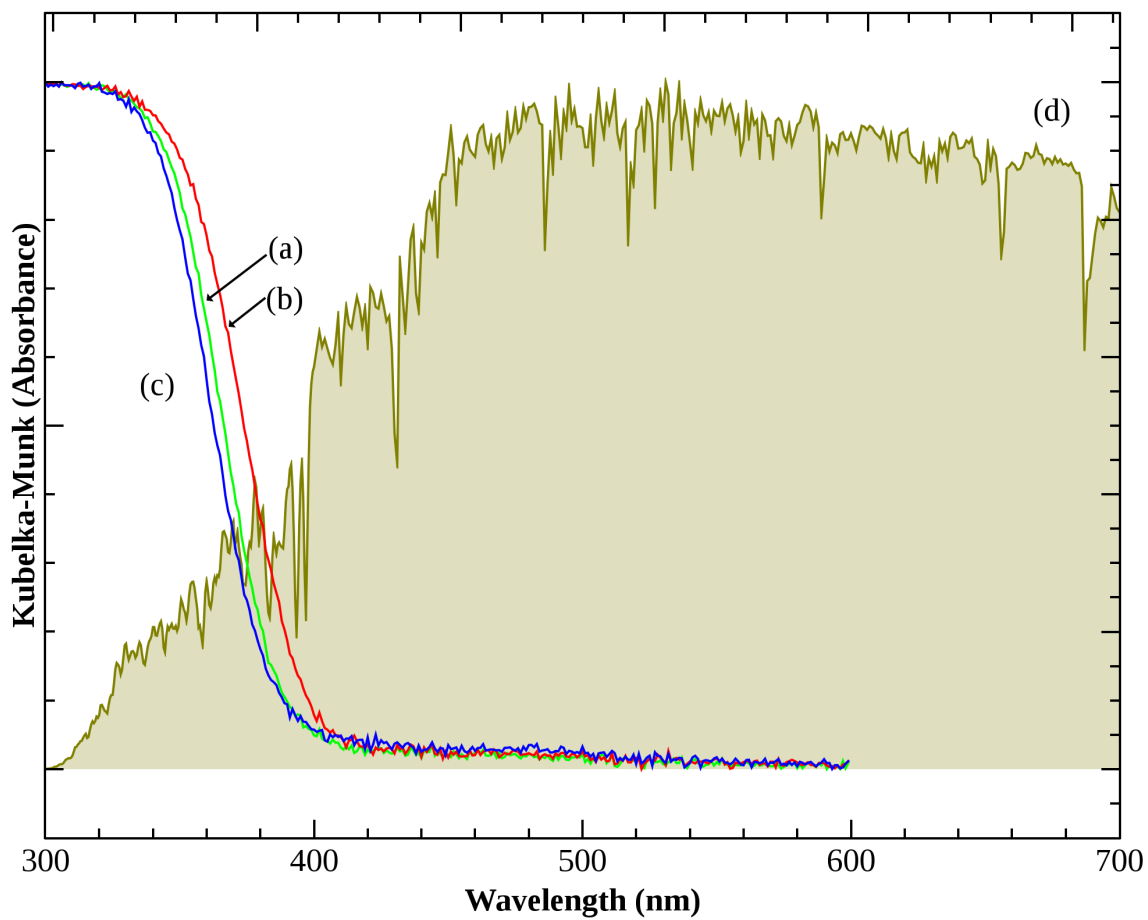
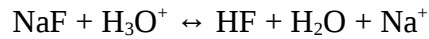


Figure 4.4: DRS of NH_4Cl samples. (a) N-doped TiO_2 , (b) fluorinated anatase N-doped TiO_2 , (c) fluorinated amorphous N-doped TiO_2 . (d) shows the AM1.5 solar spectrum.

very similar to the ones reported here, however, require the use of formamide, which is toxic, teratogenic, corrosive, and decomposes to hydrogen cyanide upon heating.

4.2.1 Proposed Mechanism of Anatase Formation

Introducing the samples to an acidic NaF solution causes the formation of HF, which continues in the dissolution / redeposition of the TiO₂ by the following reaction¹³⁴:



If the solution pH is below the PZC of the particles, then the surface of the particles will have a net positive charge. This will cause a coulombic attraction between the particles and the TiF₆²⁻, causing the redeposition of TiO₂ as an anatase crystal.



Other researchers have referred to this process as Ostwald ripening^{134,135}, a misnomer as the process does not involve particle growth. Ostwald ripening is a thermodynamically driven process because larger particles are thermodynamically more stable^{136,137}.

Although rutile has a lower Gibbs free energy (see §1.2, page 9), the redeposition occurs as anatase rather than amorphous or another phase of TiO₂ because anatase has the lowest surface energy. Other work has shown similar results with very slow TiO₂ particle growth by extreme dilution of the precursors¹³⁸. The calculated surface energies (using density functional theory (DFT) within the generalized-gradient approximation (GGA), with the exchange-correlation functional of Perdew and Wang (PW91)) from reference [139] are tabulated in Table 4.1.

The energy of formation, G_x^0 , is related to the surface free energy by the equation

Anatase		
Surface	γ (J/m ²)	σ (J/m ²)
(001)	0.84	0.91
(100)	0.65	-0.19
(101)	0.63	0.09

Rutile		
Surface	γ (J/m ²)	σ (J/m ²)
(100)	1.82	0.80
(110)	0.84	1.27
(011)	1.19	1.38

Table 4.1: Surface energies for anatase and rutile from [139].

$$G_x^0 = \Delta_f G_x^0 + \frac{M}{\rho_x} (1-e) \left[q \sum_i f_i \gamma_{xi} \right] \quad (7)$$

where γ is the surface free energy, σ is the surface tension, $\Delta_f G_x^0$ is the free energy of formation for the bulk, M is the molar mass, ρ_x is the density, e is the volume dilution induced by surface tension, q is the surface to volume ratio and f_i is a weighting factor.

It is also worthwhile to note that the 10 mM fluorination process had a 92% recovery while the 100 mM process only had 42% recovery. This is due to the greater concentration of F^- ions, therefore much greater amount of TiF_6^{2-} remains in solution at the end of the reaction, which was then washed out. A quick calculation shows that for the quantities used in this reaction a 10 mM NaF solution can dissolve 5.7% of the Ti to TiF_6^{2-} , while 100 mM NaF will dissolve 40%. Any Ti in the form of TiF_6^{2-} will be washed out at the reaction end.

The pH in the fluorination process was adjusted with HCl and NaOH. The reaction was also successfully run with H_2SO_4 and HNO_3 and it was concluded that the acid source has no effect. XRD shows no differences as a function of the acid source.

4.2.2 Crystallization Kinetics

The anatase crystals appear as a exponential rise with increasing concentrations of NaF. The same effect is observed with increasing reaction time, shown in Figure 4.5.a. The (101) peak can be fit to a Gaussian distribution:

$$f(x) = \frac{A}{w} \cdot \sqrt{\frac{2}{\pi}} \cdot \exp\left(-2 \cdot \left(\frac{x-c}{w}\right)^2\right) \quad (8)$$

By plotting the fit variable A (which determines intensity) for the anatase (101) peak (Figure 4.5.b) it becomes clear that the reaction has reached 90% of saturation after 2 days. This is

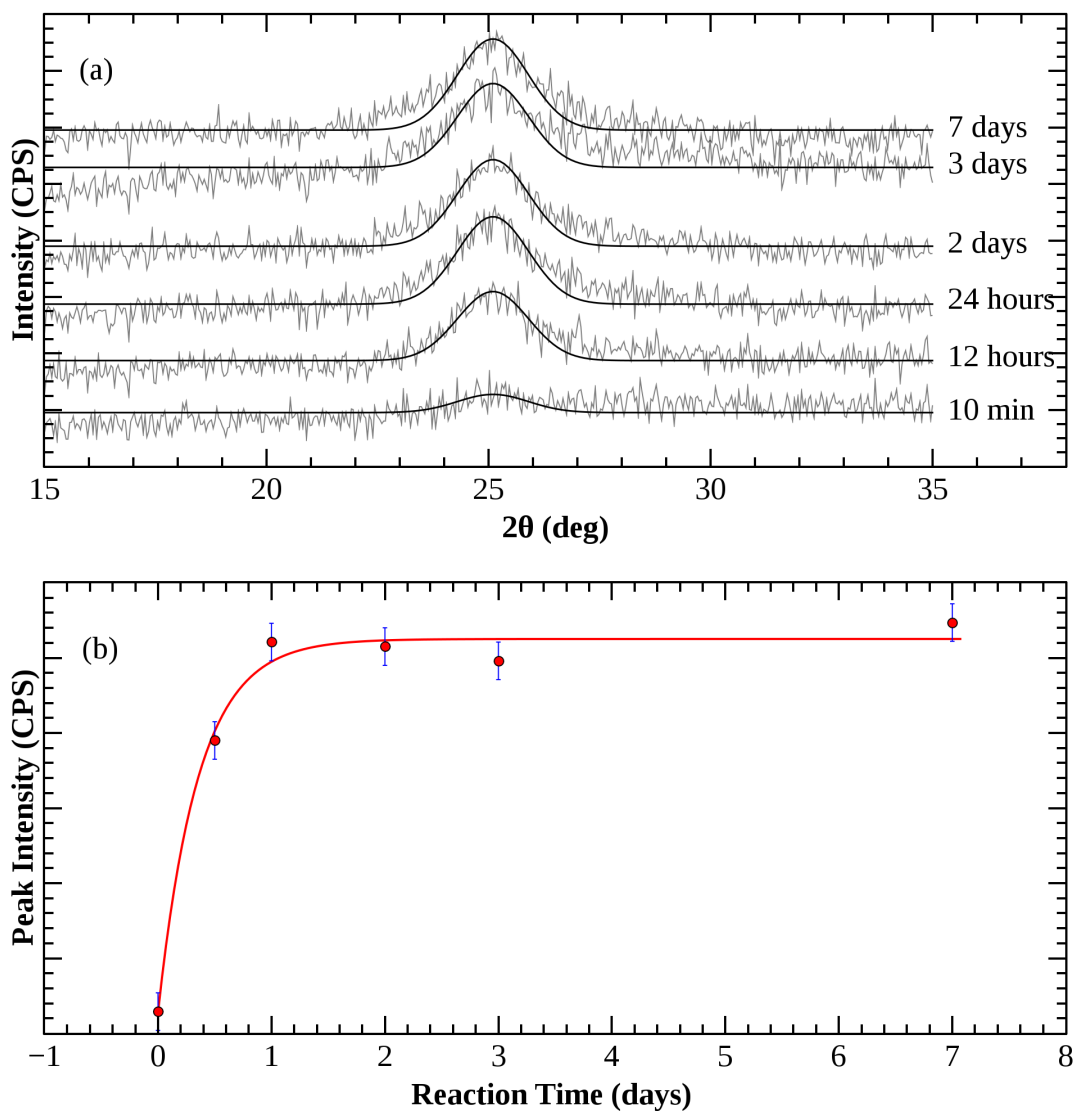


Figure 4.5: Time dependence of the growth of anatase in a 10 mM NaF at pH=3.4. (a) shows the anatase (101) peak after various reaction times. (b) Peak intensities with respect to time.

observed because the Ti dissolution step is not preferential to the amorphous TiO_2 , and as the surface becomes coated with anatase TiO_2 , much of the anatase will redissolve.

All reactions were done under constant slow stirring, although control experiments showed only a slight decrease when no stirring was used.

The kinetics of crystallization were affected by the N-doping of the sample, with the N-doped samples showing a slightly decreased rate of anatase formation, as shown in Figure 4.6. This is an effect of the raised PZC of the N-doped particles, and shows how N-doping alters the surface chemistry. Another example of this effect is seen in §7.1.

4.2.3 pH dependance

The anatase transformation is only evident if the pH of the NaF solution is acidic. The exact point that the transformation takes place is related to the PZC of the material. Figure 4.7 shows the anatase (101) peak for samples fluorinated at various pH's. All samples treated above a pH of 5.58 show no anatase, while all samples treated at a pH of 4.62 and below show a transformation to anatase. For all samples below the pH threshold, the intensity and crystalline size of the anatase (101) peak remain the same. This amount is termed the saturation point. The sample at pH of 5.06 showed a partial transition. The peaks were fit and the (101) intensity extracted in the same manner as described in §4.2.2. These were fit to a sigmoidal curve, shown in Figure 4.8 on the right axis. From the fit, the 1%, 50%, and 99% of saturation could be extracted and found to correspond with a pH of 5.7, 5.0, and 4.4, respectively. This matches very well with the measured PZC for this material at 5.2, shown in Figure 4.9.

It should also be noted that since HF is a necessary component, the amount of free HF in solution may influence the point at which this transformation takes place in instances with a high

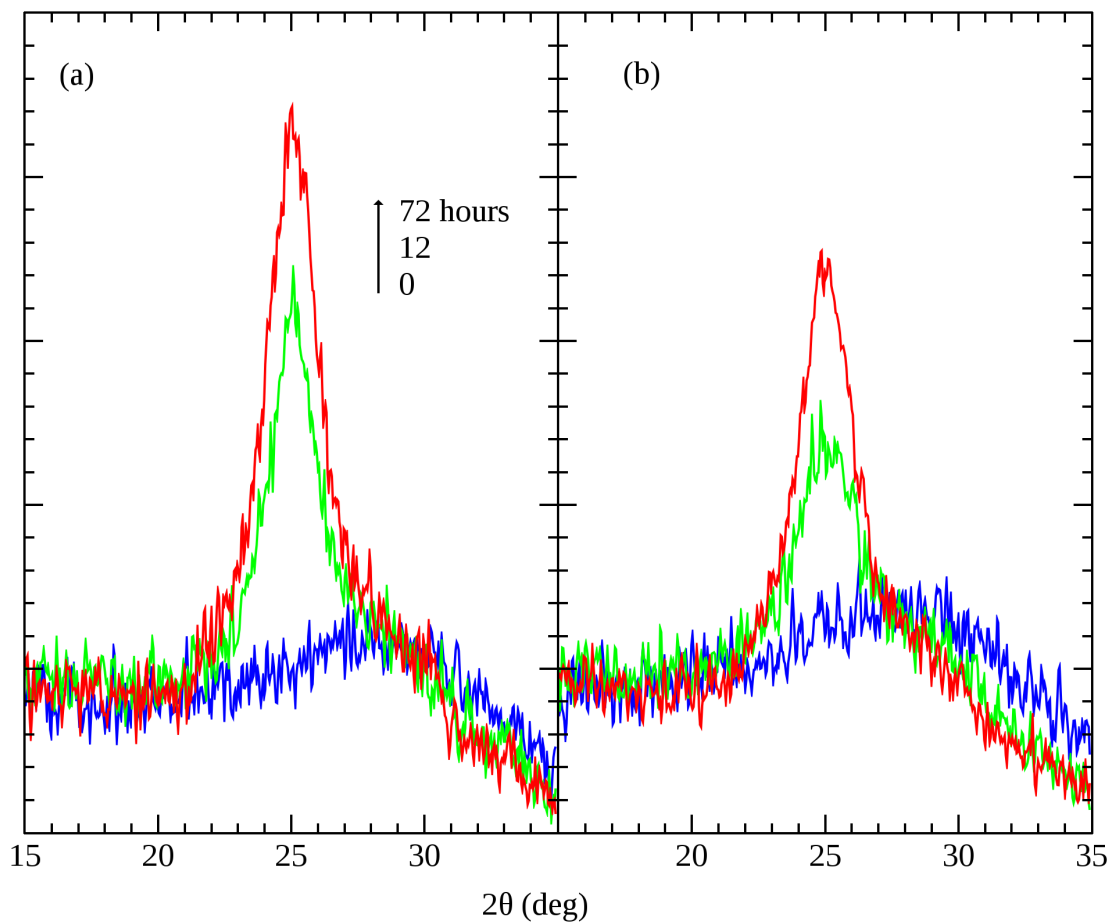


Figure 4.6: XRD spectra to show the influence of N-doping. (a) shows growth over time of anatase (101) peak for undoped TiO_2 , (b) shows N-doped TiO_2 .

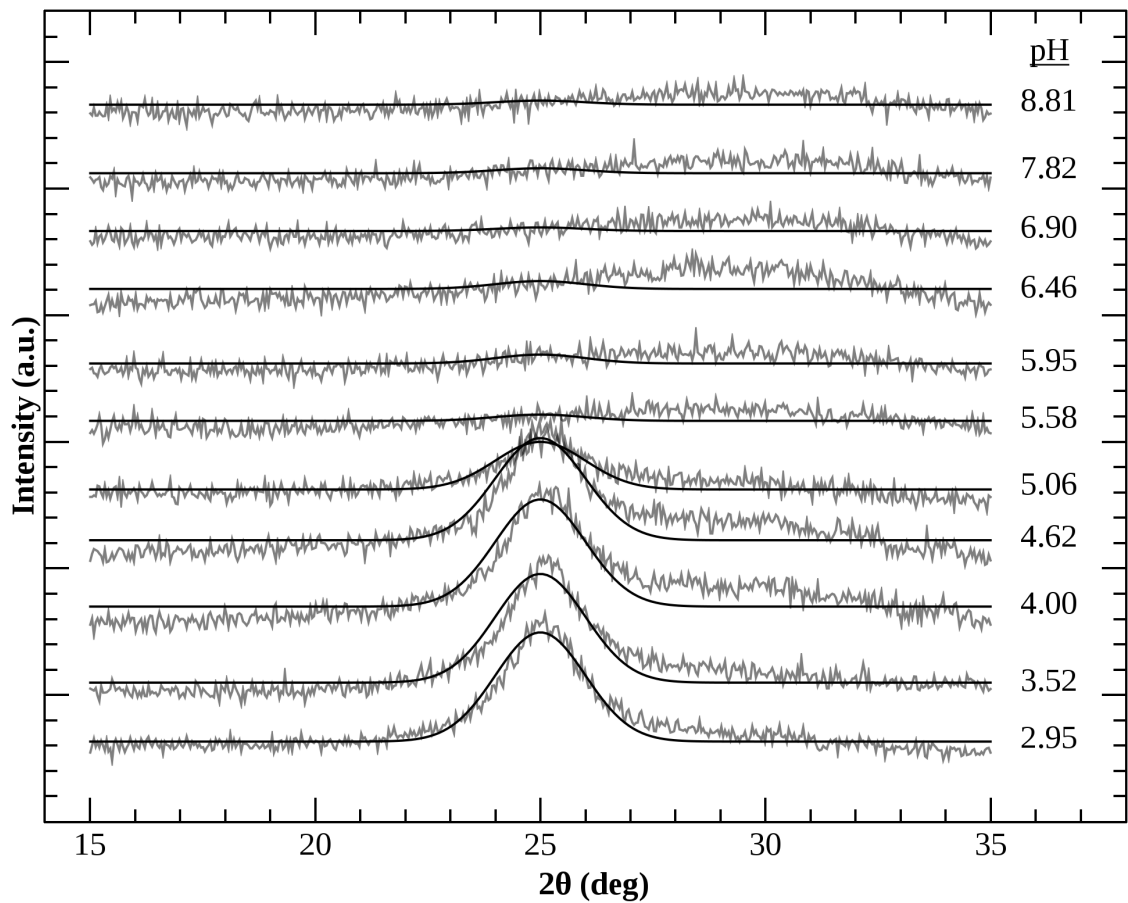


Figure 4.7: XRD spectra of the anatase (101) peak to show the anatase transformation at various pH values for pure TiO₂. The dark line is the fit, with the data shown in gray.

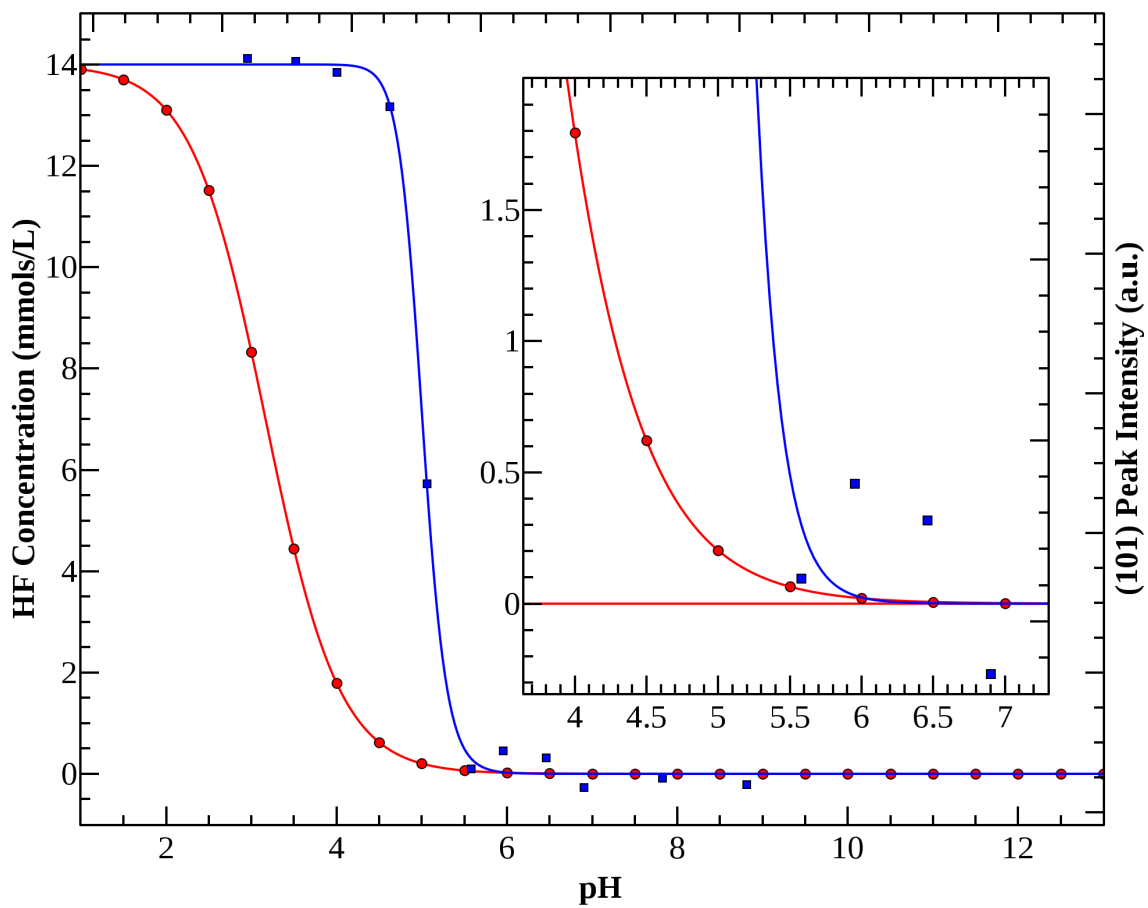


Figure 4.8: Theoretical concentration of HF vs pH based on a pK_a for HF of 3.167 is shown with \bullet . On the right axis, the anatase (101) peak intensity from Figure 4.7 is shown with \blacksquare .

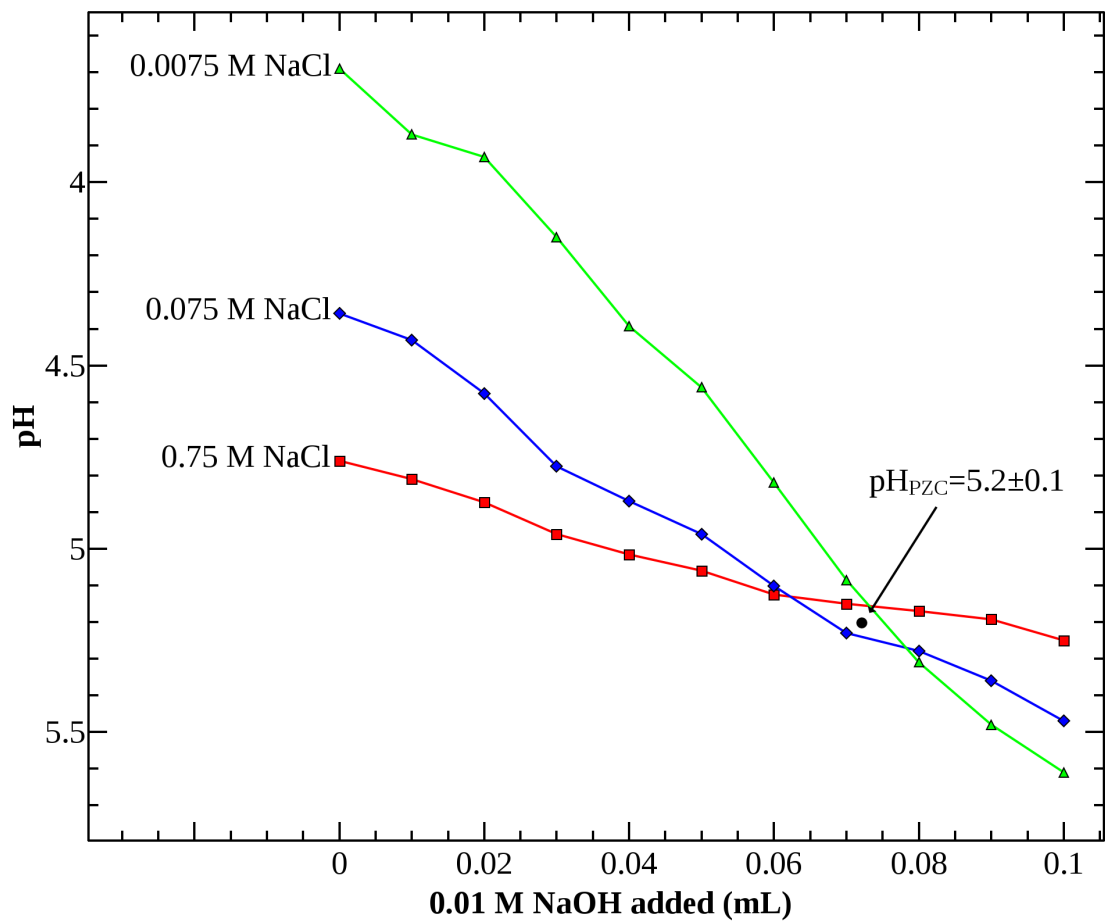


Figure 4.9: Measurement to find the PZC of N-doped NH_4Cl sample.

PZC. Plotting the amount of HF / F⁻ in solution results in Figure 4.8 and Table 4.2, assuming a 14 mM solution of NaF and knowing the pK_a of HF is 3.167. The sigmoidal curves for the anatase transformation and amount of HF do not correlate suggesting that the anatase transformation is at best weakly linked to the amount of HF in solution.

An abrupt absorption edge similar to the anatase transformation curve has been reported before for TiO₂ nanoparticles adsorbing Zn²⁺ and Cd²⁺ ions. This was attributed as a function of the PZC of the particles¹⁴⁰. However, the amount of absorbed F, as calculated from the amount of F⁻ remaining in solution after fluorination with an F⁻ ISE, does not show an abrupt edge, but rather the more expected gradual uptake (shown in Figure 4.10). This is confirmed by XPS and Auger measurements (Figure 4.11). The amount of adsorbed F correlates loosely with the amount of HF in solution, shown in Figure 4.10 as the solid line on the right axis.

This suggests that the threshold point where the anatase transition takes place is a function of both the PZC of the material and the amount of HF in solution.

4.3 Phase Transition Temperature

Fluorination also lowers the amorphous-anatase phase transition temperature (α -A PTT). Figure 4.12.a shows XRD spectra of the as-synthesized particles. As discussed earlier, fluorination causes approximately the same amount of anatase to form as annealing to 300 °C (Figure 4.12.b&c). However, after annealing the fluorinated sample the amount of anatase increases 12 – 42 fold (Figure 4.12.d). Fluorinating the annealed particles (Figure 4.12.e) causes no discernible change. This experiment was performed in triplicate.

pH	[HF] (mmols/L)	[HF]/[F ⁻] (%)	(101) Peak Intensity (CPS)
1.5	13.7	4650%	--
2.0	13.1	1470%	--
2.5	11.5	464%	--
3.0	8.32	146%	1080
3.5	4.44	46.5%	1076
4.0	1.79	14.7%	1060
4.5	0.621	4.65%	1011
5.0	0.202	1.47%	471
5.5	0.0647	0.465%	61.9
6.0	0.0205	0.147%	88.1
6.5	6.50×10^{-3}	0.0464%	77.9
7.0	2.05×10^{-3}	0.0147%	35.5
8.0	6.50×10^{-4}	1.46×10^{-3} %	48.8
9.0	2.05×10^{-4}	1.46×10^{-4} %	40.1

Table 4.2: Comparison of the available HF and the amount of anatase formed at a given pH.

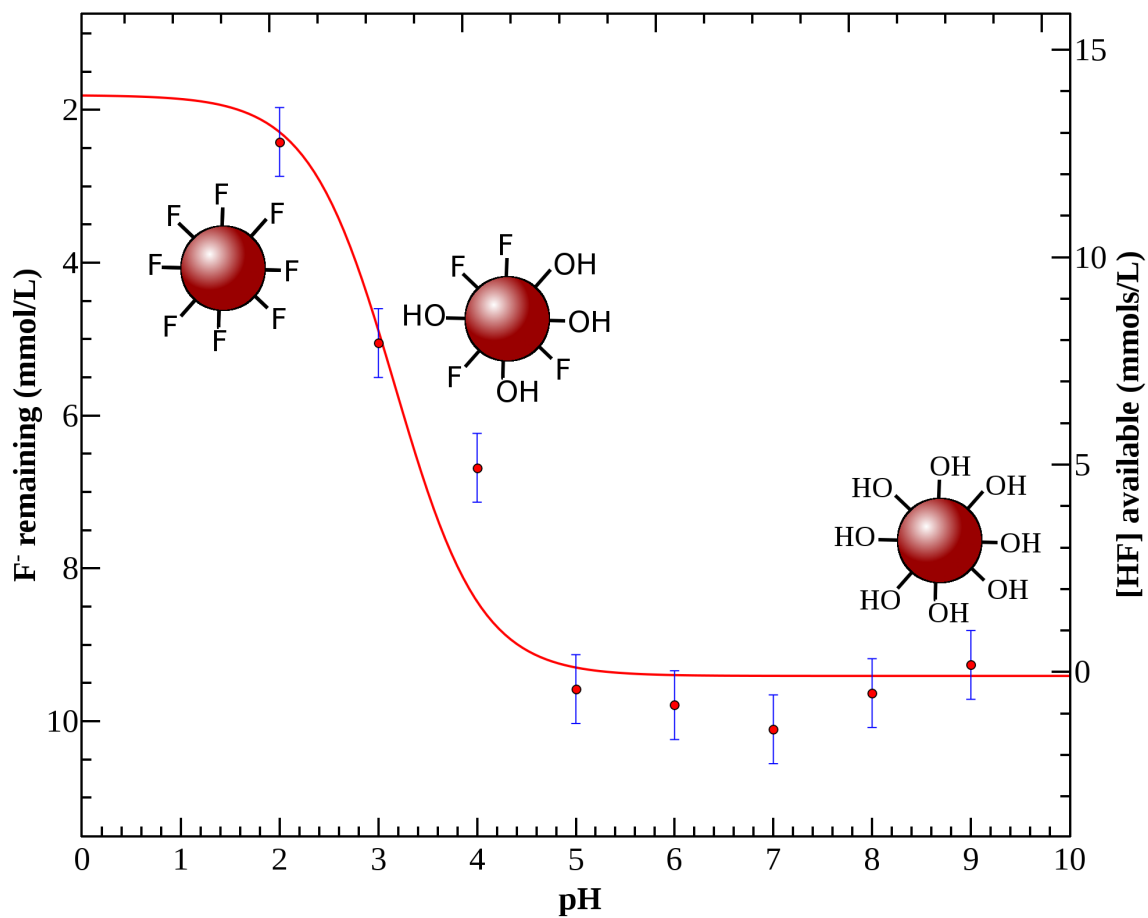


Figure 4.10: The data points are linked to the left axis and show the amount of F⁻ remaining in solution after fluorination vs pH of the fluorination solution. The solid line on the right axis shows the amount of F⁻ vs HF.

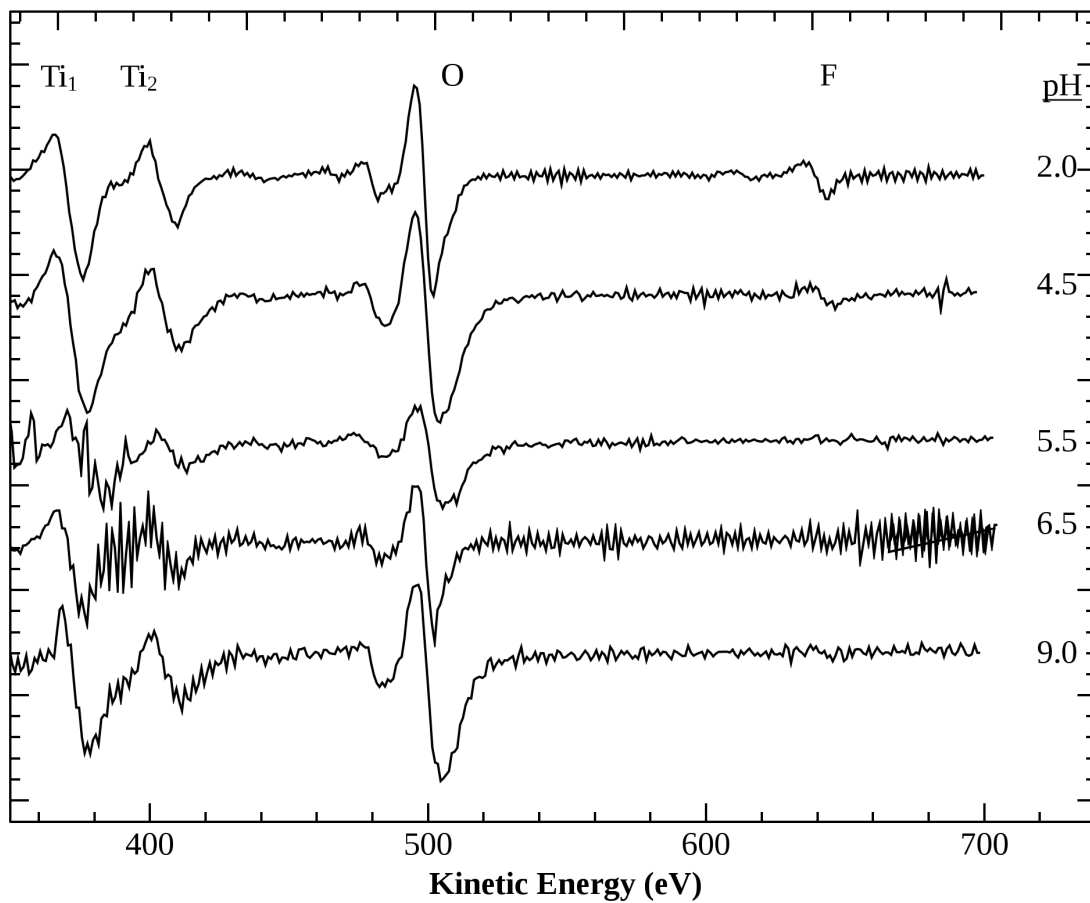


Figure 4.11: AES after treating NH₄Cl samples at various pH values.

This is referred to the amorphous – anatase phase transition temperature (α -A PTT). Fluorination causes a significant lowering of the α -A PTT. This is due to the fluorination process creating “seed” crystals and the F lowering the surface energy. Other experiments show that fluorinated TiO₂ shows an increase in the amount of anatase at temperatures as low as 100 °C, while pure TiO₂ requires temperatures of at least 300 °C to show any crystallinity. Furthermore, TiO₂ fluorinated at a pH above the transition point does not affect the α -A PTT, although XPS confirms there is F on the surface, albeit a fraction of the amount on the TiO₂ fluorinated at a pH below the transition point.

While the effect of dopants on the anatase – rutile PTT (A-R PTT) have been extensively studied, very little effort has been spent on the α -A PTT. To our knowledge the effect of F on the α -A PTT has not been reported before.

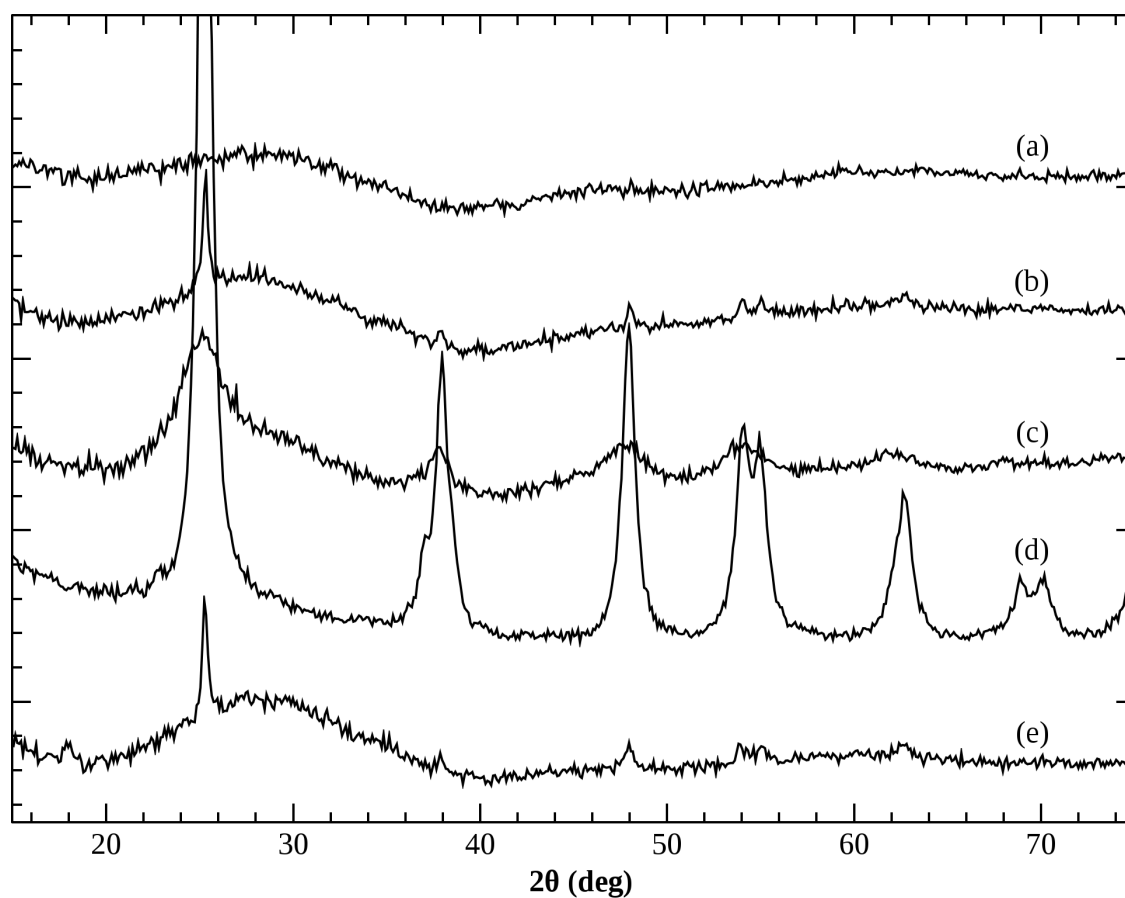


Figure 4.12: XRD spectra to show the effect of F on the PTT. (a) shows as synthesized N-doped TiO_2 , (b) after annealing (a) to 300 °C for 6 hours, (c) after fluorinating (a) in 10 mM NaF, (d) after annealing (c) to 300 °C for 6 hours, (e) after fluorinating (b) in 100 mM NaF.

CHAPTER 5 - PHOTOACTIVITY

5.1 Increasing the Optical Absorption

Since Asahi et al. published results that showed the bandgap lowering with N-doping, many groups have reported the corresponding increase in the optical absorption. This was measured for this work as well using DRS measurements. It should be noted that measuring the absorption is a useful tool, but should not be considered proportional with e^-/h^+ pairs generated.

5.1.1 Powders from Organic Synthesis

The DRS measurements are shown in Figure 5.1. The pure (undoped) sample shows comparable spectra to the standard purchased sample (Degussa P-25), indicating that a material with similar optical properties was successfully synthesized. The N-doped material shows a clear shift in the bandgap and thereby an increase in the absorption amount. The N,F-doped TiO_2 shows very little change from the N-doped, which was expected since the F should have a negligible contribution to the optical properties.

Since many applications for TiO_2 call for the harnessing of sunlight, the solar spectrum¹⁸ is provided in Figure 5.1. The amount of sunlight that can be harnessed by each sample can be estimated mathematically as the intersection of the absorbance and the solar spectrum. For this sample, the N-doped and F,N-doped samples have 166% the absorbance of the pure TiO_2 sample (for the range of 300 – 600 nm).

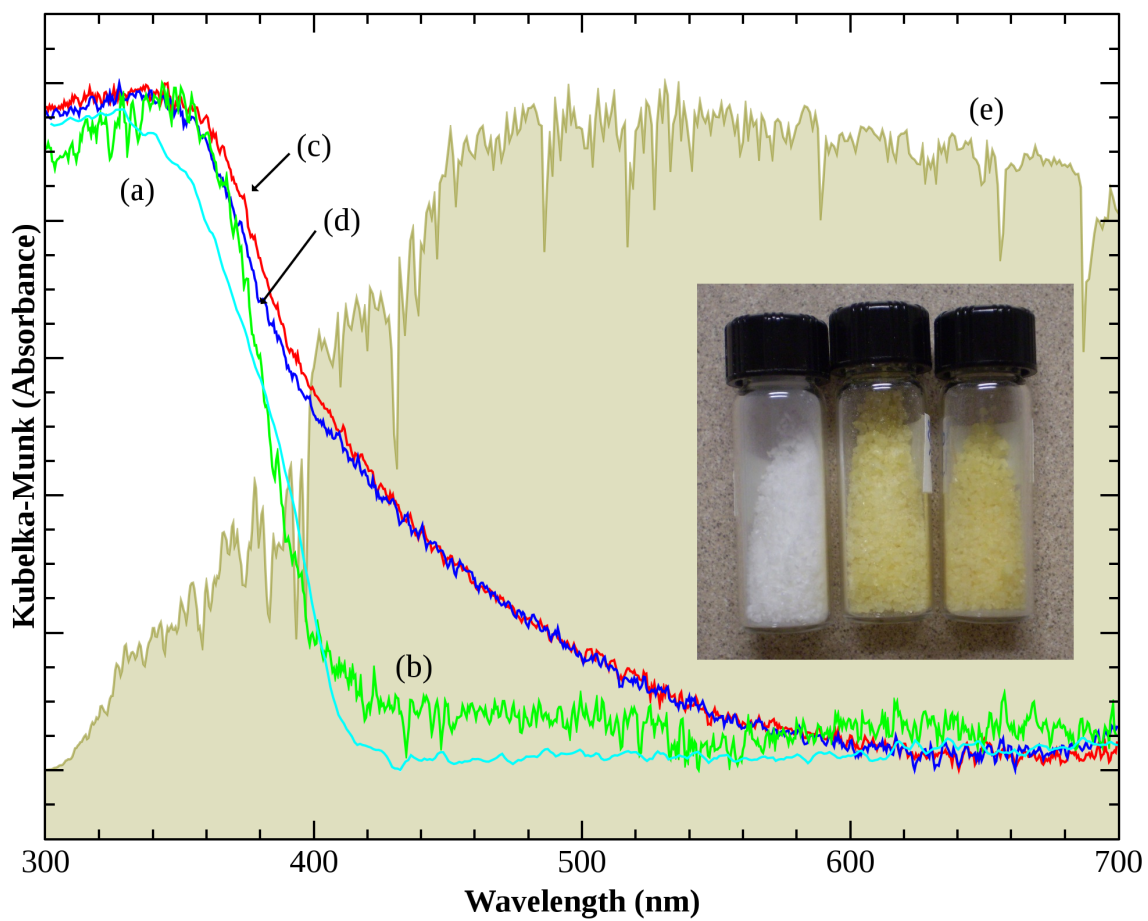


Figure 5.1: DRS of TEA samples. (a) P-25, (b) pure TiO₂, (c) N-doped TiO₂, and (d) F,N-doped TiO₂. (e) shows the AM1.5 solar spectrum. The inset shows a photograph of the samples.

5.1.2 Powders from Inorganic Synthesis

DRS for the synthesis using inorganic precursors is shown in Figure 5.2. Again, the bandgap is lowered for the N-doped samples. The N-doped and fluorinated N-doped samples absorb 140 and 156% of the solar spectrum compared to the pure sample, respectively.

5.1.3 Effect of Doping on O Vacancy Creation

Although many (hundreds) of groups attribute a color change (therefore the bandgap shift) to the incorporation of N, we find that very little color change occurs from the N-doping process. Only a small shift is measured for the bandgap from DRS. A few other groups have also had similar results¹⁴¹, and this author agrees with them that the shift to a yellow color that is cited by many as evidence of N-doping is actually the formation of O vacancy defects and, when using the organic precursors, the formation of N-containing organic molecules such as triethylammonium acetate. This can be confirmed by deconvolution a peak at about 430 nm. Indeed, most groups report N/Ti ratios of 2-4% (by sol-gel methods), which is far below the ~11% (1 N in a unit cell of 8 Ti atoms) used in the initial calculations that predicted a bandgap as low as 2.0 eV¹⁹. Additionally, the computational method they used (LDA) is known to have shortcomings, which was corrected for in the original paper to bring the calculated values in line with experimental values.

A distinct correlation in the color intensity with extended time in the vacuum drying chamber was observed, as expected for the creation of V_O , which create F-type color centers at ~430-440 nm¹⁴¹.

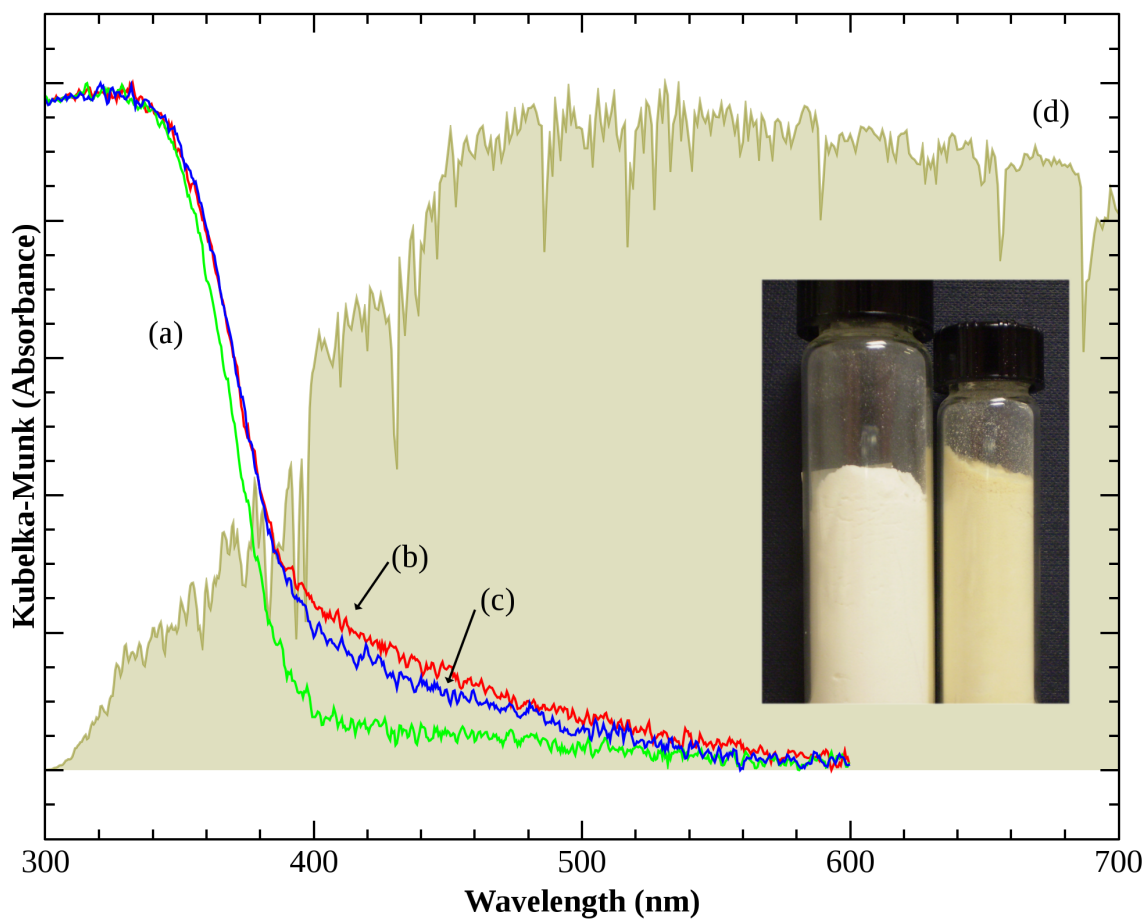


Figure 5.2: DRS of NH_4Cl samples. (a) pure TiO_2 , (b) N-doped TiO_2 , (c) F,N-doped TiO_2 . (d) shows the AM1.5 solar spectrum. The inset shows a photograph of the samples.

To investigate this, another synthesis was performed, and the pressure of the vacuum drying chamber closely monitored. When the pressure dropped below the vapor pressure of water (about 0.5 Torr for water at -25 °C), it was assumed all of the water in the sample was removed from the sample. These samples were white in color with an estimated bandgap of 386 nm (3.21 eV). XPS confirms that the samples were N-doped. White N-doped samples have been reported by other groups⁹⁶.

It is expected that F doping or F surface treatment will slightly lower the optical bandgap of TiO₂, since the F_{2s} states will mix with and slightly lower the CB of TiO₂¹⁴². A small shift is seen in every case (~0.01 eV), however this shift is extremely small and is not outside experimental error for the experiments described in this work.

Oxygen vacancies (V_O) are known to form by a number of methods, most commonly by electron bombardment or UHV annealing^{130,141}. The V_O introduces DOS below the CB, thereby reducing the bandgap to as low as 2.0 eV¹⁴³. It is shown in this work that long term (1-5 days) vacuum exposure from the drying process also induces V_O formation.

It has been theoretically predicted that N-doping significantly lowers the formation energy for an V_O (from 4.2 to 0.6 eV)⁵⁴. This work confirms that after an otherwise identical treatment, the N-doped sample has an increased amount of V_O (Figure 5.3). This is evident in the DRS spectra as a buried peak at about 430 nm¹⁴³, that grows in intensity (arrow 2 in Figure 5.3). The bandgap lowering due to N-doping is evidenced by a shift in the absorption edge (arrow 1 Figure 5.3).

This work also shows that surface F has the opposite effect, preventing the formation of V_O, as shown in Figure 5.4. A N-doped sample was treated in a NaF solution at an acidic pH (~3)

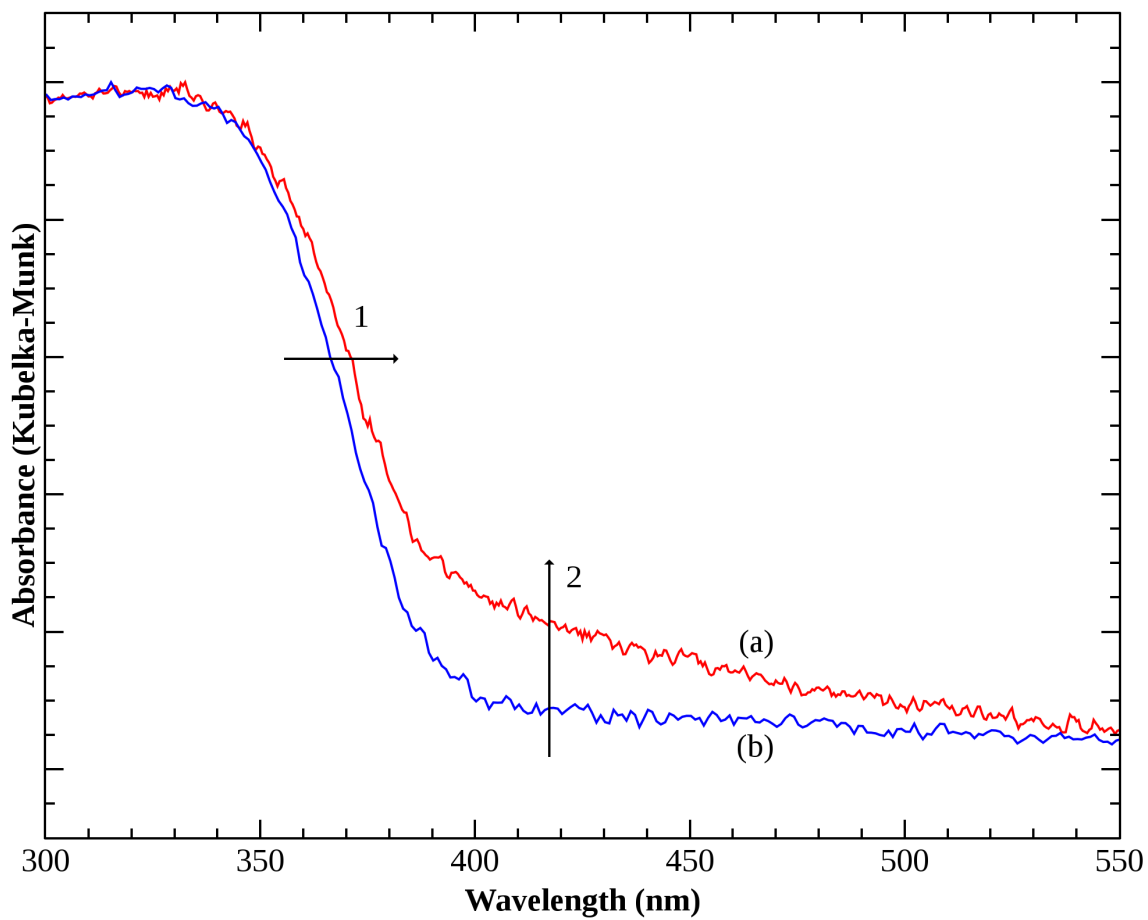


Figure 5.3: DRS of (a) N-doped and (b) pure (undoped) NH_4Cl samples. The bandgap shift is shown by arrow 1, and the creation of O vacancies is shown by arrow 2.

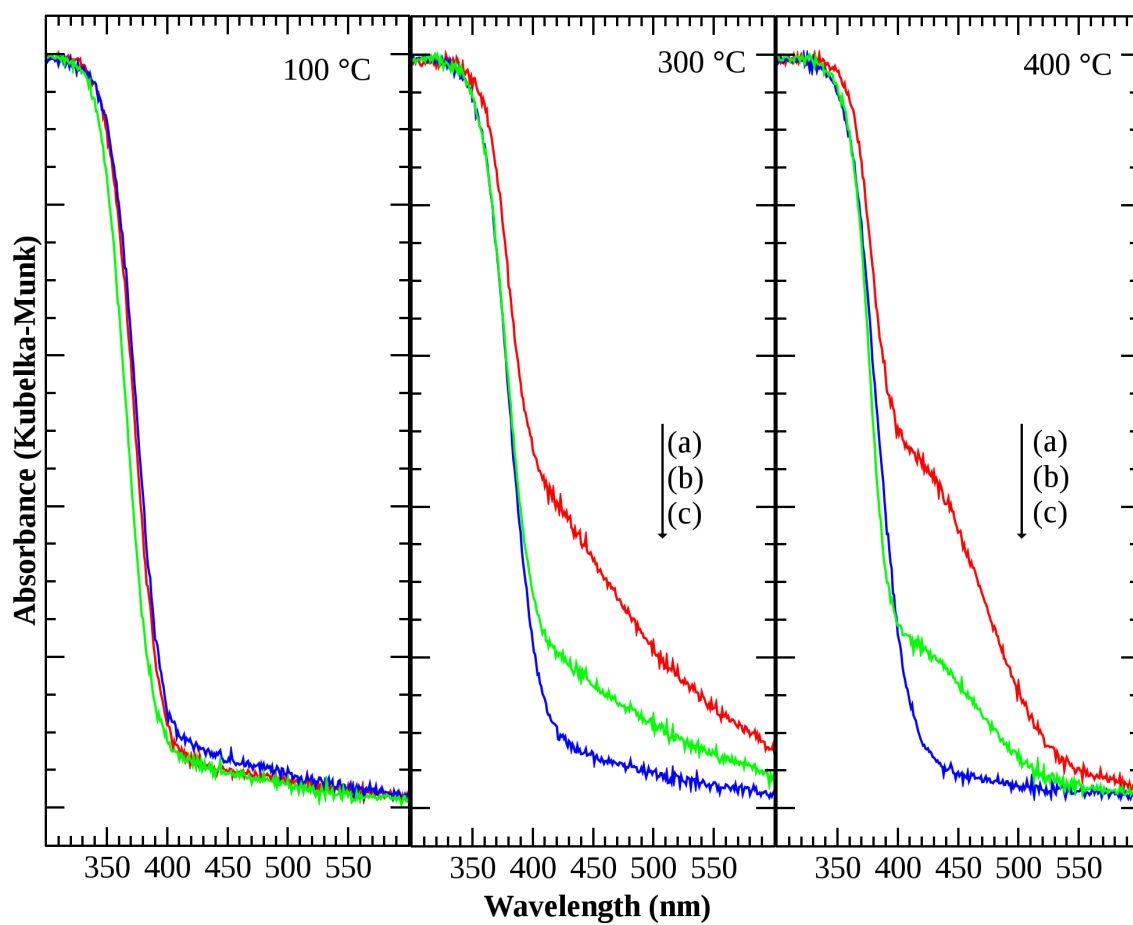


Figure 5.4: DRS at various annealing temperatures for (a) N-doped TiO_2 , (b) N-doped TiO_2 with a small amount of surface F, and (c) N-doped TiO_2 with the surface saturated in F for NH_4Cl samples.

to saturate the surface with F. This sample had anatase character. Another sample was treated in a NaF solution at a neutral pH (~ 7) to induce a partial coverage of the surface with F. With increasing annealing temperatures, V_O were induced in the N-doped TiO_2 . V_O formed to a lesser extent in the partially fluorinated sample, and nearly no V_O formation was seen in the sample with a saturated surface. To the author's knowledge, this has not been reported before.

5.2 Photodegradation of MB

5.2.1 Effect of N-doping and Surface Fluorination

For the experiments testing the effects of N-doping, the 560 nm shortpass filter was not used. This led to the major part of the degradation being attributed to the autodecomposition of MB.

The samples were tested for their photoactivity by monitoring the degradation of MB as described in §2.8. This produces results that exclude the photoactivity due to the native ability of the TiO_2 , and only the photoactivity due to the extended absorption is measured. The normalized photodegradation data is shown in Figure 5.5. The cuvettes with the MB and TiO_2 were not irradiated for the first 90 minutes to allow the MB to absorb to the TiO_2 and the reaction vessel walls. This is indicated in the figure with a negative reaction time. The rate constants were extracted by the method described in §2.8 to produce the data shown in Figure 5.6.

Figure 5.6.a shows the autodecomposition rate of the MB. Due to the cutoff filter, the pure TiO_2 (Figure 5.6.b) had very little photoactivity, the slight increase in the rate is due to the slight overlap in the filter setup and absorption of pure TiO_2 (see Figure 2.3). The N-doped TiO_2 (Figure 5.6.c) accelerates the rate of MB decomposition by 1.5-fold versus undoped TiO_2 . This indicates that the bandgap has indeed been shifted into the visible and the lowered bandgap is

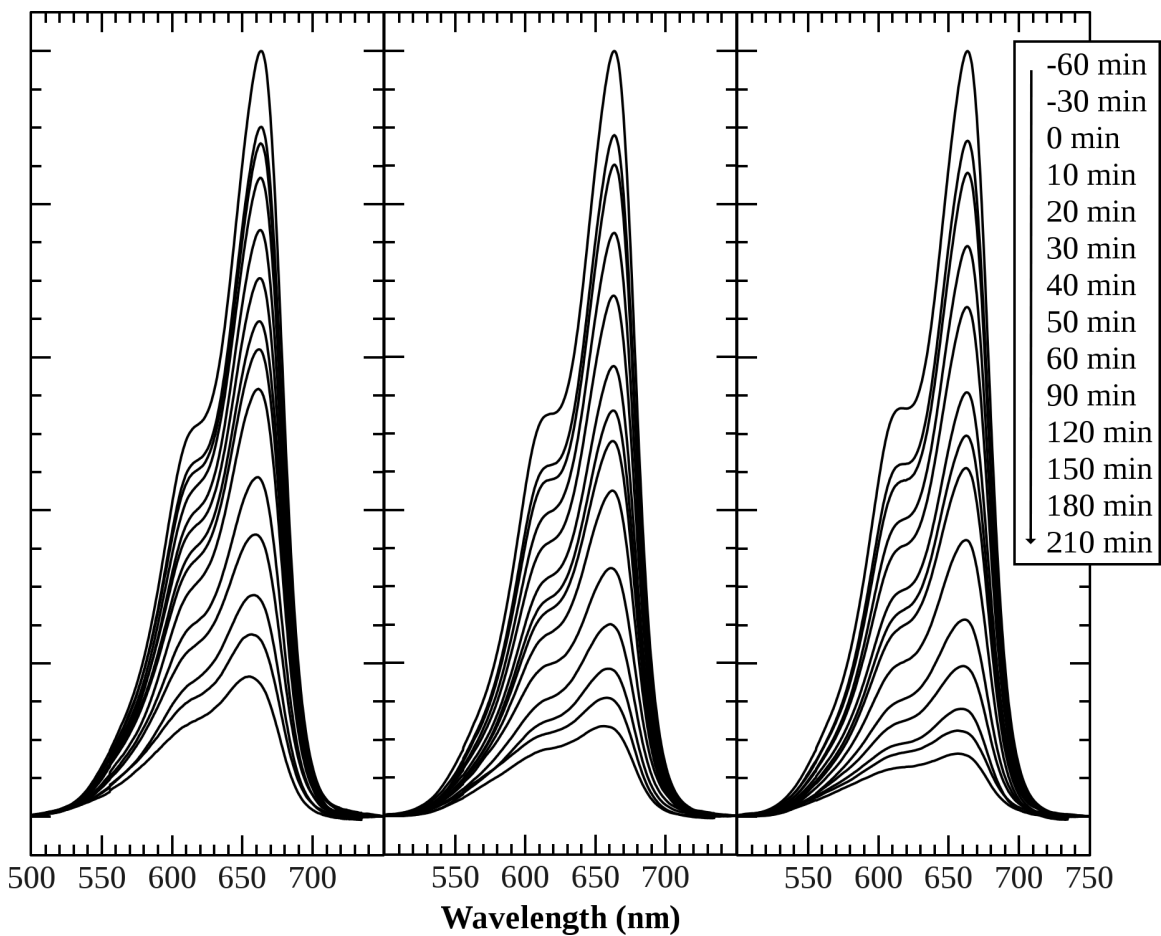


Figure 5.5: Normalized UV-Vis spectra for MB photodecomposition. (a) shows pure, (b) N-doped, and (c) E,N-doped TEA samples

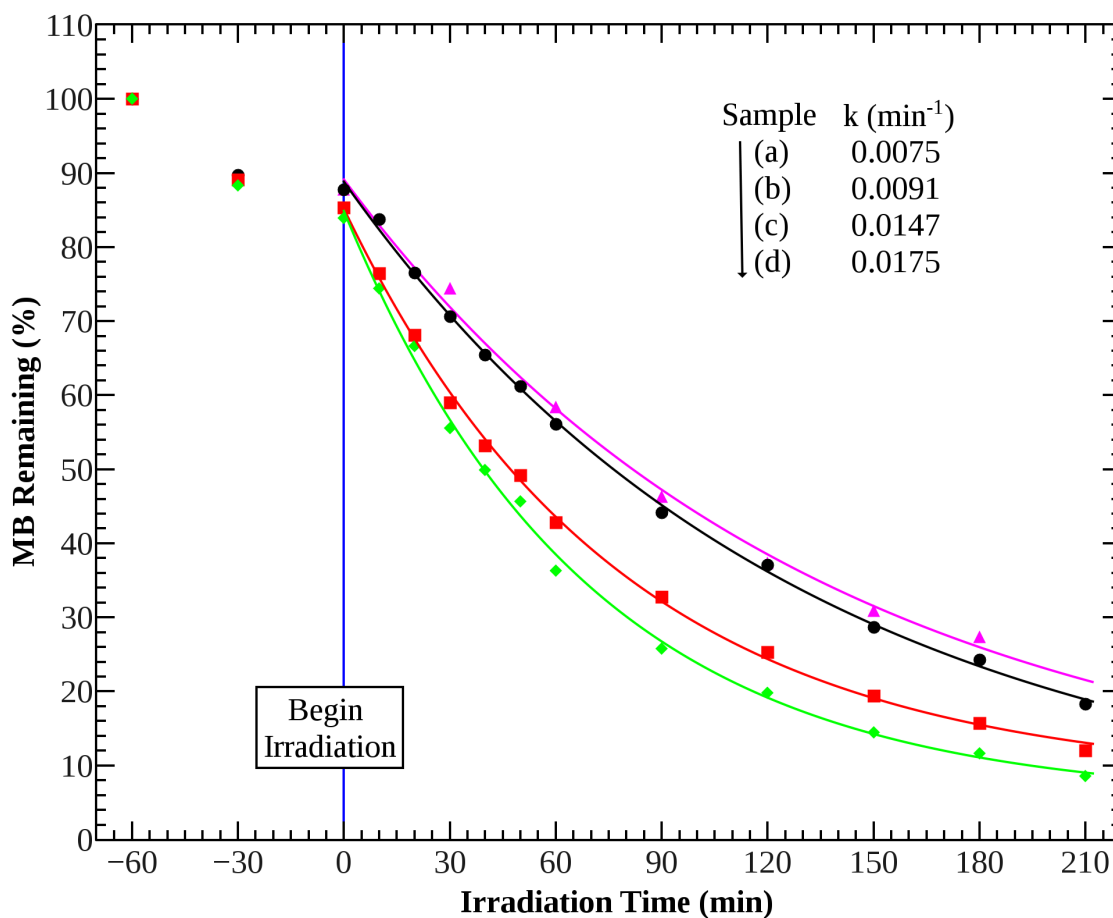


Figure 5.6: Rates for photodecomposition of MB for (a) pure MB, no TiO_2 (b) pure (undoped), (c) N-doped, and (d) N,F-doped TEA samples. The table shows the extracted pseudo first order rate constants.

promoting the degradation reaction. The N,F-doped sample (Figure 5.6.d) shows a 2-fold increase in the pseudo first order rate constant. This is due to the F promoting the production of ROS, especially OH radicals.

As discussed in §1.4.1, MB can decompose by several routes. Literature reports the MB peak shifting by over 40 nm during the demethylation pathway¹⁴⁴. Based on the observation that the peak in the raw spectra shown in Figure 5.5 shifts by only 8 nm, we can conclude that the demethylation pathway is not significant, and that ring cleavage pathway dominates.

To further investigate the decomposition pathway, ESI-MS was done on the decomposition products, shown in Figure 5.7. The 0 min scan shows a peak for 284 m/z due to the MB, and a smaller peak at 270 m/z for Azure B. A peak with an intensity of about 16% of the parent peak is seen due to demethylation in the ionization process, and is seen when pure MB is studied (data not shown) as well being reported in the literature¹⁴⁵. The small peak at m/z = 102 is isopropyl acetate, a contaminant caused by the reaction of excess triethylamine and isopropanol.

After 210 minutes of irradiation time, peaks for Azure B (m/z = 270), Azure A (m/z = 256), and Azure C (m/z = 242) are seen. These peaks are present in much greater abundance relative to the parent MB peak than is caused from the ionization process, indicating they are products of the photoactivity of the TiO₂. However, the abundances do not match with the UV-Vis data. Since the extinction coefficients (ϵ from Beer's Law) of the demethylated products are similar (within an order of magnitude)¹⁴⁶, if the proportions seen in the mass spectrum were present, the UV-Vis would show a very broad, blueshifted peak, the sum of all absorbing molecules. In addition, there is a higher mass peak present at m/z = 317. The 317 peak can be assigned to the species shown in Figure 1.8.

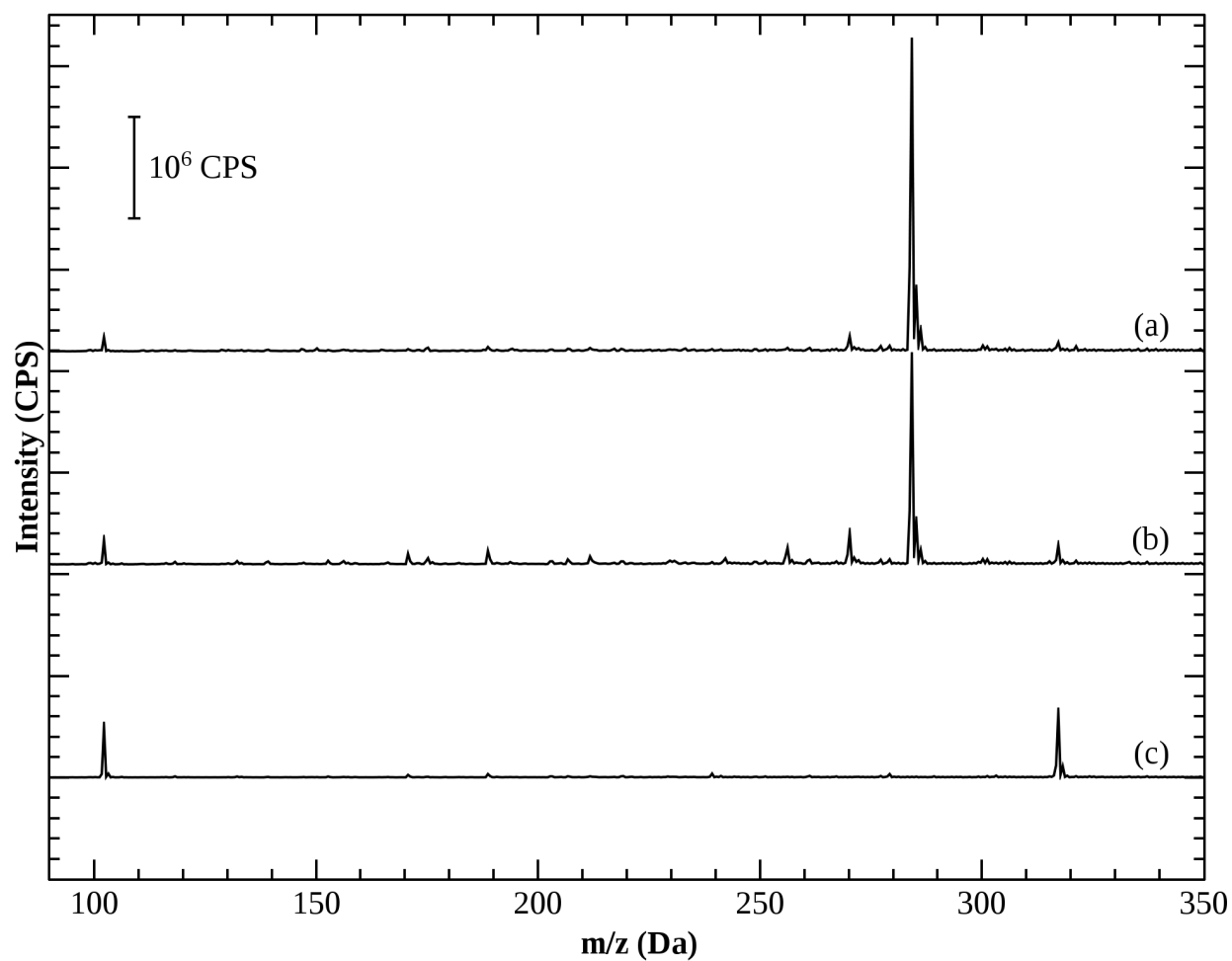


Figure 5.7: ESI-MS of the decomposition products for N-doped TEA samples. (a) shows the sample before irradiation, (b) after 210 minutes of irradiation time, and (c) after 390 minutes.

After 390 minutes of irradiation time, the solution appears colorless and the UV-Vis shows no signal for MB, and a large, broad signal in the UV range due to the remaining derivatized benzene rings (see Figure 1.8). The MS shows only one species at $m/z = 317$.

All this suggests that ring cleavage is the primary degradation mechanism, with a small contribution due to the demethylation pathway.. Since N-doping causes the VB to increase, more e^- s are available to create the ROS superoxide ($O_2^{\cdot-}$), which reacts with the positively charged S on the MB to form the 317 species. Because the 317 species is not charged, only a small fraction of the actual amount is seen in the mass spectrum (see §2.11). This pathway will be termed e^- -mediated, since the ROS are primarily formed by e^- s in the CB.

5.2.2 Effect of Fluorination

As shown in Figures 5.5 & 5.6, fluorination also increases the reaction rate. To investigate this further, samples were partially and fully doped with F by adjusting the pH of the NaF solution. These experiments were done with the full filter setup, so a pure MB and a pure TiO_2 sample show similar amounts of degradation (about 5% in 210 min). This further confirms that the filter setup cuts out the native photoactivity of the TiO_2 . Figure 5.8.a shows the UV-Vis spectra for a control sample (P-25), partially and fully F-doped TiO_2 . With increasing fluorination, the peak shape drastically changes and shifts (Figure 5.8.b & c), indicating that the demethylation products are present and that the demethylation pathway is the primary decomposition pathway. ESI-MS, shown in Figure 5.9 and Table 5.1, confirms the UV-Vis results and clearly shows that fluorinating the TiO_2 surface favors the demethylation decomposition pathway.

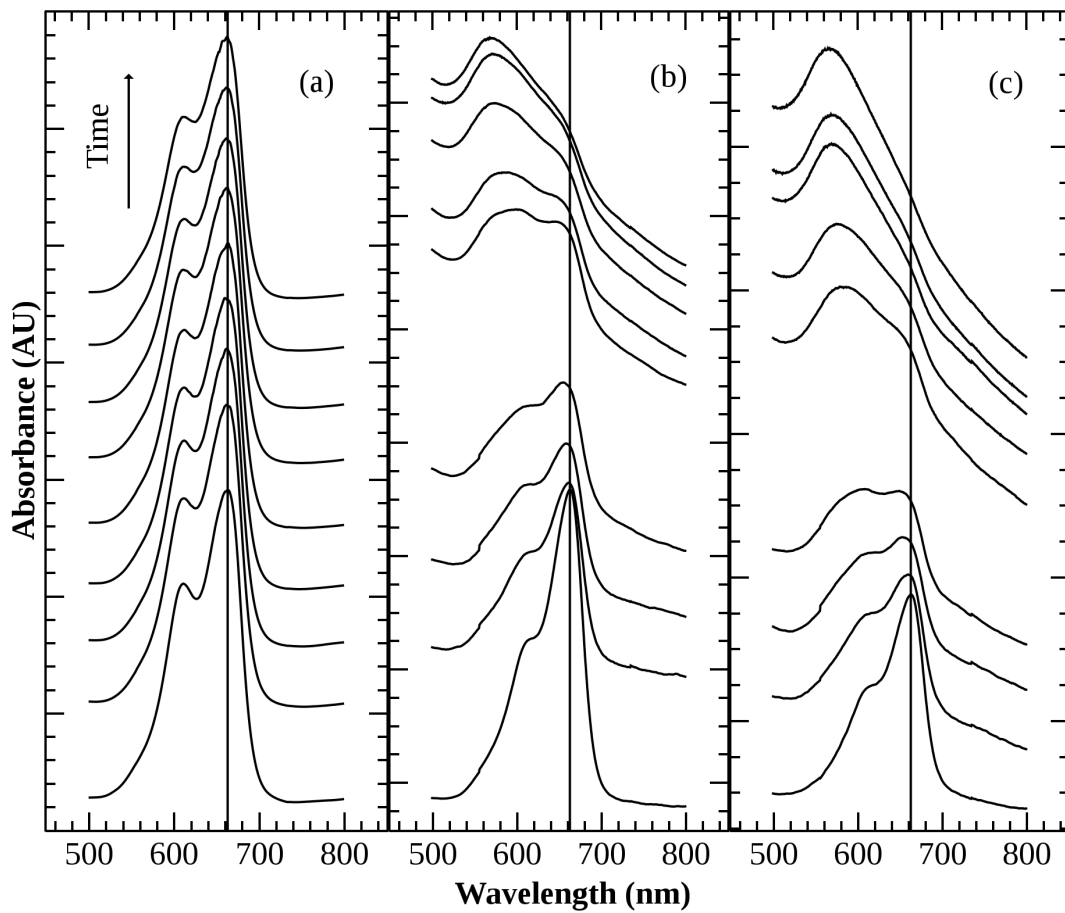


Figure 5.8: UV-Vis spectra for MB degradation. (a) shows Degussa P-25, (b) shows as synthesized N-doped, and (c) shows fluorinated N-doped NH₄Cl samples.

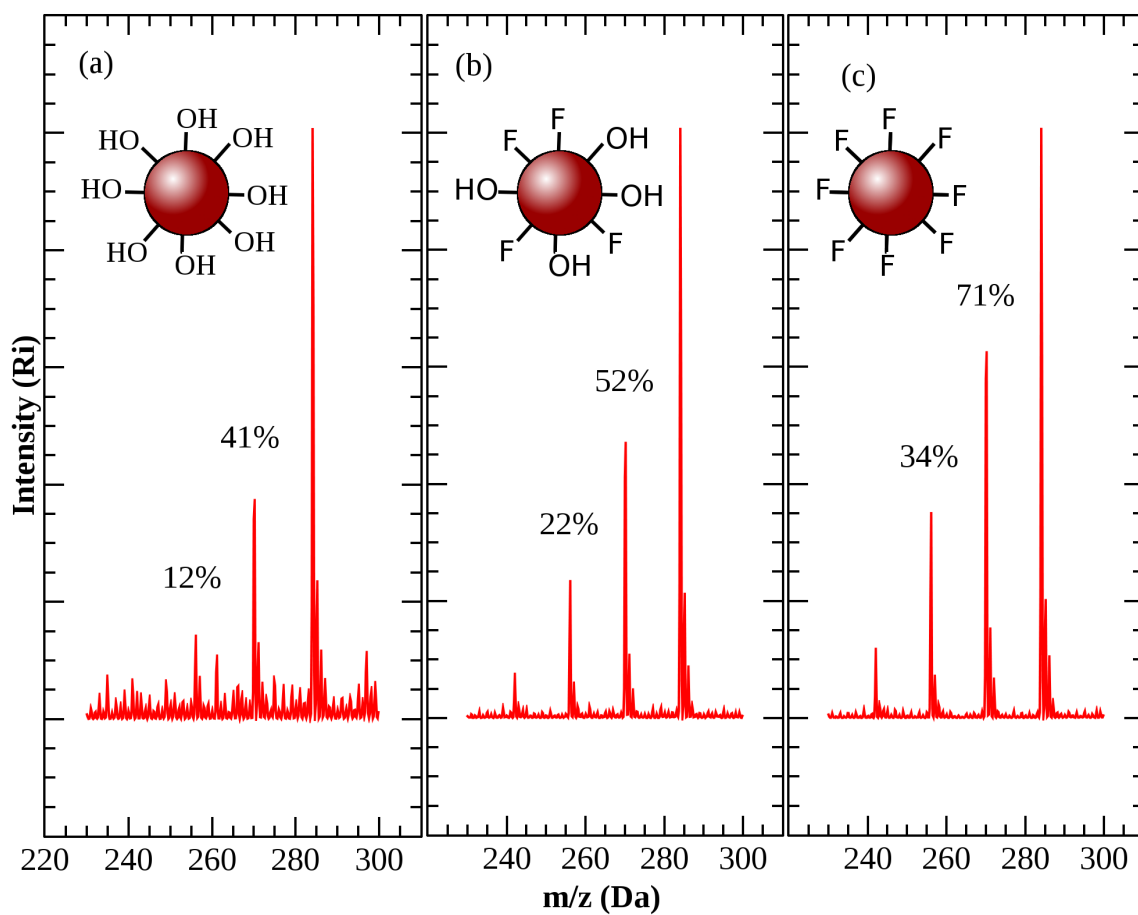


Figure 5.9: ESI-MS showing the effect of fluorination on the degradation path for NH_4Cl samples. (a) shows the as-synthesized N-doped, (b) was fluorinated at pH=7, and (c) was fluorinated at pH=3.

Sample	Methylene Blue (m/z = 284)	Azure B (m/z = 270)	Azure A (m/z = 256)	Azure C (m/z = 242)
pure MB	100%	16.7%	7.6%	3.5%
Inorganic N-doped	100%	41%	12%	0%
Partially Fluorinated Inorganic N-doped	100%	52%	22%	6.2%
Fully Fluorinated Inorganic N-doped	100%	71%	34%	10.6%

Table 5.1: Comparison of the relative amounts of demethylation products as a function of amount of absorbed fluoride.

It is known that fluorination promotes the creation of hydroxyl radicals ($\cdot\text{OH}$)^{90,144} from h^+ s (see §1.3.3). These then degrade MB by the demethylation pathway, as shown in Figure 1.7. This pathway can be termed h^+ -mediated, since the ROS are generated from the VB holes.

5.2.3 Effect of Annealing and Surface Area

Several groups report that moderate annealing improves the photoactivity¹²⁷. To investigate this further, samples were annealed at 100 °C increments and the photoactivity measured as shown in Figure 5.10. It is evident from this data that the photoactivity declines with higher annealing temperatures. The rate constants are tabulated in Table 5.2.

This effect can be directly attributed to the reduction of the surface area of the particles. Even with moderate annealing, the particles sinter and loose surface area. Since these measurements are taken in identical conditions, the initial amount of MB adsorbed to the particle is directly correlated to the surface area. Figure 5.11 compares the amount of MB adsorbed to the rate constant. There is a rough linear relationship. Three types of TiO_2 were tested: N-doped TiO_2 , anatase N,F-doped TiO_2 , and amorphous N,F-doped TiO_2 . All three followed the same linear relationship, indicating that the dominant factor in the photodegradation reaction is the surface area.

Figure 5.12 compares the rate constants as a function of temperature and suggests that in the case of N-doped TiO_2 , moderate annealing does increase the rate per surface area. This effect is not seen when the TiO_2 is fluorinated, implying that the annealing is driving off surface groups that are not present in the fluorinated particles due to the F displacing the surface OH groups.

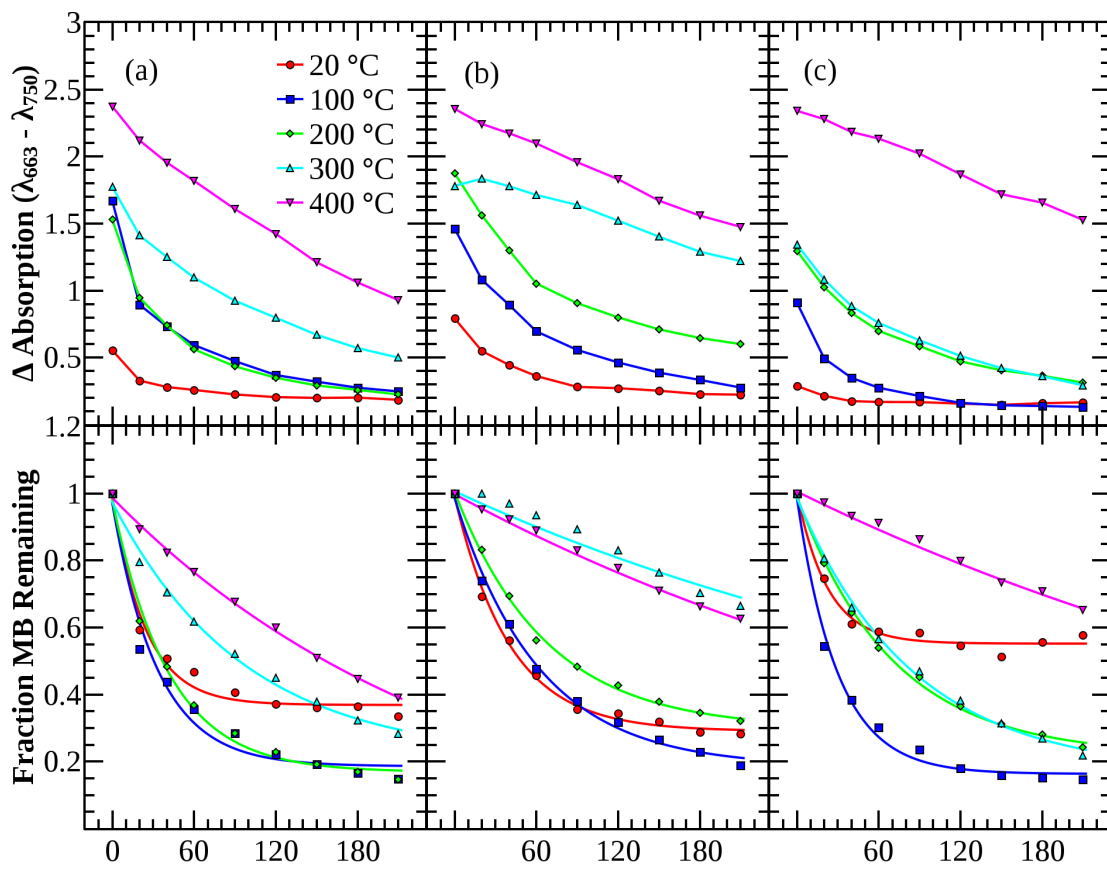


Figure 5.10: Effect of annealing on the photodegradation rate of MB. (a) shows N-doped, (b) anatase N,F-doped, and (c) amorphous N,F-doped NH_4Cl samples.

Sample		MB Absorbed (mmol/g)	N/Ti Ratio (%)	F/Ti Ratio (%)	Rate Constant k (min ⁻¹)
N-doped TiO ₂	Unannealed	0.115	5.68	--	0.0041
	100 °C	0.070	4.88	--	0.0030
	200 °C	0.077	4.04	--	0.0024
	300 °C	0.065	2.08	--	0.0010
	400 °C	0.032	2.05	--	0.0004
anatase F,N-doped TiO ₂	Unannealed	0.106	7.16	55.4	0.0025
	100 °C	0.080	4.61	55.0	0.0016
	200 °C	0.060	3.08	41.1	0.0015
	300 °C	0.065	1.88	16.0	0.0002
	400 °C	0.033	2.39	8.3	0.0002
amorphous F,N-doped TiO ₂	Unannealed	0.124	3.20	10.2	0.0044
	100 °C	0.102	2.98	8.7	0.0034
	200 °C	0.087	2.35	8.4	0.0014
	300 °C	0.085	2.36	9.8	0.0012
	400 °C	0.034	1.21	17.0	0.0002

Table 5.2: Summary of surface areas, N and F amounts, and MB decomposition rate constants versus annealing temperature for N-doped TiO₂ from the NH₄Cl synthesis.

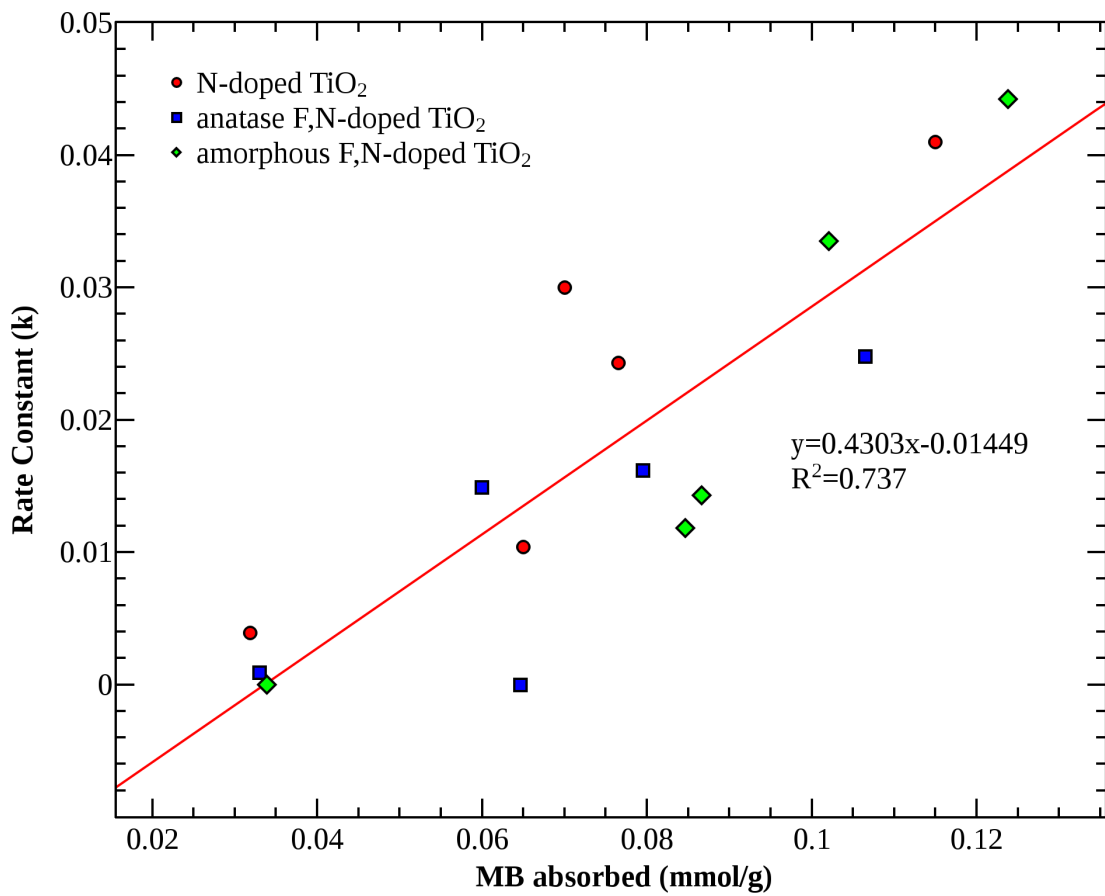


Figure 5.11: Effect of surface area on the rate constant. ● shows N-doped, ■ shows anatase F,N-doped, and ◆ shows amorphous F,N-doped NH₄Cl samples.

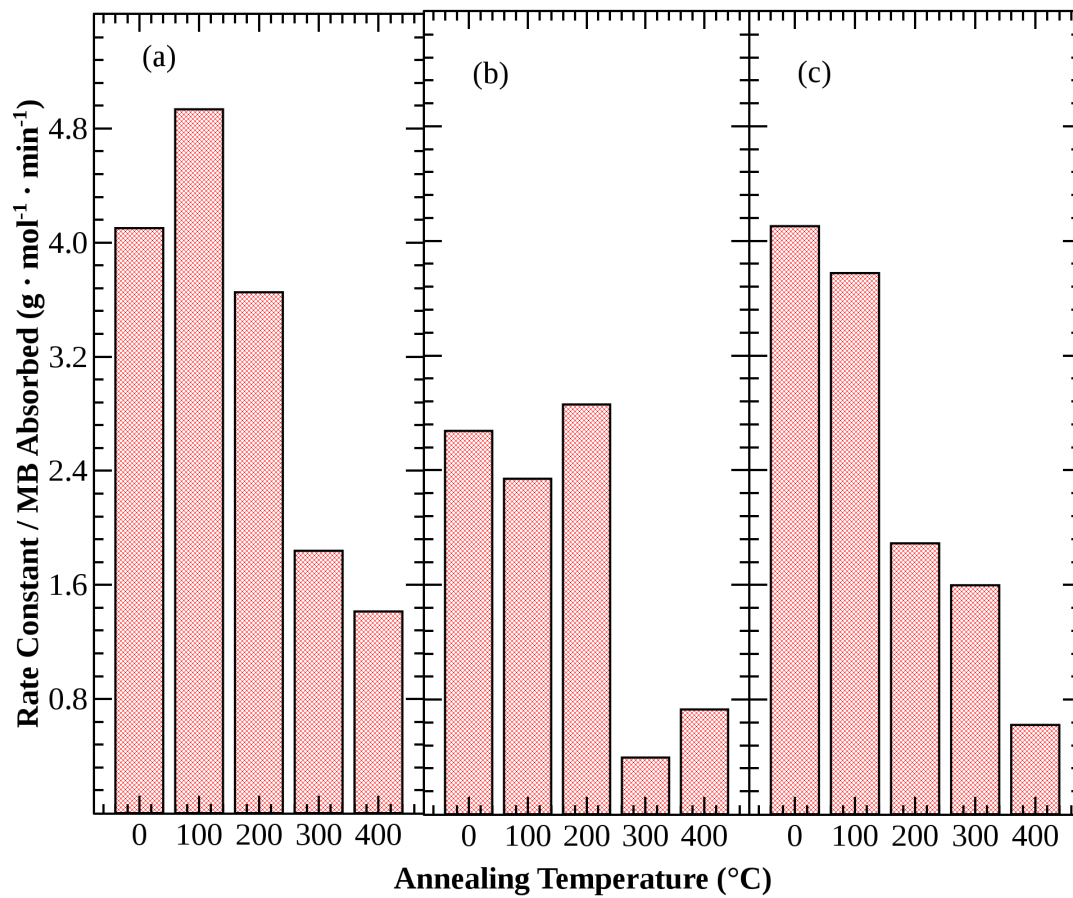


Figure 5.12: Comparison of the rate as a function of the surface area. (a) shows N-doped, (b) anatase N,F-doped, and (c) amorphous N,F-doped NH₄Cl samples.

5.2.4 Effect of Crystallinity

As seen above, the presence of anatase phase (induced by the fluorination process) does not improve the photoactive rate. However, these samples only have anatase structure on the surface. XRD comparisons to P-25 (a known amount of anatase) reveal that the samples are still more than 95% amorphous. Since light has a penetration depth many times the maximum charge carrier distance, having a bulk crystal structure would be beneficial.

To investigate the effect of long range crystallinity, three N-doped TiO₂ samples were chosen that had all been annealed to 300 °C and that showed similar initial MB absorption amounts. The XRD spectra for these samples is shown in Figure 4.12.b, 4.12.d, and 4.12.e. The results are shown in Figure 5.13. The long range crystallinity has a clear effect in promoting the degradation of MB.

5.3 Conclusions

It was found that doping the TiO₂ with organic and inorganic precursors both provided an increase in the amount of visible light absorbed and an increase in the photoactivity. The mechanism for photodegradation was much different depending on the precursor: the organic N precursors promoted the ring cleavage pathway by a CB e⁻ mediated pathway, while the inorganic N precursors promoted the VB h⁺ mediated reactions.

Fluorination promoted the photoactivity and changed the mechanism. While N-doped TiO₂ utilized the e⁻-mediated ring cleavage pathway, the fluorinated surfaces increased the production of ·OH radicals and promoted the H⁺-mediated demethylation pathway.

It was found that the single largest contribution to the photoactivity of TiO₂ is the surface area of the particles. Only long-range crystallinity proved to be beneficial to the photoactivity,

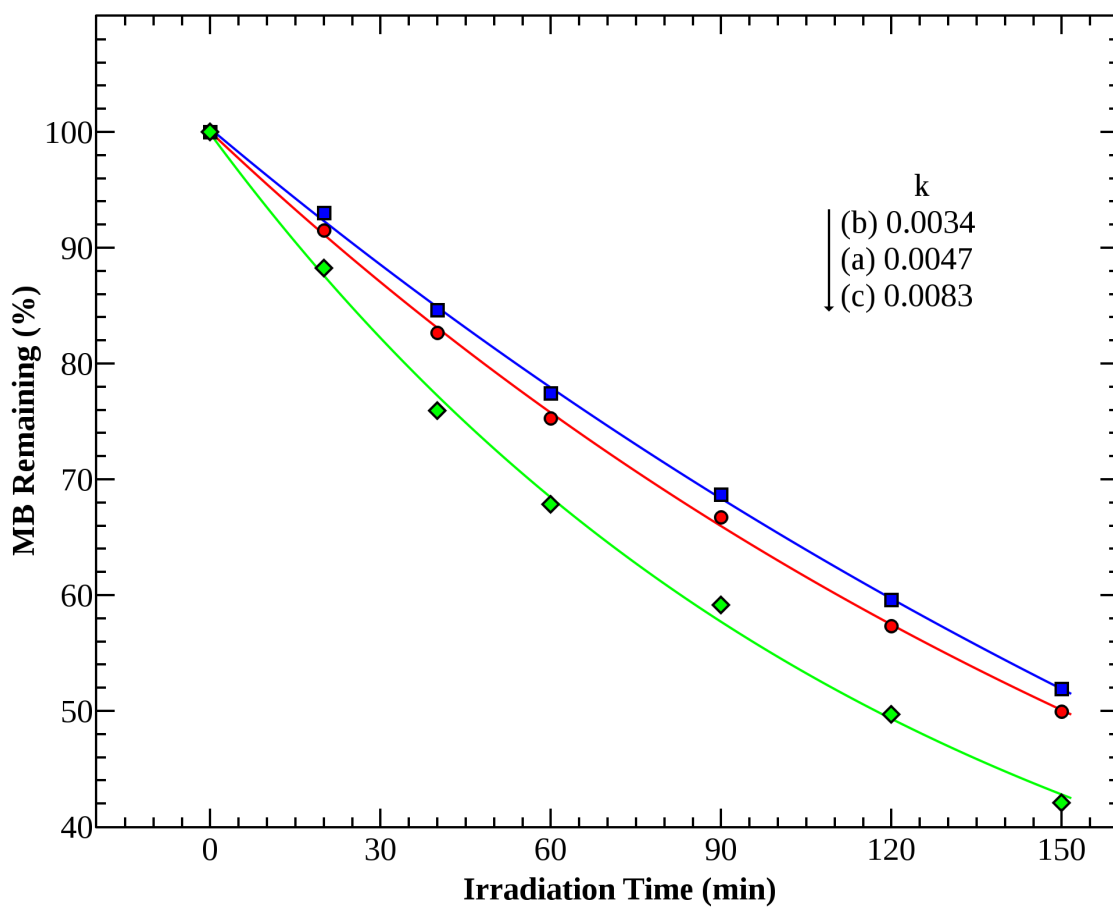


Figure 5.13: Photodecomposition rates of MB for N-doped NH_4Cl samples annealed at 300 °C for 6 hours. (a) annealed, (b) annealed then fluorinated with a 10 mM NaF solution, (c) fluorinated then annealed.

which would require high temperature annealing that would sinter the particles. Several groups have reported that moderate annealing is beneficial to the photoactivity, however this work demonstrates that the loss in surface area from the annealing process is more detrimental to the total photoactivity than any increase gained from the annealing process.

CHAPTER 6 - CONCLUSIONS

6.1 This Work

6.1.1 Synthesis

The work described in this dissertation describes a new method to synthesize high surface area, N-doped, surface fluorinated anatase TiO₂. An organic and an inorganic N source was used. Using vibrational spectroscopy, it was found that the organic N source, triethylamine (TEA), left significant amounts of organic impurities in the final product. Using an inorganic N source, ammonium chloride (NH₄Cl), eliminated these impurities.

The surface hydroxyls were exchanged for fluoride in an post-synthesis reaction, allowing the amount of N and F to be independently controllable. XPS confirms that the F is not multicoordinate (F-doped TiO₂).

XPS reveals that the TEA synthesis contains a single nitrogen species with a binding energy of 400.6 eV. In contrast, when NH₄Cl was used as the nitrogen precursor two nitrogen species were observed with binding energies at 402.6 and 401.2 eV. These are assigned to interstitial nitrogen in the N¹⁺ and N⁰ oxidation states.

6.1.2 Crystallinity

The samples are synthesized at ambient temperatures and are never heated, and unsurprisingly XRD confirms that they are amorphous. Annealing converts the samples to anatase at lower temperatures and to rutile at very high temperatures.

Anatase character can also reproducibly be achieved by treating amorphous TiO₂ particles in an acidic solution of NaF. This process is exponentially saturating, with a rate dependent on the concentration of NaF and reaction time, not the pH. However, the anatase produced has little to no effect on the photoactivity of the particles. N-doping is retained during the anatase formation process.

It is also shown that the absorbed F affects the phase transition temperature, and allows near 100% anatase powders to be formed at temperatures well below those currently reported and below the temperature at which most dopants are driven out.

In a recent review²⁹, M. Henderson notes “Often, it is difficult to evaluate the influence of an additive on photocatalytic behavior from a fundamental, molecular-level perspective because of the complex natures of most TiO₂ samples and preparation methods.” This author enthusiastically concurs, and points out that it proved to be extremely difficult even in synthesizing one batch identical to the last. The chemical precursors used, rate of TTIP addition, reaction vessel temperature, stirring speed, and time spent in the drying vacuum system all affected the appearance and activity of the final product.

6.1.3 Photoactivity

Both samples exhibited lowered bandgaps and increased optical absorption compared to the undoped samples. The TEA samples was found to have organic amines that contributed to the optical absorption and the NH₄Cl samples were found to have oxygen vacancies that increased the optical absorption. Both N-doped samples showed enhanced photoactivity compared to pure TiO₂ made by the same method. Fluorination further enhanced the photodegradation in both samples. When TEA was the dopant precursor, MB primarily decomposed by a ring-cleavage

pathway using superoxide. In contrast, when NH_4Cl was the dopant precursor, MB decomposed through demethylation pathway induced by hydroxyl radicals. Fluorination promotes the demethylation pathway.

Despite the enhancements gained from N and F-doping, this work shows that the surface area of the TiO_2 particles plays the primary role in the photoactivity. Even low annealing temperatures often used as a matter of routine in the synthesis process directly and drastically affects the surface area of the particles.

6.2 Future Work

6.2.1 F^- adsorption

It would be interesting to undertake a systematic study of the amount of F adsorbed by the TiO_2 as a function of pH, and to compare this to the measured PZC. Changing the PZC by various treatments should then alter that amount of adsorbed F^- . Also interesting would be to quantify the F by XPS as a function of time. Since surface fluorination occurs very quickly, and the anatase transformation takes several hours, this would separate the role of the anatase in the F absorption. Although there is no evidence in the XRD or XPS peak positions for TiOF_2 .

6.2.2 Anatase formation

This work has determined that the pH of the NaF solution is important, and that the threshold for the formation of anatase occurs suddenly (from 1% to 99% of saturation within 1 pH unit) and is a function of both the concentration of HF in solution and the PZC of the material. This sudden onset is abnormal and continued studies would certainly prove interesting.

6.2.3 Phase Transition Temperature

It is clear that surface F plays a role in crystallization of TiO₂ particles when annealed. This is generally referred to as the phase transition temperature (PTT). While a large number of groups have studied the influence of doping on the anatase → rutile PTT, the influence of surface groups or the amorphous → anatase PTT has not been adequately studied.

6.2.4 BET Studies

The surface area of the particles plays a huge role in their photoactivity, however, it was difficult to get reliable surface area measurements without access to a commercial BET instrument. Since it was found that the surface area of the particles is critical to the photoactivity, BET studies correlating the surface area to the extent of fluorination would undoubtedly yield interesting results. Additionally, investigating the change in pore volume and size as a function of fluorination and annealing would prove very interesting.

6.2.5 Other Analyte Molecules

This research focused on a single analyte molecule, MB, to test the photoactivity of the TiO₂. Other analytes such as 4-chlorophenol, methyl orange, rhodamine B and others have been used in the literature and would yield different results due to the different charges on the molecules.

CHAPTER 7 - ADDITIONAL EXPERIMENTS

7.1 Effect of N on Surface Group Retention

The FTIR spectra of N-doped and undoped TiO₂ as a function of fluorination is shown in Figure 7.1. The two peaks seen at 1443 and 1536 cm⁻¹ are surface bicarbonate groups from absorbed atmospheric CO₂. The shoulder at 1620 cm⁻¹ corresponds to the bending mode of surface >OH₂ groups¹⁴⁷. The Ti-O-H stretching mode is buried in the broad peak between 3000 – 3500 cm⁻¹. The broad peaks from 400 – 1000 cm⁻¹ are the bulk absorbance of the TiO₂.

The retention of bicarbonate groups varied between the N-doped and undoped samples. Outside of the photoactivity, this is the only area where differences in the properties of N-doped and undoped samples was noticed. Figure 7.1.a shows that N-doped and undoped samples as synthesized have similar amounts of carboxylate ions on the surface. Figure 7.1.b is after fluorination in 10 mM NaF, Figure 7.1.c after 100 mM NaF. The N-doped sample show a large reduction in the amount of carboxylate ions after only 10 mM treatment, something that is not achieved with with the undoped sample even after treating with 100 mM NaF. XRD shows that the amount and size of the anatase crystallites are similar (Figure 7.2). This confirms that the influencing factor is the N-dopant.

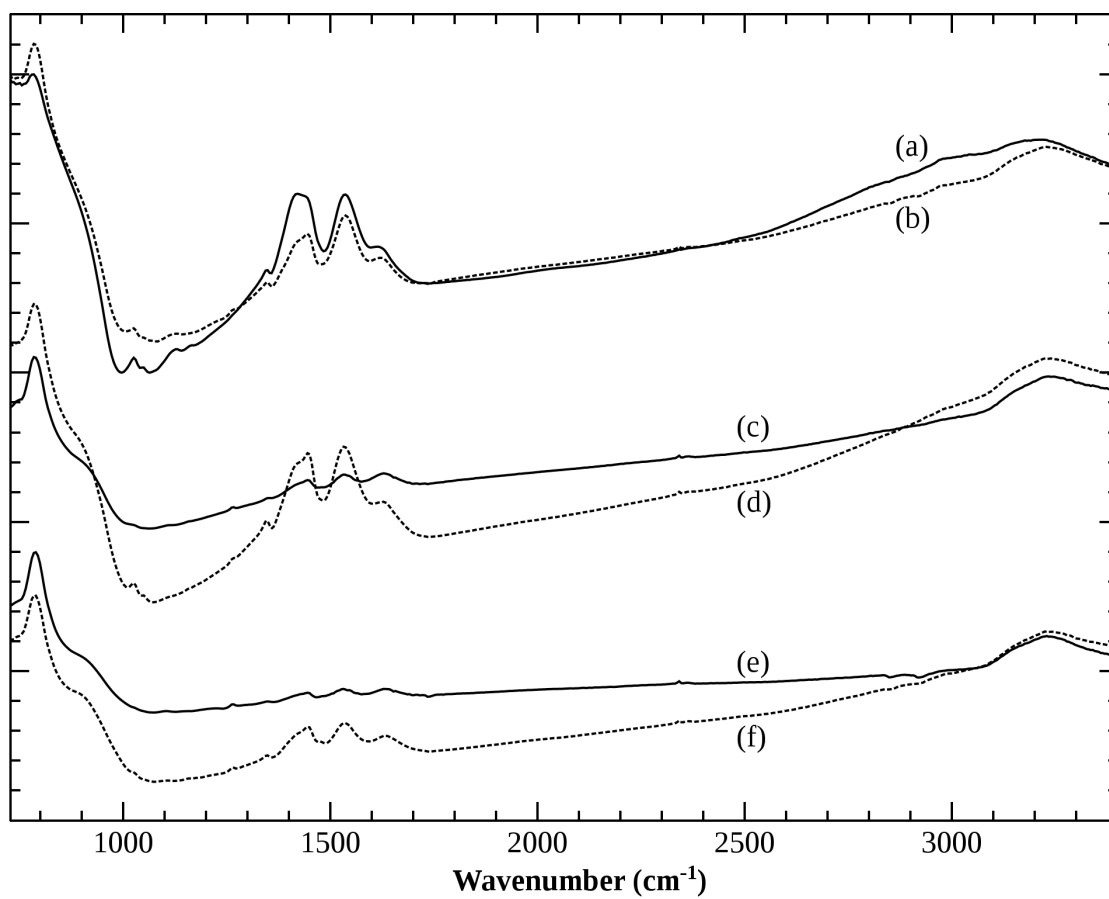


Figure 7.1: FTIR of N-doped NH₄Cl samples shown as a solid line, and undoped NH₄Cl samples shown as a dashed line. Lines (a) and (b) are untreated, (c) and (d) are treated with 10 mM NaF, and (e) and (f) are treated with 100 mM NaF.

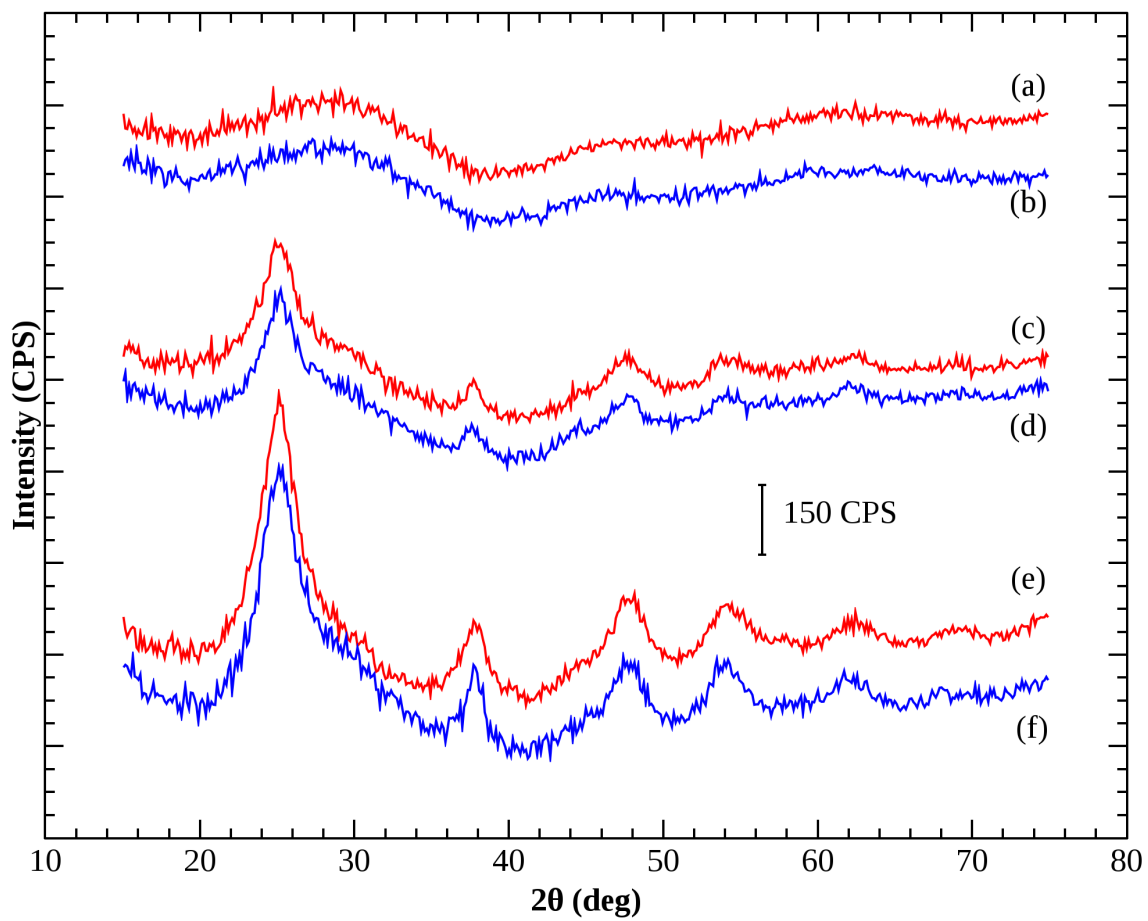


Figure 7.2: XRD of undoped (a, c, and d), and N-doped (b, d, and f) NH_4Cl samples, as made (a,b), after treatment with 10 mM NaF (c,d), and 100 mM NaF (e,f).

7.2 Metal-doped TiO₂

To synthesize metal-doped TiO₂, 0.01 moles of the metal chloride salt is added to ~60 mL of the nanocolloid discussed in §3.2. This is stirred at 0 °C overnight and is then dried by the same process discussed in §3.2, without the subsequent washing. TiO₂ doped with Fe, Co, Cu, and V in various oxidation states and concentrations was synthesized by this method. Although the synthesis seemed to work and produced results consistent with the literature⁵⁰ in terms of appearance, we found that in every case the metal was not incorporated into the TiO₂ lattice, but rather co-crystallized as the metal chloride. This can be seen in the XPS, where the Cl is evident. Additionally, upon washing the brightly colored samples with water, the metal salt readily dissolved leaving the brown TiO₂ behind. Although XPS shows that some residual metal remains in the powder after washing, the results question the validity of calling the samples “metal-doped”.

7.3 Effect of pH and Buffers on Photoactivity

It is well known that the pH of the solution when the MB degradation was being carried out was critical to the degradation rate. Figure 7.3 shows the effect of varying pH on the degradation rate. This is in large part due the negative surface charge on the particles in basic solutions that attracts the MB cation. For this reason it was critical to keep the pH steady across all experiments. This effect can be seen in the absorbance of MB on the particles in the absence of irradiation, noted in Figure 7.3 as negative reaction times.

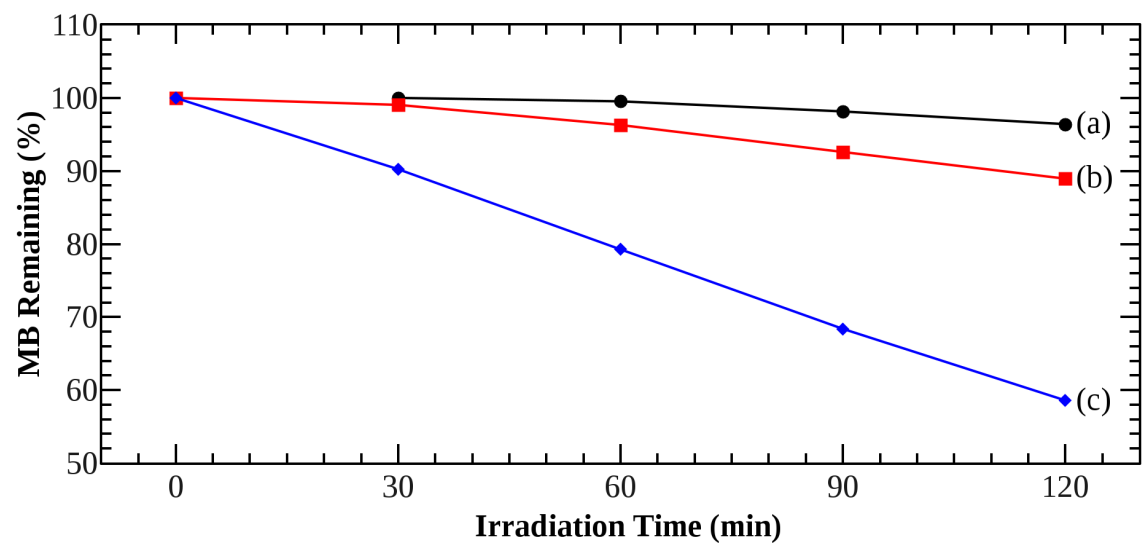
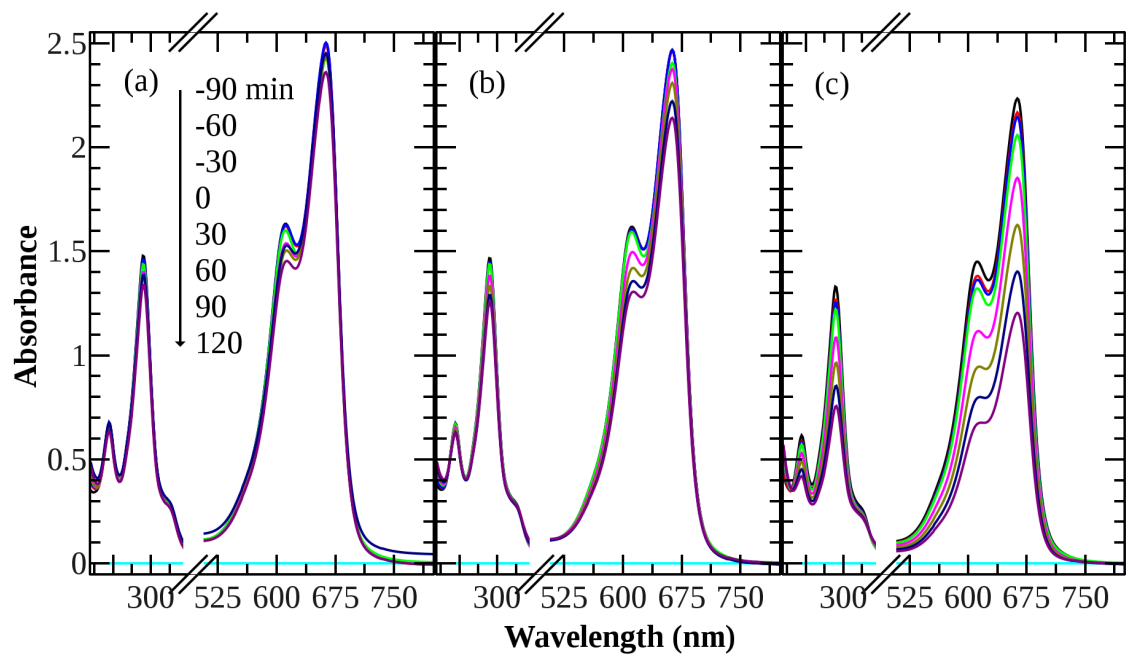


Figure 7.3: pH dependance for MB degradation. (a) at pH = 4, (b) pH = 7, and (c) pH = 10.

Naturally, first attempts at controlling the pH would lead to buffer solutions. Several buffers were tried, including acetate, phosphate, borate, and carbonate buffers, however, the buffers were found to greatly affect the photodegradation rate and mechanism. It was found that MB's tendency to autodegrade took place by different routes depending on the buffer used, as shown in Figure 7.4. This data was collected by irradiating pure MB (no TiO₂) with the filter setup without the 560 nm shortpass filter. The different peak shapes indicate that various decomposition routes are at work and completely different intermediates are being formed. The cause may be related to the double layer formed with the buffers interacting with the MB molecules.

For this reason only HCl and NaOH were used to adjust the pH in this work, although control experiments showed that any strong acids or bases are suitable.

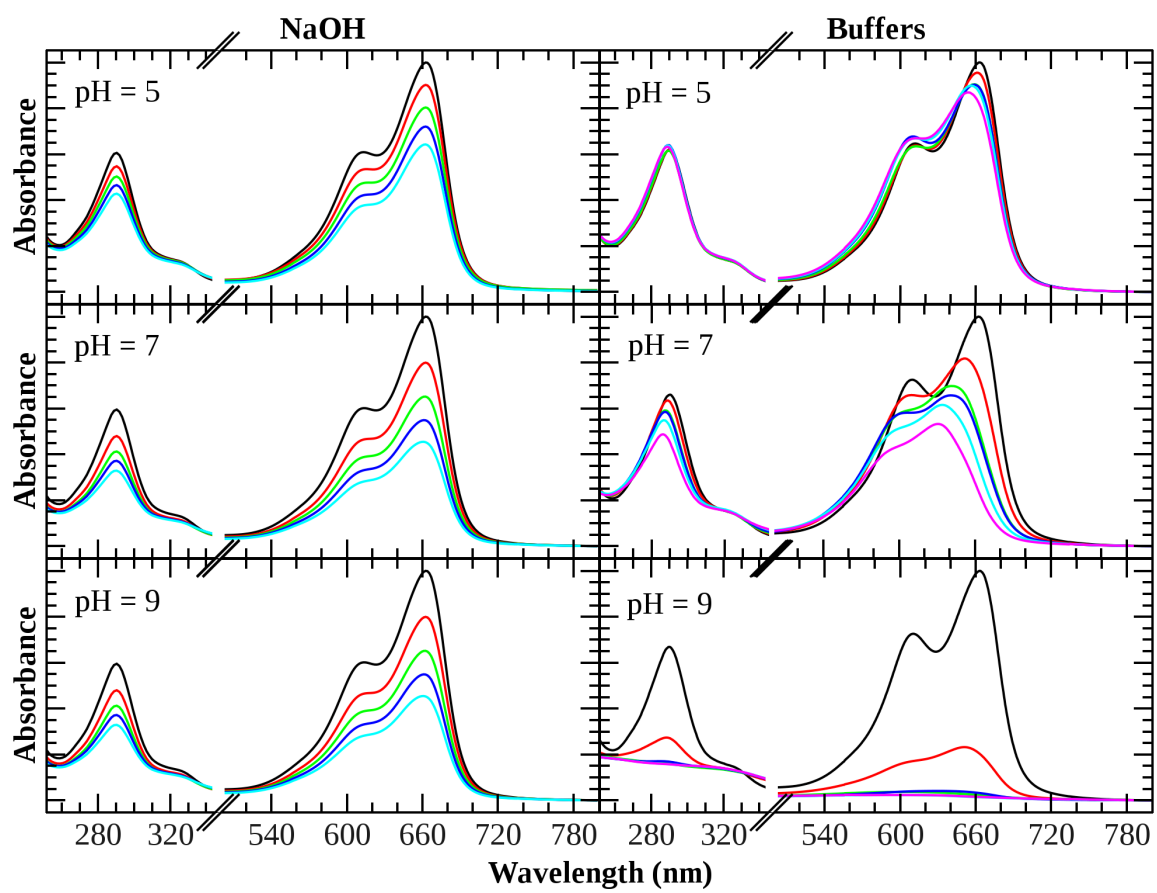


Figure 7.4: The effect of buffer solutions on the autodegradation of MB.

REFERENCES

- (1) Li, J.-G.; Ishigaki, T.; Sun, X. Anatase, Brookite, and Rutile Nanocrystals via Redox Reactions under Mild Hydrothermal Conditions: Phase-Selective Synthesis and Physicochemical Properties. *The Journal of Physical Chemistry C* **2007**, *111*, 4969–4976.
- (2) Rudnick, R. L. *The Crust: Treatise on Geochemistry*; Elsevier Science, 2006.
- (3) Government of Canada, C. C. for O. H. and S. Titanium Dioxide Classified as Possibly Carcinogenic to Humans. <http://www.ccohs.ca/headlines/text186.html> (accessed September 15, 2011).
- (4) Fujishima, A.; Honda, K. Electrochemical Photolysis of Water at a Semiconductor Electrode. *Nature* **1972**, *238*, 37–38.
- (5) This is commonly referred to as photocatalysis, a misnomer since a truly catalytic process would regenerate a photon.
- (6) Ganesh, V. A.; Raut, H. K.; Nair, A. S.; Ramakrishna, S. A review on self-cleaning coatings. *J. Mater. Chem.* **2011**, *21*, 16304–16322.
- (7) Abbaszadegan, M.; Hasan, M. N.; Gerba, C. P.; Roessler, P. F.; Wilson, B. R.; Kuennen, R.; Van Dellen, E. The disinfection efficacy of a point-of-use water treatment system against bacterial, viral and protozoan waterborne pathogens. *Water Research* **1997**, *31*, 574–582.
- (8) Sung, W. P.; Tsai, T. T.; Wu, M. J.; Wang, H. J.; Surampalli, R. Y. Removal of Indoor Airborne Bacteria by Nano-Ag/TiO₂ as Photocatalyst: Feasibility Study in Museum and Nursing Institutions. *Journal of Environmental Engineering* **2010**, *137*, 163.
- (9) Lee, J.; Mahendra, S.; Alvarez, P. J. J. Nanomaterials in the Construction Industry: A Review of Their Applications and Environmental Health and Safety Considerations. *ACS Nano* **2010**, *4*, 3580–3590.
- (10) Bethany Halford Building Small. *C&EN* **2011**, *89*, 12–17.
- (11) Tang, J.; Cowan, A. J.; Durrant, J. R.; Klug, D. R. Mechanism of O₂ Production from Water Splitting: Nature of Charge Carriers in Nitrogen Doped Nanocrystalline TiO₂ Films and Factors Limiting O₂ Production. *J. Phys. Chem. C* **2011**, *115*, 3143–3150.

- (12) Usubharatana, P.; McMartin, D.; Veawab, A.; Tontiwachwuthikul, P. Photocatalytic Process for CO₂ Emission Reduction from Industrial Flue Gas Streams. *Ind. Eng. Chem. Res.* **2006**, *45*, 2558–2568.
- (13) Shiraishi, Y.; Hirai, T. Selective organic transformations on titanium oxide-based photocatalysts. *Journal of Photochemistry and Photobiology C: Photochemistry Reviews* **2008**, *9*, 157–170.
- (14) Palmisano, G.; Augugliaro, V.; Pagliaro, M.; Palmisano, L. Photocatalysis: a promising route for 21st century organic chemistry. *Chem. Commun.* **2007**, 3425–3437.
- (15) Fujishima, A.; Zhang, X.; Tryk, D. A. TiO₂ photocatalysis and related surface phenomena. *Surface Science Reports* **2008**, *63*, 515–582.
- (16) Kikuchi, Y.; Sunada, K.; Iyoda, T.; Hashimoto, K.; Fujishima, A. Photocatalytic bactericidal effect of TiO₂ thin films: dynamic view of the active oxygen species responsible for the effect. *Journal of Photochemistry and Photobiology A: Chemistry* **1997**, *106*, 51–56.
- (17) Tatsuma, T.; Tachibana, S.; Miwa, T.; Tryk, D. A.; Fujishima, A. Remote Bleaching of Methylene Blue by UV-Irradiated TiO₂ in the Gas Phase. *J. Phys. Chem. B* **1999**, *103*, 8033–8035.
- (18) ASTM G173 - 03(2008) Standard Tables for Reference Solar Spectral Irradiances. **2008**.
- (19) Asahi, R.; Morikawa, T.; Ohwaki, T.; Aoki, K.; Taga, Y. Visible-Light Photocatalysis in Nitrogen-Doped Titanium Oxides. *Science* **2001**, *293*, 269–271.
- (20) Batzill, M.; Morales, E. H.; Diebold, U. Influence of Nitrogen Doping on the Defect Formation and Surface Properties of TiO₂ Rutile and Anatase. *Phys. Rev. Lett.* **2006**, *96*, 026103.
- (21) Anpo, M.; Kamat, P. V. *Environmentally Benign Photocatalysts: Applications of Titanium Oxide-based Materials*; Springer, 2010.
- (22) Braun, A.; Akurati, K. K.; Fortunato, G.; Reifler, F. A.; Ritter, A.; Harvey, A. S.; Vital, A.; Graule, T. Nitrogen Doping of TiO₂ Photocatalyst Forms a Second e_g State in the Oxygen 1s NEXAFS Pre-edge. *J. Phys. Chem. C* **2009**, *114*, 516–519.
- (23) Thompson, T.; Yates, J. TiO₂-based Photocatalysis: Surface Defects, Oxygen and Charge Transfer. *Topics in Catalysis* **2005**, *35*, 197–210.
- (24) Yates, H. M.; Nolan, M. G.; Sheel, D. W.; Pemble, M. E. The role of nitrogen doping on the development of visible light-induced photocatalytic activity in thin TiO₂ films grown on glass by chemical vapour deposition. *Journal of Photochemistry and Photobiology A: Chemistry* **2006**, *179*, 213–223.

- (25) Oropeza, F. E.; Harmer, J.; Egdeell, R. G.; Palgrave, R. G. A critical evaluation of the mode of incorporation of nitrogen in doped anatase photocatalysts. *Physical Chemistry Chemical Physics* **2010**, *12*, 960.
- (26) Ai, Z.; Zhu, L.; Lee, S.; Zhang, L. NO treated TiO₂ as an efficient visible light photocatalyst for NO removal. *Journal of Hazardous Materials* **2011**, *192*, 361–367.
- (27) Vargas, S.; Arroyo, R.; Haro, E.; Rodríguez, R. Effects of Cationic Dopants on the Phase Transition Temperature of Titania Prepared by the Sol-Gel Method. *Journal of Materials Research* **1999**, *14*, 3932–3937.
- (28) Liu, S.; Yu, J.; Jaroniec, M. Anatase TiO₂ with Dominant High-Energy {001} Facets: Synthesis, Properties, and Applications. *Chem. Mater.* **2011**, *23*, 4085–4093.
- (29) Henderson, M. A. A surface science perspective on photocatalysis. *Surface Science Reports* **2011**, *66*, 185–297.
- (30) Ganesh, V. A.; Raut, H. K.; Nair, A. S.; Ramakrishna, S. A review on self-cleaning coatings. *J. Mater. Chem.* **2011**, *21*, 16304–16322.
- (31) Zaleska, A. Doped-TiO₂: A Review. *Recent Patents on Engineering* **2008**, *2*, 157–164.
- (32) Detlef, B. Photocatalytic water treatment: solar energy applications. *Solar Energy* **2004**, *77*, 445–459.
- (33) Hoffmann, M. R.; Martin, S. T.; Choi, W.; Bahnemann, D. W. Environmental Applications of Semiconductor Photocatalysis. *Chem. Rev.* **1995**, *95*, 69–96.
- (34) Wyckoff, R. Crystal Structures 1. In *Crystal Structures 1*; Interscience Publishers: New York, New York, 1963; pp. 239–444.
- (35) Parker, R. Zur Kristallstruktur von Anastas und Rutil. (II. Teil. Die Anastasstruktur). *Zeitschrift für Kristallographie* **1924**, *59*, 1–54.
- (36) Knacke, O.; Hesselmann, K. *Thermochemical properties of inorganic substances*; Springer-Verlag, 1991.
- (37) H. E. Swanson, H. F. McMurdie, M. C. Morris, and E. H. Evans Section 7. In *Standard X-ray Powder Diffraction Patterns*; National Bureau of Standards, 1969; pp. 88–89.
- (38) Sun, J.; Gao, L.; Zhang, Q. Synthesizing and Comparing the Photocatalytic Properties of High Surface Area Rutile and Anatase Titania Nanoparticles. *Journal of the American Ceramic Society* **2003**, *86*, 1677–1682.
- (39) Sun, J.; Gao, L.; Zhang, Q. Synthesizing and Comparing the Photocatalytic Properties of High Surface Area Rutile and Anatase Titania Nanoparticles. *Journal of the American*

- Ceramic Society* **2003**, 86, 1677–1682.
- (40) Hanaor, D. A. H.; Sorrell, C. C. Review of the anatase to rutile phase transformation. *Journal of Materials Science* **2010**, 46, 855–874.
- (41) Morley, I. W. *Black sands: a history of the mineral sand mining industry in eastern Australia* / I.W. Morley; University of Queensland Press: St. Lucia, Qld. :, 1981.
- (42) Moore, D. Key issues in the medium term outlook for titanium and zircon minerals. In; Canberra, 1997.
- (43) Titanium - Mineral Fact Sheets - Australian Mines Atlas. http://www.australianminesatlas.gov.au/education/fact_sheets/titanium.html (accessed May 15, 2012).
- (44) Yin, H.; Wada, Y.; Kitamura, T.; Kambe, S.; Murasawa, S.; Mori, H.; Sakata, T.; Yanagida, S. Hydrothermal synthesis of nanosized anatase and rutile TiO₂ using amorphous phase TiO₂. *J. Mater. Chem.* **2001**, 11, 1694–1703.
- (45) Ulrike, D. The surface science of titanium dioxide. *Surface Science Reports* **2003**, 48, 53–229.
- (46) Wu, J. C. S.; Cheng, Y.-T. In situ FTIR study of photocatalytic NO reaction on photocatalysts under UV irradiation. *Journal of Catalysis* **2006**, 237, 393–404.
- (47) Zhao, W.; Chen, C.; Li, X.; Zhao, J.; Hidaka, H.; Serpone, N. Photodegradation of Sulforhodamine-B Dye in Platinized Titania Dispersions under Visible Light Irradiation: Influence of Platinum as a Functional Co-catalyst. *J. Phys. Chem. B* **2002**, 106, 5022–5028.
- (48) Kachina, A.; Puzenat, E.; Ould-Chikh, S.; Geantet, C.; Delichere, P.; Afanasiev, P. A New Approach to the Preparation of Nitrogen-Doped Titania Visible Light Photocatalyst. *Chem. Mater.* **2012**.
- (49) Jagadale, T. C.; Takale, S. P.; Sonawane, R. S.; Joshi, H. M.; Patil, S. I.; Kale, B. B.; Ogale, S. B. N-Doped TiO₂ Nanoparticle Based Visible Light Photocatalyst by Modified Peroxide Sol–Gel Method. *J. Phys. Chem. C* **2008**, 112, 14595–14602.
- (50) Gole, J. L.; Prokes, S. M.; Glembocki, O. J. Efficient Room-Temperature Conversion of Anatase to Rutile TiO₂ Induced by High-Spin Ion Doping. *The Journal of Physical Chemistry C* **2008**, 112, 1782–1788.
- (51) Na-Phattalung, S.; Smith, M. F.; Kim, K.; Du, M.-H.; Wei, S.-H.; Zhang, S. B.; Limpijumnong, S. First-principles study of native defects in anatase TiO₂. *Phys. Rev. B* **2006**, 73, 125205.

- (52) Mineralogical Society *The Mineralogical Magazine and Journal of the Mineralogical Society*; Mineralogical Society., 1897.
- (53) Di Valentin, C.; Pacchioni, G.; Selloni, A. Origin of the different photoactivity of N-doped anatase and rutile TiO₂. *Phys. Rev. B* **2004**, *70*, 085116.
- (54) Di Valentin, C.; Pacchioni, G.; Selloni, A.; Livraghi, S.; Giamello, E. Characterization of Paramagnetic Species in N-Doped TiO₂ Powders by EPR Spectroscopy and DFT Calculations. *J. Phys. Chem. B* **2005**, *109*, 11414–11419.
- (55) Bai, J.; Zhou, B.; Li, L.; Liu, Y.; Zheng, Q.; Shao, J.; Zhu, X.; Cai, W.; Liao, J.; Zou, L. The formation mechanism of titania nanotube arrays in hydrofluoric acid electrolyte. *Journal of Materials Science* **2008**, *43*, 1880–1884.
- (56) Li, D.; Haneda, H.; Labhsetwar, N. K.; Hishita, S.; Ohashi, N. Visible-light-driven photocatalysis on fluorine-doped TiO₂ powders by the creation of surface oxygen vacancies. *Chemical Physics Letters* **2005**, *401*, 579–584.
- (57) Czoska, A. M.; Livraghi, S.; Chiesa, M.; Giamello, E.; Agnoli, S.; Granozzi, G.; Finazzi, E.; Valentin, C. D.; Pacchioni, G. The Nature of Defects in Fluorine-Doped TiO₂. *The Journal of Physical Chemistry C* **2008**, *112*, 8951–8956.
- (58) *Comprehensive Handbook of Chemical Bond Energies - CRC Press Book*.
- (59) Li, S.; Hennigan, J. M.; Dixon, D. A.; Peterson, K. A. Accurate Thermochemistry for Transition Metal Oxide Clusters. *J. Phys. Chem. A* **2009**, *113*, 7861–7877.
- (60) Tang, J.; Quan, H.; Ye, J. Photocatalytic Properties and Photoinduced Hydrophilicity of Surface-Fluorinated TiO₂. *Chem. Mater.* **2007**, *19*, 116–122.
- (61) Park, H.; Choi, W. Effects of TiO₂ Surface Fluorination on Photocatalytic Reactions and Photoelectrochemical Behaviors. *J. Phys. Chem. B* **2004**, *108*, 4086–4093.
- (62) Zheng, Y.; Lv, K.; Wang, Z.; Deng, K.; Li, M. Microwave-assisted rapid synthesis of anatase TiO₂ nanocrystals with exposed {001} facets. *Journal of Molecular Catalysis A: Chemical* **2012**, *356*, 137–143.
- (63) Minero, C.; Mariella, G.; Maurino, V.; Pelizzetti, E. Photocatalytic Transformation of Organic Compounds in the Presence of Inorganic Anions. 1. Hydroxyl-Mediated and Direct Electron-Transfer Reactions of Phenol on a Titanium Dioxide–Fluoride System. *Langmuir* **2000**, *16*, 2632–2641.
- (64) Vohra, M. S.; Kim, S.; Choi, W. Effects of surface fluorination of TiO₂ on the photocatalytic degradation of tetramethylammonium. *Journal of Photochemistry and Photobiology A: Chemistry* **2003**, *160*, 55–60.

- (65) Wang, C. M.; Mallouk, T. E. Wide-range tuning of the titanium dioxide flat-band potential by adsorption of fluoride and hydrofluoric acid. *J. Phys. Chem.* **1990**, *94*, 4276–4280.
- (66) Huang, F.; Chen, L.; Wang, H.; Yan, Z. Analysis of the degradation mechanism of methylene blue by atmospheric pressure dielectric barrier discharge plasma. *Chemical Engineering Journal* **2010**, *162*, 250–256.
- (67) Yogi, C.; Kojima, K.; Wada, N.; Tokumoto, H.; Takai, T.; Mizoguchi, T.; Tamiaki, H. Photocatalytic degradation of methylene blue by TiO₂ film and Au particles-TiO₂ composite film. *Thin Solid Films* **2008**, *516*, 5881–5884.
- (68) Houas, A.; Lachheb, H.; Ksibi, M.; Elaloui, E.; Guillard, C.; Herrmann, J.-M. Photocatalytic degradation pathway of methylene blue in water. *Applied Catalysis B: Environmental* **2001**, *31*, 145–157.
- (69) Yu, Z.; Chuang, S. S. C. Probing Methylene Blue Photocatalytic Degradation by Adsorbed Ethanol with In Situ IR. *J. Phys. Chem. C* **2007**, *111*, 13813–13820.
- (70) Shirley, D. A. High-Resolution X-Ray Photoemission Spectrum of the Valence Bands of Gold. *Phys. Rev. B* **1972**, *5*, 4709.
- (71) Moulder, J. F.; Stickle, W. F.; Sobol, P. E.; Bomben, K. D. *Handbook of X Ray Photoelectron Spectroscopy: A Reference Book of Standard Spectra for Identification and Interpretation of XPS Data*; Physical Electronics, 1995.
- (72) Private communication with Dr. Mark Weaver, Department of Metallurgical and Materials Engineering, The University of Alabama, Tuscaloosa, AL.
- (73) Scherrer, P. Bestimmung der Größe und der inneren Struktur von Kolloidteilchen mittels Röntgenstrahlen. *Göttinger Nachrichten Gesell.* **1918**, *2*, 98–100.
- (74) Penn, R. L.; Banfield, J. F. Morphology development and crystal growth in nanocrystalline aggregates under hydrothermal conditions: insights from titania. *Geochimica et Cosmochimica Acta* **1999**, *63*, 1549–1557.
- (75) Langford, J. I.; Wilson, A. J. C. Scherrer after sixty years: A survey and some new results in the determination of crystallite size. *Journal of Applied Crystallography* **1978**, *11*, 102–113.
- (76) The instrument was designed and built by Dr. Alan Lane in the Chemical Engineering Department at the University of Alabama. We appreciate Dr. Lane's assistance in this project.
- (77) ASTM D4567 - 03(2008) Standard Test Method for Single-Point Determination of Specific Surface Area of Catalysts and Catalyst Carriers Using Nitrogen Adsorption by Continuous Flow Method. **2008**.

- (78) Torrents, A.; Stone, A. T. Catalysis of picolinate ester hydrolysis at the oxide/water interface: inhibition by coadsorbed species. *Environ. Sci. Technol.* **1993**, *27*, 1060–1067.
- (79) Yan, X.; Ohno, T.; Nishijima, K.; Abe, R.; Ohtani, B. Is methylene blue an appropriate substrate for a photocatalytic activity test? A study with visible-light responsive titania. *Chemical Physics Letters* **2006**, *429*, 606–610.
- (80) Levenberg, K. A Method for the Solution of Certain Non-Linear Problems in Least Squares. *Quart. Appl. Math.* **1944**, *2*, 164–168.
- (81) Marquardt, D. W. An Algorithm for Least-Squares Estimation of Nonlinear Parameters. *Journal of the Society for Industrial and Applied Mathematics* **1963**, *11*, 431–441.
- (82) Zhang, T.; Oyama, T.; Aoshima, A.; Hidaka, H.; Zhao, J.; Serpone, N. Photooxidative N-demethylation of methylene blue in aqueous TiO₂ dispersions under UV irradiation. *Journal of Photochemistry and Photobiology A: Chemistry* **2001**, *140*, 163–172.
- (83) Zare, R. N. *Laser experiments for beginners*; University Science Books, 1995.
- (84) Schulthess, C. P.; Sparks, D. L. Backtitration Technique for Proton Isotherm Modeling of Oxide Surfaces. *Soil Sci Soc Am J* **1986**, *50*, 1406–1411.
- (85) Kosmulski, M. *Surface Charging and Points of Zero Charge*; Surfactant Science Series; CRC Press, 2009.
- (86) Bhattacharyya, A.; Kawi, S.; Ray, M. B. Photocatalytic degradation of orange II by TiO₂ catalysts supported on adsorbents. *Catalysis Today* **2004**, *98*, 431–439.
- (87) NIST Mass Spec Data Center, S.E. Stein, director Infrared Spectra. In *NIST Chemistry WebBook, NIST Standard Reference Database Number 69*; National Institute of Standards and Technology: Gaithersburg MD, 20899.
- (88) Jensen, H.; Soloviev, A.; Li, Z.; Søgaaard, E. G. XPS and FTIR investigation of the surface properties of different prepared titania nano-powders. *Applied Surface Science* **2005**, *246*, 239–249.
- (89) Liu, S.; Yu, J.; Wang, W. Effects of annealing on the microstructures and photoactivity of fluorinated N-doped TiO₂. *Phys. Chem. Chem. Phys.* **2010**, *12*, 12308.
- (90) Park, H.; Choi, W. Effects of TiO₂ Surface Fluorination on Photocatalytic Reactions and Photoelectrochemical Behaviors. *The Journal of Physical Chemistry B* **2004**, *108*, 4086–4093.
- (91) Barth, G.; Linder, R.; Bryson, C. Advances in charge neutralization for XPS measurements of nonconducting materials. *Surface and Interface Analysis* **2004**, *11*, 307–311.

- (92) Kohiki, S.; Oki, K. Problems of adventitious carbon as an energy reference. *Journal of Electron Spectroscopy and Related Phenomena* **1984**, *33*, 375–380.
- (93) Swift, P. Adventitious carbon—the panacea for energy referencing? *Surface and Interface Analysis* **2004**, *4*, 47–51.
- (94) Charles D. Wagner; Alexander V. Naumkin; Anna Kraut-Vass; Juanita W. Allison; Cedric J. Powell; John R. Rumble, Jr NIST X-ray Photoelectron Spectroscopy (XPS) Database, Version 3.5. http://srdata.nist.gov/xps/query_chem_name_detail.aspx?ID_NO=2178&CName=ammonium%20chloride (accessed April 20, 2012).
- (95) Baltrusaitis, J.; Jayaweera, P. M.; Grassian, V. H. XPS study of nitrogen dioxide adsorption on metal oxide particle surfaces under different environmental conditions. *Phys. Chem. Chem. Phys.* **2009**, *11*, 8295–8305.
- (96) Hojamberdiev, M.; Zhu, G.; Sujaridworakun, P.; Jinawath, S.; Liu, P.; Zhou, J.-P. Visible-light-driven N–F-codoped TiO₂ powders derived from different ammonium oxofluorotitanate precursors. *Powder Technology* **2012**, *218*, 140–148.
- (97) Diebold, U.; Madey, T. E. Adsorption and electron stimulated desorption of NH₃/TiO₂ (110). In *38th National Symposium of the American Vacuum Society; AVS, 1992; Vol. 10*, pp. 2327–2335.
- (98) Chambers, S. A.; Cheung, S. H.; Shutthanandan, V.; Thevuthasan, S.; Bowman, M. K.; Joly, A. G. Properties of structurally excellent N-doped TiO₂ rutile. *Chemical Physics* **2007**, *339*, 27–35.
- (99) Wu, M. Efficient one-pot synthesis of Ag nanoparticles loaded on N-doped multiphase TiO₂ hollow nanorod arrays with enhanced photocatalytic activity. *Applied Surface Science* **2010**, *256*, 7125.
- (100) Yuan, J.; Chen, M.; Shi, J.; Shangguan, W. Preparations and photocatalytic hydrogen evolution of N-doped TiO₂ from urea and titanium tetrachloride. *International Journal of Hydrogen Energy* **2006**, *31*, 1326–1331.
- (101) Esaka, F.; Furuya, K.; Shimada, H.; Imamura, M.; Matsubayashi, N.; Sato, H.; Nishijima, A.; Kawana, A.; Ichimura, H.; Kikuchi, T. Comparison of surface oxidation of titanium nitride and chromium nitride films studied by x-ray absorption and photoelectron spectroscopy. *Journal of Vacuum Science & Technology A: Vacuum, Surfaces, and Films* **1997**, *15*, 2521–2528.
- (102) Dong, F.; Zhao, W.; Wu, Z.; Guo, S. Band structure and visible light photocatalytic activity of multi-type nitrogen doped TiO₂ nanoparticles prepared by thermal decomposition. *Journal of hazardous materials* **2009**, *162*, 763–770.

- (103) Pulsipher, D. J. V.; Martin, I. T.; Fisher, E. R. Controlled Nitrogen Doping and Film Colorimetrics in Porous TiO₂ Materials Using Plasma Processing. *ACS Applied Materials & Interfaces* **2010**, *2*, 1743–1753.
- (104) Giannakopoulou, T.; Todorova, N.; Osiceanu, P.; Lagoyannis, A.; Vaimakis, T.; Trapalis, C. Description of TiO₂ thin films treated in NH₃ atmosphere by optical dispersion models. *Thin Solid Films* **2009**, *517*, 6694–6699.
- (105) Serpone, N.; Emeline, A. V.; Kuznetsov, V. N.; Ryabchuk, V. K. Second Generation Visible-Light-Active Photocatalysts: Preparation, Optical Properties, and Consequences of Dopants on the Band Gap Energy of TiO₂. *Environmentally Benign Photocatalysts: Applications of Titanium Oxide-based Materials* **2010**, 35.
- (106) Thompson, T. L.; Yates, J. T. TiO₂-based Photocatalysis: Surface Defects, Oxygen and Charge Transfer. *Topics in Catalysis* **2005**, *35*, 197–210.
- (107) Berger, T.; Sterrer, M.; Diwald, O.; Knözinger, E.; Panayotov, D.; Thompson, T. L.; Yates, J. T. Light-Induced Charge Separation in Anatase TiO₂ Particles. *The Journal of Physical Chemistry B* **2005**, *109*, 6061–6068.
- (108) Vasapollo, G.; Nobile, C. F.; Sacco, A.; Gowenlock, B. G.; Sabbatini, L.; Malitesta, C.; Zambonin, P. G. Nitrosoarene complexes of rhodium (III), iridium (III), copper (I) and mercury (II). Use of XPS in determining the mode of bonding to transition metals. *Journal of organometallic chemistry* **1989**, *378*, 239–244.
- (109) Littlejohn, D.; Chang, S. G. An XPS study of nitrogen-sulfur compounds. *Journal of Electron Spectroscopy and Related Phenomena* **1995**, *71*, 47–50.
- (110) Uchida, K.; Soma, M.; Onishi, T.; Tamaru, K. XPS studies of nitrosyl metal (Fe, Co, and Mn) phthalocyanines. *Inorganica Chimica Acta* **1978**, *26*, L3–L4.
- (111) Batich, C. D.; Donald, D. S. X-ray photoelectron spectroscopy of nitroso compounds: relative ionicity of the closed and open forms. *Journal of the American Chemical Society* **1984**, *106*, 2758–2761.
- (112) Zhou, X.; Peng, F.; Wang, H.; Yu, H.; Yang, J. Preparation of nitrogen doped TiO₂ photocatalyst by oxidation of titanium nitride with H₂O₂. *Materials Research Bulletin* **2011**.
- (113) Chen, X.; Burda, C. The electronic origin of the visible-light absorption properties of C-, N- and S-doped TiO₂ nanomaterials. *Journal of the American Chemical Society* **2008**, *130*, 5018–5019.
- (114) Kubacka, A.; Colón, G.; Fernández-García, M. N- and/or W-(co) doped TiO₂-anatase catalysts: Effect of the calcination treatment on photoactivity. *Applied Catalysis B: Environmental* **2010**, *95*, 238–244.

- (115) Huang, D.; Miyamoto, Y.; Ding, J.; Gu, J.; Zhu, S.; Liu, Q.; Fan, T.; Guo, Q.; Zhang, D. A new method to prepare high-surface-area N-TiO₂/activated carbon. *Materials Letters* **2011**, *65*, 326–328.
- (116) Cong, Y.; Xiao, L.; Zhang, J.; Chen, F.; Anpo, M. Preparation and characterization of nitrogen-doped TiO₂ photocatalyst in different acid environments. *Research on chemical intermediates* **2006**, *32*, 717–724.
- (117) Palgrave, R. G.; Payne, D. J.; Egdell, R. G. Nitrogen diffusion in doped TiO₂ (110) single crystals: a combined XPS and SIMS study. *Journal of Materials Chemistry* **2009**, *19*, 8418.
- (118) Nosaka, Y.; Matsushita, M.; Nishino, J.; Nosaka, A. Y. Nitrogen-doped titanium dioxide photocatalysts for visible response prepared by using organic compounds. *Science and Technology of Advanced Materials* **2005**, *6*, 143–148.
- (119) Yu, Y. P.; Xing, X. J.; Xu, L. M.; Wu, S. X.; Li, S. W. N-derived signals in the x-ray photoelectron spectra of N-doped anatase TiO₂. *Journal of Applied Physics* **2009**, *105*, 123535.
- (120) Li, D.; Ohashi, N.; Hishita, S.; Kolodiazny, T.; Haneda, H. Origin of visible-light-driven photocatalysis: A comparative study on N/F-doped and N–F-codoped TiO₂ powders by means of experimental characterizations and theoretical calculations. *Journal of Solid State Chemistry* **2005**, *178*, 3293–3302.
- (121) Kim, Y. K.; Park, S.; Kim, K.; Kim, B. S. Photoemission Study of N-Doped TiO₂ (110) with NH₃. *The Journal of Physical Chemistry C* **2011**.
- (122) Chai, J. W.; Yang, M.; Chen, Q.; Pan, J. S.; Zhang, Z.; Feng, Y. P.; Wang, S. J. Effects of nitrogen incorporation on the electronic structure of rutile-TiO₂. *Journal of Applied Physics* **2011**, *109*, 023707.
- (123) Chen, H.; Nambu, A.; Wen, W.; Graciani, J.; Zhong, Z.; Hanson, J. C.; Fujita, E.; Rodriguez, J. A. Reaction of NH₃ with Titania: N-Doping of the Oxide and TiN Formation. *Journal of Physical Chemistry C* **2007**, *111*, 1366–1372.
- (124) Sathish, M.; Viswanathan, B.; Viswanath, R. P.; Gopinath, C. S. Synthesis, Characterization, Electronic Structure, and Photocatalytic Activity of Nitrogen-Doped TiO₂ Nanocatalyst. *Chemistry of Materials* **2005**, *17*, 6349–6353.
- (125) Escard, J.; Mavel, G.; Guerchais, J. E.; Kergoat, R. X-ray photoelectron spectroscopy study of some metal(II) halide and pseudohalide complexes. *Inorg. Chem.* **1974**, *13*, 695–701.
- (126) Li, D.; Haneda, H.; Labhsetwar, N. K.; Hishita, S.; Ohashi, N. Visible-light-driven photocatalysis on fluorine-doped TiO₂ powders by the creation of surface oxygen

- vacancies. *Chemical Physics Letters* **2005**, *401*, 579–584.
- (127) Yu, J. C.; Yu, H.; Jiang, Z.; Zhang, Y. Effects of F- Doping on the Photocatalytic Activity and Microstructures of Nanocrystalline TiO₂ Powders. *Chem. Mater.* **2002**, *14*, 3808–3816.
- (128) Henderson, M. A. Evidence for bicarbonate formation on vacuum annealed TiO₂ (110) resulting from a precursor-mediated interaction between CO₂ and H₂O. *Surface science* **1998**, *400*, 203–219.
- (129) Nie, L. H.; Xu, H. T.; Yuan, S. D. A Simple Way to Prepare C-doped TiO₂ with Visible Light Photocatalytic Activity. *Advanced Materials Research* **2011**, *239-242*, 1175–1179.
- (130) Diebold, U. The surface science of titanium dioxide. *Surface Science Reports* **2003**, *48*, 53–229.
- (131) Balachandran, U.; Erer, N. G. Raman spectra of titanium dioxide. *Journal of Solid State Chemistry* **1982**, *42*, 276–282.
- (132) Zhang, W. F.; He, Y. L.; Zhang, M. S.; Yin, Z.; Chen, Q. Raman scattering study on anatase TiO₂ nanocrystals. *Journal of Physics D: Applied Physics* **2000**, *33*, 912–916.
- (133) Hegazy, A.; Prouzet, E. Room Temperature Synthesis and Thermal Evolution of Porous Nanocrystalline TiO₂ Anatase. *Chem. Mater.* **2011**, *24*, 245–254.
- (134) Yu, J.; Xiang, Q.; Ran, J.; Mann, S. One-step hydrothermal fabrication and photocatalytic activity of surface-fluorinated TiO₂ hollow microspheres and tabular anatase single microcrystals with high-energy facets. *CrystEngComm* **2010**, *12*, 872.
- (135) Private communication with Dr. Michael Hoffmann, Department of Engineering and Applied Science, California Institute of Technology, Pasadena, CA, USA.
- (136) Ostwald, W. Studien über die Bildung und Umwandlung fester Körper. *Z. Phys. Chem.* **1897**, *22*, 289.
- (137) Boistelle, R.; Astier, J. P. Crystallization mechanisms in solution. *Journal of Crystal Growth* **1988**, *90*, 14–30.
- (138) Farias, R. F. de A new experimental procedure to obtain titania powders as anatase phase by a sol-gel process. *Química Nova* **2002**, *25*, 1027–1028.
- (139) Barnard, A. S.; Zapol, P. Effects of particle morphology and surface hydrogenation on the phase stability of TiO₂. *Phys. Rev. B* **2004**, *70*, 235403.
- (140) Janusz, W.; Jabłoński, J.; Sprycha, R. The Electrical Interfacial Layer at the TiO₂ (Anatase) / Electrolyte Interface - Adsorption of Zn(II) and Cd(II) Ions. *Journal of Dispersion Science and Technology* **2000**, *21*, 739–759.

- (141) Kuznetsov, V. N.; Serpone, N. On the Origin of the Spectral Bands in the Visible Absorption Spectra of Visible-Light-Active TiO₂ Specimens Analysis and Assignments. *J. Phys. Chem. C* **2009**, *113*, 15110–15123.
- (142) Yamaki, T.; Umebayashi, T.; Sumita, T.; Yamamoto, S.; Maekawa, M.; Kawasuso, A.; Itoh, H. Fluorine-doping in titanium dioxide by ion implantation technique. *Nuclear Instruments and Methods in Physics Research Section B: Beam Interactions with Materials and Atoms* **2003**, *206*, 254–258.
- (143) Nakamura, I.; Negishi, N.; Kutsuna, S.; Ihara, T.; Sugihara, S.; Takeuchi, K. Role of oxygen vacancy in the plasma-treated TiO₂ photocatalyst with visible light activity for NO removal. *Journal of Molecular Catalysis A: Chemical* **2000**, *161*, 205–212.
- (144) Kim, J.; Choi, W.; Park, H. Effects of TiO₂ surface fluorination on photocatalytic degradation of methylene blue and humic acid. *Research on Chemical Intermediates* **2010**, *36*, 127–140.
- (145) Asakawa, D.; Hiraoka, K. Study on the redox reactions for organic dyes and S-nitrosylated peptide in electrospray droplet impact. *Journal of Mass Spectrometry* **2009**, *44*, 461–465.
- (146) Narband, N. Nanoparticles and photosensitisers; their interactions and antibacterial properties, page 95, University College London, **2009**.
- (147) López, T.; Moreno, J. A.; Gómez, R.; Bokhimi, X.; Wang, J. A.; Yee-Madeira, H.; Pecchi, G.; Reyes, P. Characterization of iron-doped titania sol–gel materials. *J. Mater. Chem.* **2002**, *12*, 714–718.